Passive Remote Sensing of Lake Ice and Snow using Wideband Autocorrelation Radiometer (WiBAR)

by

Hamid Nejati

A dissertation submitted in partial fulfillment
of the requirements for the degree of
Doctor of Philosophy
(Electrical Engineering)
in The University of Michigan
2014

Doctoral Committee:

Professor Kamal Sarabandi, Co-Chair
Professor Anthony W. England, Co-Chair
Assistant Research Scientist Roger D. De Roo
Professor Christopher S. Ruf

I dedicate my dissertation work to my family. A special feeling of gratitude to my loving parents and fiancee, whose encouragement and push for success drove me forward in my research.

ACKNOWLEDGEMENTS

It would not have been possible to write this doctoral thesis without the help and support of the kind people around me, to only some of whom it is possible to give particular mention here.

I would like to express my deepest gratitude to both of my research advisers, Professors Anthony W. England and Kamal Sarabandi, for their continuous insight guidance, caring, patience, and providing me with an excellent atmosphere for doing research. They have always been very helpful and generous in supporting me through my graduate study, and offering me several opportunities to interact with other researchers in the remote sensing community in related conferences and workshops. I also appreciate their commitment to train me in both aspects of experiments and theory in the remote sensing field. This thesis would not have been possible without their hard work and dedication. I would also like to thank Dr. Roger DeRoo in my committee who helped me in both theoretical and experimental sides of my PhD work. His continuous help and research ideas are highly appreciated. I also thank my other committee member, Professors Chris Ruf, who has provided important insights and ideas for improving the content of this thesis and also sharing his equipments and instruments with us for this work. I would also like to thank department of energy

for funding this project.

I am also grateful to my colleagues Sing Y. E. Wong, Lin van Nieuwstadt, Aravind Venkitasubramony, Benjamin Perkins, Timothy Doyle, Carl Lachner, Kishan Patel, and Michael Benson. I also appreciate the help of the Space Physics Research Laboratory (SPRL) staffs in Atmospheric, Oceanic and Space Sciences (AOSS) department David Boprie, Ronald Rizor, and Bradley Angelocc for helping us to make the final design and implemetation. In particular, I would like to thank Professor Guy Meadows of Michigan technological University (MTU) and the staffs of Great Lakes research center in MTU Mike Abbott, Colin Tyrrell, Jamey Anderson and coast guard staffs for their help, support, and accompanying us in the repair trips in the harsh environment in the South light house entry of Keweenaw Bay near Houghton, MI.

My deepest appreciation goes to my beloved family for their constant support and endless love. I would also like to thank all my friends, radlab members, and Iranian community for providing a relaxing environment, in which I could thrive. Their support made my doctorate study dream comes true. Finally, I wish to thank my fiancee, Niksa Valim, who has worked behind the scene as a true friend and an adviser during my graduate study.

TABLE OF CONTENTS

LIST OF FIGURES

Figure

ABSTRACT

Passive Remote Sensing of Lake Ice and Snow using Wideband Autocorrelation Radiometer (WiBAR)

by

Hamid Nejati

Co-Chairs: Anthony W. England and Kamal Sarabandi

Snow cover plays a vital role in providing the water supplies for domestic, industrial, and agricultural purposes. Snow cover also is important to the global climate. Therefore, understanding of the global snow cover dynamics is required for both the planet's climate study and water resource management. Conventionally, differential scatter darkening technique is used to detect the snow thickness. This technique is region specific and depends on the statistics of snow grain sizes. Ice formation process and ice thickness monitoring are important parameters in analyzing the overall pressure exerted to the off-shore structures such as wind farms. Lake ice thickness measurement is also required for the safety purposes for ice fishing or skating. The traditional method for measuring the lake ice thickness is by a cumbersome drilling process through the ice, which is labor intensive and potentially dangerous. For future in-situ or remote planetary applications, the detection and analysis of ice sheets on or

near the surface is one of the primary objectives of many planetary exploration missions. These applications demonstrate the requirement for an accurate remote sensing instrument, which can estimate the ice thickness without disturbing or breaking the ice.

In this work, a novel microwave remote sensing technique to accurately estimate the thickness of any layered low-absorbing media including snow pack and fresh water ice using wideband autocorrelation radiometer (WiBAR) is presented. This technique relies on finding the autocorrelation response of the upwelling brightness temperature. The autocorrelation response provides enough information to estimate the microwave travel time delay of the doubly reflected thermal emission between the top and bottom interfaces. With knowledge of dielectric properties of fresh water ice or snow and also microwave transit time delay, the thickness of the snow or ice layer can be obtained. Several post processing techniques are developed to capture the periodicity of the ripples in the power spectral density domain. These techniques are capable of detecting very weak ripples deeply buried under noise. A compressive sensing based algorithm is also developed for detecting the thickness of ice/snow layers. The compressive sensing algorithm allows for retrieving the desired parameters with less data and increases the response time of the system. The proposed approach is capable of predicting the layer thickness with using only 1/10 that of the Nyquist rate. We have successfully designed, implemented, and tested a handheld ground base ice/snow thickness sensor under several scenarios including snow on top of undulated and vegetation covered terrain, ice over the lake water, air gap above a water surface and below a dielectric sheet, snow cover under the forest canopy. The proposed technology

is robust in the presence of radio frequency interference (RFI).

This research opens up the possibility of the ice sheet measurements using a stand off handheld device or in a large scale using an airborne or spaceborne platform. It is demonstrated that a WiBAR operating over the frequency band of $1-3$GHz or $7-10$GHz can estimate the thickness of snow/ice layer to within 1.5cm.

CHAPTER I

Introduction

The physics behind the emission and brightness temperature of a gray/black body is studied in Section 1.1. The importance of snowpacks and fresh water ice are explained in Sections 1.2 and 1.3, respectively. The role of passive microwave remote sensing in environmental studies is discussed in Section 1.4. Finally, the structure of the thesis is elaborated in Section 1.5.

1.1 Brightness temperature and black body radiation

The brightness temperature is originated due to the oscillatory motions of atomic-scale charges, which are the result of the material's temperature. The temperature causes a vibration in the lattice structure of the material. The vibration forces the electrons to accelerate and decelerate, which leads to emission/radiation of electromagnetic waves. These waves can be detected accurately using sensitive radiometers. The nature of radiation/emission is similar to the radiation of numerous randomly distributed infinitesimal dipole antennas radiating electromagnetic waves independently. Hence, any material with temperature above $0[K]$ emits.

The thermodynamic equilibrium states that the emission is equal to the absorption. A blackbody is defined as a material that absorbs incident waves at all frequen-

cies without reflection. The thermal emission of a blackbody can be formulated as given by 1.1 also known as Planck's formula (60).

$$I(f,T) = \frac{2hf^3}{c^2(e^{\frac{hf}{kT}} - 1)} \; [\frac{W}{m^2 sr Hz}], \tag{1.1}$$

where c is the speed of light in free space ($c = 3 \times 10^8$ [m/s]), h is the Planck's constant and is equal to $6.62 \times 10^{-34}[J.s]$, k is the Boltzmann's constant and is equal to $1.380 \times 10^{-23}[\frac{J}{K}]$, f is the frequency of interest in hertz, and T is the temperature of blackbody in kelvin. Most materials emit less than the emission predicted by Planck's formula, (1.1). These materials are referred as graybody radiators. The ratio of the graybody radiation to the blackbody radiation is called emissivity. This ratio is less than or equal to 1. The emissivity of a blackbody radiator is equal to 1. In the microwave remote sensing frequency range of interest, the Planck's formula can be simplified as $I(f,T) = \frac{2kTf^2}{c^2}$ (43; 35). This simplification is known as Rayleigh-Jeans law (78; 80).

1.1.1 Analysis of brightness temperature

To study the brightness temperature, the dependence of the emission to the statistics of dipoles including their orientations, locations, and frequencies is analyzed in this subsection. As it is pointed out, the brightness temperature is similar to the collective radiation of numerous infinitesimal dipole radiators in the material under study. The theoretical analysis of the brightness temperature has been fully explored in the literature by utilizing the statistical Maxwell's equations and the Fluctuation-Dissipation Theorem (FDT) (65; 66). The statistical Maxwell's equation analyze the radiation of randomly oriented dipoles in the material. The FDT is a common tool in analyzing the response of non-equilibrium thermodynamic systems used in statistical physics. This tool is capable of predicting the response of the system to an applied perturbation as a function of fluctuations in a system at thermal equilibrium. Using

these two theorems, the statistical response of the dipole radiator's currents can be formulated as given by (1.2) (4) for an isotropic and homogeneous dielectric medium.

$$< j_{\theta_1}(r,f) j_{\theta_2}(r',f') >= 2fI(f,T)\epsilon_0\epsilon''(f)\delta(\theta_1-\theta_2)\delta(r-r')\delta(f-f'), \qquad (1.2)$$

where $< ... >$ is the statistical ensemble average of the infinitesimal dipole currents. $I(f,T)$ is defined as in (1.1) and $\epsilon_0 = 8.85 \times 10^{-12}[F/m]$ is the permittivity of free space. ϵ'' is the imaginary part of ϵ_r, where ϵ_r is the relative dielectric constant of the material. The permittivity of the material can be formulated as $\epsilon = \epsilon_0\epsilon_r = \epsilon_0(\epsilon' + j\epsilon'')$. The ϵ'' is a function of frequency. $\delta(x)$ is the Dirac-delta function, which is equal to zero everywhere except at $x = 0$ with an integral of one over the entire real line. r indicates the position of the dipole current and θ refers to the orientation of each infinitesimal dipole.

Equation (1.2) states that the currents of the virtual dipole radiators are fully independent from each other in all positions, frequencies, orientations, and angles. Therefore; there is absolutely no dependence between the orientation, location and frequency of the dipole radiators in thermal equilibrium. Statistically speaking, the correlation length of the emitted electromagnetic wave is zero.

The analysis of brightness temperature emission is equivalent to detecting the collective radiation of numerous independent, uncorrelated infinitesimal dipole radiators oriented uniformly and independently. The amplitude distribution of the collective radiation of this equivalent system is Gaussian, based on the central limit theorem. Central limit theorem in classical probability states that the probability distribution of the arithmetic mean (collective radiation of the dipoles) of a large number of well defined independent random variables (based on (1.2)) is Gaussian (58).

To this point, we showed that the brightness temperature of half-space isotropic and homogeneous dielectric has a Gaussian distribution and fully independent with

correlation length of zero in frequency, location, and orientation. Hence, specifically the thermal emission of water and terrain (soil) have Gaussian distribution.

The thickness detection of low absorbing media are of interest in several applications including the snowpacks and fresh water lake ice. Snowpack is the accumulation of snow found mainly in mountainous and higher latitude regions. The importance of monitoring the snowpack thickness is due to its vital significance in water resource management, flood and avalanche prediction as well as ecosystem and climate studies (56; 67; 82; 45; 26). Climate change causes the non-stationary annual statistics in the snowpacks' characteristics that should be monitored in a nearly daily time intervals (50; 68; 3; 1; 2; 74; 81).

1.2 Snowpack

Snowpacks play a vital role in providing the water supplies for domestic, agricultural, and industrial purposes. Snow melt provides the main water source for arid mountainous regions. Seasonal snowpacks are also natural resource for hydropower generation (42).It can negatively affect railroad and naval transportations and communications.

Snow packs also cause flooding and avalanche. One of the main reasons of avalanche formation is due to very fast melting rate of sow packs in sloped mountainous regions. The high temperature gradient generates depth hoar that accounts for avalanche formation. Another cause of avalanche is the movement of snow layers within the snow pack over a weak snow layer due to an external trigger.

The gradual temperature rise of our planet causes the melting of the glaciers, especially in the Greenland, the reduction of the snow packs in mountains, and rising of the sea water level. The column of water released after complete melting of the snowpack is known as Snow Water Equivalent (SWE) and can be calculated as $SWE = d(\rho_s/\rho_w)$, where ρ_s and ρ_w are the density of the snow and water, respec-

tively. d is the depth of the snowpack.

The thickness of snow layer over the terrain after each snow storm is used as an indicator to scale the severity of the snow storm in northeast snowfall impact scale. The scale includes five categories of snow storms. Snow on the ground increases the albedo and also provides an insulation layer over the terrain. This thermal insulation layer separates the very cold temperature on the surface of the snow from the terrain under the snow layer. Therefore, the underlying soil stays relatively warm and unfrozen. This phenomenon protects many types of vegetations from very low air temperature. Some small animals survive underneath snowpacks. Snow is also habitat for some snow worms and algae (5).

The rapid melting process due to the global warming changes the annual statistics of the snow packs including extent, timing, and snow water equivalent (SWE) of seasonal snow packs. This leads to non-stationary annual statistics that should be monitored in nearly daily intervals. Conventionally, the snow pack thickness has been monitored using radiometers by applying differential scatter darkening technique. A radiometer is a passive instrument that can detect the brightness temperature emanating from the targets in the form of power in a specific frequency band. Due to the refreezing process of the snow grains in days and nights, the effective grain size is changing, which leads to the volumetric scattering of the snow grains at very high frequencies. Passive remote sensing of the snow at two different frequencies with scatter darkening more pronounced at higher frequency can capture the volumetric scattering of the snow pack. Using empirical formulation, the SWE and snowpack thickness can be estimated. The complexity of the terrain beneath the snow complicates the tuning algorithm that can capture the nonlinearity in subpixel heterogeneities of the terrain. Accurate estimation of the SWE is also required for thickness estimation. The empirical formulae are region specific. Hence, a general technique, which can work globally is an open research problem and is highly desired.

1.3 Fresh water ice

In this section, the hydrology of fresh water ice as well as the impact of ice sheet on the offshore structures specifically offshore wind farms are explained.

1.3.1 Lake ice hydrology

Fresh water ice affects human life both positively and negatively. The influences of lake ice on human activities are in industrial production, building, transport of goods, and winter sports. It can also endanger human life.

Less than 3% of all waters on the earth is fresh water including ice caps, glaciers, ground waters, soil, lakes, rivers, and the atmosphere (5). Among fresh water lakes, the Great Lakes, also known as inland seas, have more than 21% of all fresh water on earth including lakes and rivers. The Lake Superior is the largest freshwater lake on the globe.

The formation process of the fresh water ice starts by cooling the air over the lake. The lake temperature changes locally on the surface of the lake, which is in direct contact with the cold air. Water density is a function of temperature and the maximum water density occurs at $4°C$. As the air temperature cools down, the surface water temperature goes down toward $4°C$. The density of this layer of water is larger than the rest of the lake water; therefore, it sinks to the bottom of the lake. This process continues till all of the lake water is at $4°C$. Further cooling in the air temperature reduces the surface water temperature to $0°C$. Then, the initial ice layer formation starts on the surface of the lake. The ice layer then thickened and the water level goes down. When the temperature rises, the ice cover break up begins and finally the ice is disappeared. The existence of warm water at the bottom of the lake provides an ecosystem for the fish to live.

The hydrology science is interested in characterizing the ice, annual variation of the ice, ice forecast including ice formation, jamming, and breakup. The impact of

the fresh water lake can be listed as follows. The ice cover over the lakes reduces the amount of water evaporation in winter, which reduces the risk of lowering the lake water level. The ice formation over the lake reduces the heavy lake-effect snowfalls. The lake-effect snowfalls happen due to the contact of the cold air with the warm unfrozen lake surface at early winter. The moving cold air evaporates the lake water, which leads to high concentration of water vapor moving toward the shore lines. It results in heavy snowfalls on the lands around the lake. Ice cover over the lake reduces the chance of the lake-effect snowfalls. Lake ice formation also limits the existence of waves at the shore, which erodes the shoreline (5).

The ice formation on the Great Lakes starts at the shoreline and extends toward the center of the lake. The melting/breaking of the ice also starts at the center of the lake toward the shoreline. At the end of the winter the small floes of ice known as pancake ice are formed around the shoreline.

The ice cover moves with the water level up and down in a daily cycle. This movement causes stress and strain on ice layer, which leads to crack formation on the ice. The isolated ice sheets move with the wind and this moving ice floes to the shore can cause damage to the offshore structures and the shoreline.

The major ice type on the lakes with small flow velocity are black ice and snow ice (white ice). The black ice is the ice formed from below without any trapped bubbles in the ice and is fully transparent. On the other hand, the snow fall over the ice layer can cause further thickening of the ice layer. The water-soaked snow freezes and becomes the white ice.

1.3.2 Ice impact on off-shore structures

Fossil fuels cause massive generation of CO_2, which leads to global warming (32). The possible solution is in using renewable energy sources. These substitutes are wind energy, solar energy, wave, bio fuels, and other sources. In the state of Michigan,

where this study has been developed, the possible choices are wind (more than 70%) and solar energy (more than 25%). The Union of Concerned Scientists (UCS) suggests a portfolio standard, in which the national policy to increase the United States use of renewable energy should be reached to 20% by the year 2020. The state of Michigan has the technical potential to generate at least 71% of its current electricity needs from wind renewable energy. The contribution of the wind to the total potential of other renewable energy sources in the state of Michigan is 89%. High wind regions in the state of Michigan are mainly concentrated in off-shore regions in the Great lakes as shown in Fig. 1.1. Building off-shore wind farms are challenging due to the severe ice formation in the winters over the Great Lakes. The exerted force from the ice is in the form of the vertical force during the ice formation and melting down, vertical force due to the daily water movement cycle, and the horizontal force due to the movement of ice floes to the structure. Currently, most of the offshore structures are designed conservatively, which causes increase in weight and project cost. An accurate technique to investigate the exerted force to the structure as a function of lake ice thickness enables us to estimate the exerted forces accurately and can avoid making the structure unnecessarily strong.

Ice characterization is required for inland waterway navigation. Non-destructive lake ice thickness sensing is beneficial for winter sports including ice fishing, ice skating, ice hockey, and snow mobile transportation over the lake ice.

It is also beneficial for planetary studies. For future in-situ or remote planetary applications, analysis of the ice sheets formed over the planetary surface is informative for space scientists.

These issues demonstrate the advantage of a remote accurate measurement setup, which can estimate the thickness without disturbing or breaking the ice.

Ice coverage over the Great lakes is shown in Fig. 1.2.

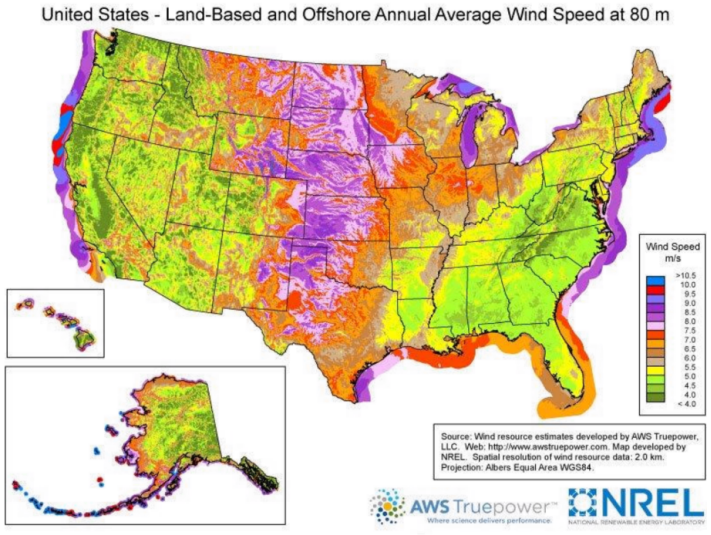

Figure 1.1: The wind map of the United States. The concentration of wind on Michigan state is mainly over the Great Lakes. Courtesy of NREL.

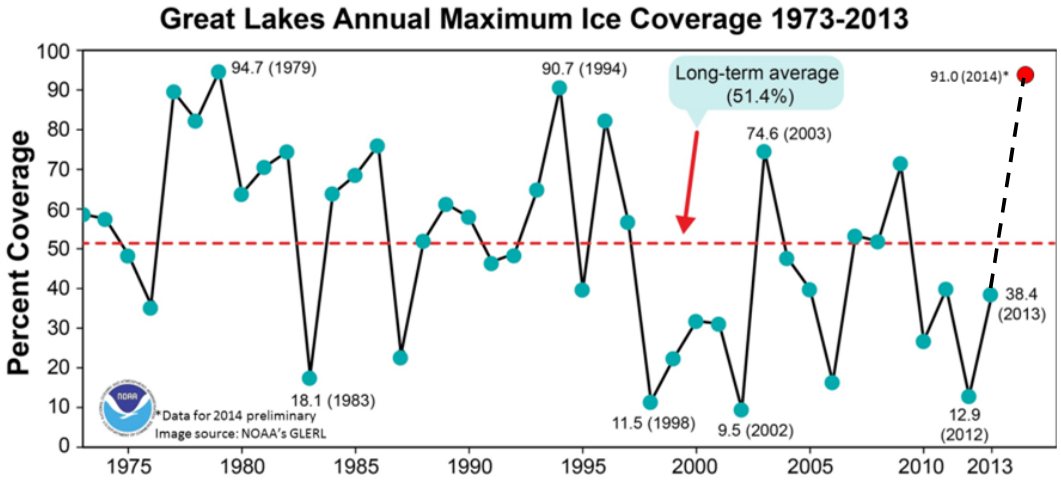

Figure 1.2: The ice coverage over the Great Lakes for the last 40 years. Courtesy of NOAA GLERL.

1.4 Passive and active microwave remote sensing of environment

Passive and active remote sensing are commonly used to monitor the environment. In active remote sensing the radar back scatter or the scattering matrix of the scene is of interest. However, in passive remote sensing the brightness temperature of the scene is monitored. Active remote sensing systems (radars) are based on monitoring the reflectivity of the scene of interest to the transmitted short pulses. The scene of interest is within the beam width of the antennae. The radars are divided into monostatic and bistatic systems. In monostatic radars, the transmitter and receiver are at the same location and the backscattering of the scene is of interest. However, in bistatic radars, the transmitter and the receiver are at different locations and the scattering matrix and radar cross sections of the scene are of interest. Radar altimeters are active microwave sensing system, which are capable of detecting the return of a short pulse transmitted normally to the scene of interest. This technique only capable of detecting flat surfaces in normal direction and is used to characterize the snowpacks.

Passive remote sensing systems (radiometers) are more common than the active counterparts in analyzing the statistics and characteristics of snow and ice layers. There is no transmitter inside the radiometer. In order to detect the brightness temperature of the scene under test, a highly sensitive receiver with complicated gain and temperature control procedures is required to precisely detect the brightness temperature. Differential scatter darkening has been the most common technique to measure the snow water equivalence (SWE) and also the thicknesses of snowpacks (20; 21; 14; 34; 25; 62; 86; 61; 16; 27; 33; 18; 71; 41). This phenomenon is due to the volumetric scattering of the snow grains at very high frequencies. This technique relies on observing the snowpacks at two different frequencies with scatter

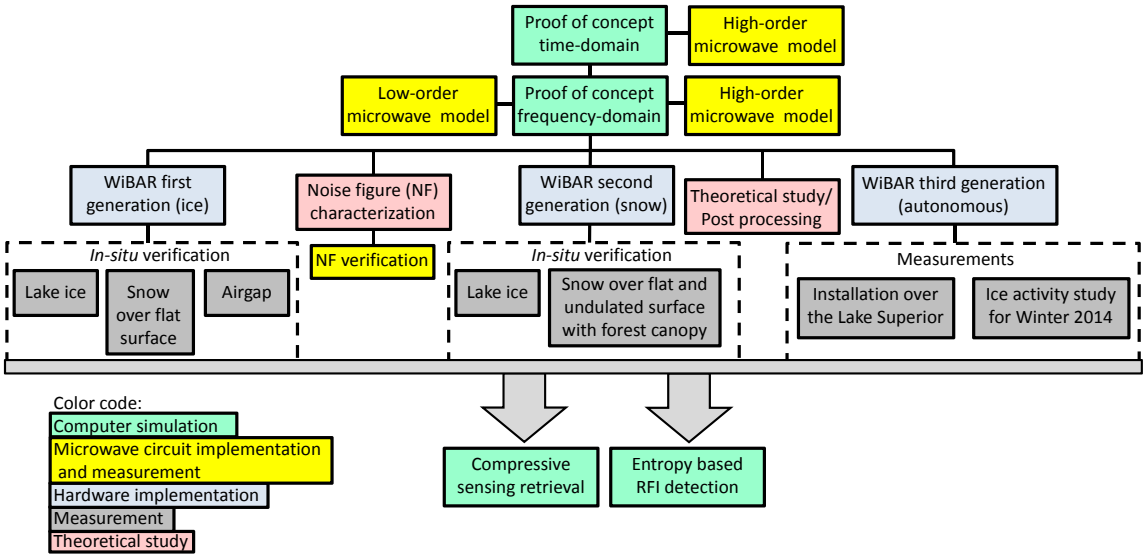

Figure 1.3: The flow of the work presented in this thesis. The color code shows the type of each work with its details.

darkening stronger at the higher frequency. Using this approach an empirical formulation is usually derived to estimate the snowpack thickness. However, the empirical formula is specific to the region (61; 16; 30; 29; 49; 15). The formula, which has been used in Finland for example does not work for Alaska and vice versa. Hence, a unique general method independent of location is highly desired. In the following chapters, we discuss our novel technique that is capable of detecting snow/ice layers globally. Differential scatter darkening technique is not capable of detecting sub-pixel variability. Subpixel variability is required for characterizing the snow thickness variation inside one footprint. The snow thickness variation is in the form of a constant slope and roughness.

1.5 Structure of thesis

The thesis follows the design, development, modeling, analysis, implementation of three generations of wideband autocorrelation radiometers (WiBARs) specified for ice and snow thickness measurements. A flowchart that illustrates the flow of materials

in this dissertation is shown in Fig. 1.3.

The rest of this thesis is organized as follows. The concept of WiBAR as well as the physics behind the operation of the WiBAR are discussed in Chapter II. The rest of Chapter II explores the software and microwave hardware models. Time and frequency domain circuits and systems are fully discussed and the measurement results are analyzed. The forward model is also addressed in this chapter.

The design procedure and implementation of the first generation of WiBAR is fully explained in Chapter III. The implemented three generations of WiBAR are illustrated and explained in this chapter. The statistical analysis of WiBAR as well as the impact of radio frequency interference (RFI) are also within this chapter. The implementation of a fully autonomous WiBAR, which has been installed over the Lake Superior in the Keweenaw Waterway near Houghton, Michigan during Winter 2014 is discussed and the ice activity is investigated in the rest of Chapter III.

In Chapter IV, the post processing procedure to detect the layer thickness is explained using the techniques commonly used in time-series analysis. These methods are capable of detecting very weak sinusoidal signals buried deeply in the noise. This technique is based on designing a matched filter to remove the system response on the measured data. The calibrated signal is then analyzed using Yule-Walker equation, which is one of the parametric methods in spectral analysis in time-series analysis. This technique is capable of reducing unwanted noise. For very weak signal detection, a procedure based on chaotic oscillators is introduced and used. An entropy based technique is also explained in this chapter, which is capable of detecting RFIs. At the end of this chapter, the utilization of compressive sensing is used for faster operation of this system.

The utilization of signal path in finding the noise figure of the wideband systems is explained in Chapter V. Finally, Chapter VI concludes the thesis and the future work is also explained in this chapter.

CHAPTER II

Wideband Autocorrelation Radiometer (WiBAR): Proof of Concept

2.1 Introduction

When ground/lake is covered by snow/ice, the received brightness temperature is a combination of the thermal emission of the underlying ground/lake water, the reflection of the downwelling sky brightness temperature, and the self emission of the snowpack/lake ice (when the layer is dry). The major contribution of the detected brightness temperature is due to the thermal emission of the underlying medium, illustrated in Fig. 2.1(a) and (b). This term is composed mainly of two parts. One is due to the direct transmission of the brightness temperature and the other is the result of the doubly reflected emitted wave inside the dry snow/ice layer due to reflection at the top and bottom interfaces. The doubly reflected wave has a transit time delay compared to the direct path wave and this delay is directly proportional to the thickness of the layer. The direct and the doubly reflected background brightness temperatures are shown by arrows in Fig. 2.1 (a) and (b). The doubly reflected path experiences more attenuation due to more absorption and scattering in the snowpack/ice layer as well as refraction at the top and bottom interfaces. The attenuation of the higher order bounced back path (quadruple reflected path) is high enough that

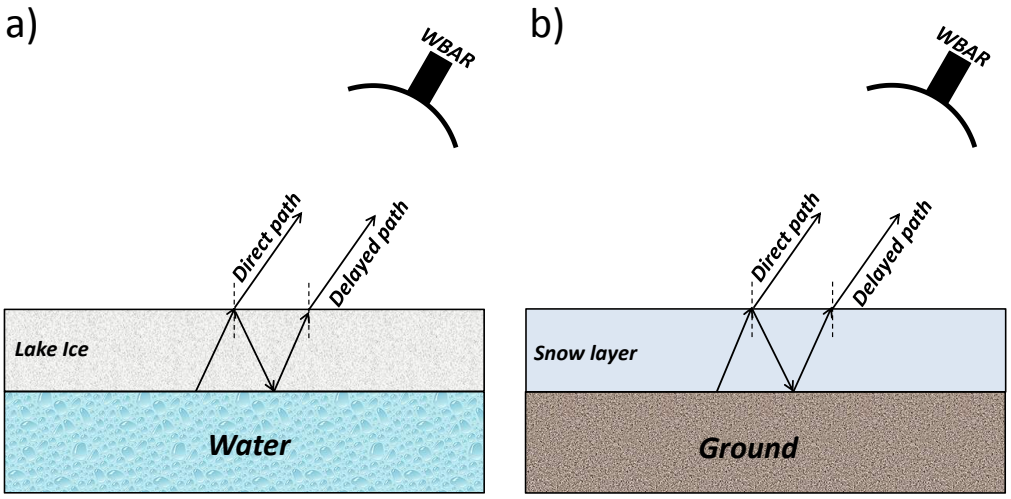

Figure 2.1: Test scenarios consist of (a) an ice layer on top of fresh water (Lake ice scenario) (b) snow layer on top of ground (snow scenario). The direct path of the brightness temperature of the underlying layer (T_A) as well as the doubly reflected brightness temperature path are shown by solid arrows.

we can ignore their presence in natural scenarios including lake ice and snowpack. In this chapter, the theoretical study of the physics of operation of our presented system is investigated. First, the concept of wideband radiometry is explained both in the time and frequency domain. Then, the derivation of microwave transit time delay is explained for several different layered materials including:

- Lossless, homogeneous, and isotropic medium with constant refractive index (fresh water ice)
- Lossy and isotropic medium with constant refractive index and extinction coefficient (fresh water ice with air bubbles trapped inside)
- layered media with refractive index as a function of vertical height (snowpack).

The dependence of the microwave transit time delay to snow water equivalent (SWE) is also discussed in this chapter. The analysis of the ripples in the power spectrum is also included in this chapter. The forward model for emissivity of single layer and bilayer structure is elaborated. At the second part of this chapter, a

low-order and high-order microwave circuit model for the physics of operation are introduced and implemented in hardware. The measurement results both for the time and frequency domain implementations are analyzed and compared. The dependence of the microwave transit time delay to the length of the layers and to the spectrum analyzer characteristics including resolution and video bandwidth is also investigated. At the end of this chapter, a theoretical procedure to find a closed form for the sensitivity of the radiometer is introduced. Using the closed form formulation, an optimum setup is presented to enhance both the measurement time and sensitivity.

2.2 Physics of operation

In this section, the physics behind the operation of our radiometer is elaborated. In Subsection 2.2.1, the operation and implementation of the system both in the time and frequency domains are explained. In Subsection 2.2.2, the dependency of the microwave transit time delay as a function of the thickness of the slab as well as the snow water equivalent (SWE) is discussed.

2.2.1 Time and frequency domain analysis

As discussed in Chapter I, the emission is the collective radiation of infinitesimal dipoles oriented randomly. If we keep track of the radiation of any of these dipoles, the wave travels a direct path and a doubly reflected path. The wave in both paths are originated from one specific dipole and hence is fully correlated. If the autocorrelation response of the brightness temperature is analyzed, the microwave transit time delay can be retrieved. This delay time shows as a peak in the autocorrelation response. The autocorrelation response of a zero mean random process with infinite bandwidth, also known as white noise, is a Dirac delta function. Limiting the bandwidth of the system causes the autocorrelation response drops smoothly from zero-lag peak with the $3dB$ bandwidth proportional to $1/B$, where B is the bandwidth of the radiometer.

The rate of drop of the autocorrelation response is a function of the bandwidth of the system. Therefore, a wide bandwidth is required for detecting the delay peak. In time domain implementation, the autocorrelation of the measured signal is of interest. In case of infinite bandwidth, if we assume that the time delay is equal to τ, we can find the autocorrelation of the $w(t) + w(t-\tau) + w(t-2\tau) + ...$, where $w(t)$ is a white Gaussian noise. The autocorrelation is equal to $\Sigma_{i=0}^{\infty}\delta(i\tau)$.

The frequency domain implementation is also possible. In this implementation, we utilize the Wiener-Khinchin theorem. This theorem states that the autocorrelation response of a stationary process is equal to the inverse Fourier transform of the power spectrum of that process. We have shown before that the emission has Gaussian distribution and is a stationary process. Therefore, this theorem can be applied to the brightness temperature. In the frequency domain implementation we expect to see periodic patterns, we call them ripples. The inverse Fourier transform of those generates peaks, which corresponds to the microwave transit time delay of the doubly reflected path compared to the direct path.

In one-dimensional layered media including snow and ice layers, the autocorrelation response of the received signal has several maxima due to the time difference in arrival of internal reflection at the top and bottom interfaces.

2.2.2 Microwave transit time delay

By calculating the exact time delay between the brightness temperature and its doubly reflected signal, we can find the ice/snow thickness from the microwave transit time delay. The time delay is composed of two terms. One is the summation of a double bouncing inside the ice slab, which should be subtracted from the time delay between direct path to the radiometer in the air. The overall time difference (τ) is given by (2.1).

$$\begin{aligned} \tau &= 2\tau_r - \tau_f \\ \tau &= \frac{2dn}{c \times cos\theta_2} - \frac{2dsin\theta_1 sin\theta_2}{c \times cos\theta_2} \end{aligned} \tag{2.1}$$

where n is the refractive index of the ice/snow, θ_1 is the incidence angle, and θ_2 is the angle within the slab. τ_r is the extra distance traveled in the doubly reflected path inside the slab up and down. τ_f is the extra path traveled in the forward path compared to the doubly reflected path in the air. This distance can be deduced by drawing a perpendicular line from the point that the doubly reflected wave leaves the top interface to the direct path in air. c is the speed of light in free space and d is the thickness of ice/snow. The ice thickness can be estimated if this time delay can be measured accurately. This technique has the potential to find the thickness of any low-absorbing layered medium.

In the case of homogeneous and isotropic layer, (2.1) is simplified to the following equation: $\tau = \frac{2d}{c}\sqrt{n^2 - sin^2\theta_1}$. This approximation is valid for layer of fresh water ice formed over the lake. However, inside the snowpacks, the refractive index is a function of vertical position in the snowpack and is not constant. On the contrary to the fresh water ice, snow has a low thermal conductivity; therefore, the temperature distribution inside the snowpack is not constant either.

A photo of a layer of snow is shown in Fig. 2.2. The distribution of ice density inside the snow layer is shown in the figure.

For the snowpack, the delay can be calculated as given by (2.2).

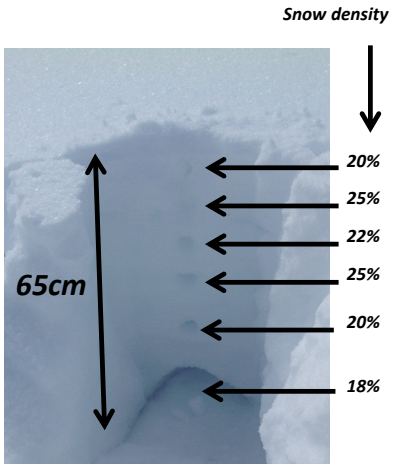

Figure 2.2: The distribution of ice density inside a thick layer of 65cm of snow measured at University of Michigan Biological Station, Pellston, MI.

$$\begin{aligned}
\tau &= \frac{2}{c}\left(\int \frac{n}{cos\theta_2}dz - \int \frac{sin\theta_1 sin\theta_2}{cos\theta_2}dz\right) \\
\tau &= \frac{2}{c}\int \frac{n}{cos\theta_2}(1 - sin^2\theta_2)dz \\
\tau &= \frac{2}{c}\int ncos\theta_2 dz \\
\tau &= \frac{2}{c}\int \sqrt{n^2 - sin^2\theta_1}dz, \qquad (2.2)
\end{aligned}$$

where we use the Snell's law ($sin\theta_1 = nsin\theta_2$) in this derivation.

Another important characteristics of snowpacks is the Snow Water Equivalent (SWE), which is defined as the equivalent depth of water when all the snow melts. In order to further proceed, we use the refractive index mixing formula ($n = v_1 n_1 + v_2 n_2$) for the refractive index of the snow. In this formula, v_1 and v_2 are the volume fraction of ice and air, respectively. The summation of $v_1 + v_2$ is equal to 1. n_1 and n_2 refers to the refractive index of ice and air, respectively. The refractive index of air is equal to 1 and the refractive index of ice is equal to $\sqrt{3.15}$.

SWE can be calculated by balancing the mass of water and ice inside the snowpack

as given by (2.3)

$$\rho_w SWE = \rho_i \int v_1 dz, \tag{2.3}$$

where ρ_w is the density of liquid water and is equal to $1[\frac{g}{cc}]$. ρ_i is the density of fresh water ice and is equal to $0.916[\frac{g}{cc}]$. Combining (2.3) by (2.2), the time delay can be calculated as a function of SWE as given by (2.4).

$$\begin{aligned}
\tau &= \frac{2}{c}\int n\sqrt{1-\left(\frac{sin\theta_1}{n}\right)^2}dz \\
\tau &\approx \frac{2}{c}\int \left(n - \frac{sin^2\theta_1}{2n}\right)dz \\
\tau &\approx \frac{2}{c}\int n dz \\
\tau &\approx \frac{2}{c}(n_2\int dz + (n_1-n_2)\int v_1 dz) \\
\tau &\approx \frac{2}{c}(n_2 d + (n_1-n_2)\frac{\rho_w}{\rho_i}SWE) \\
\tau &\approx \frac{2}{c}(d + 0.846 \times SWE),
\end{aligned} \tag{2.4}$$

where $\int dz = d$ and we use the low order Taylor expansion terms formulated as follows $\sqrt{1-x^2} \approx 1 - \frac{x^2}{2}$. Equation 2.4 shows that the delay is approximately is equal to the thickness of the snowpack with a small error, which is a function of SWE. We are analyzing the dry snow with small water content, which guarantees that the SWE is much smaller than the thickness of the layer and can be ignored. The dependence to the angle of incidence is small and of second order ($O(sin^2\theta_1)$). In the case that the refractive index of the snowpack is constant $n = 1 + 0.846SWE/d$ and the delay is given by (2.5).

$$\tau = \frac{2}{c}(d + 0.846\ SWE)\sqrt{1 - \frac{sin^2\theta_1}{(1 + 0.846\ SWE/d)^2}}. \tag{2.5}$$

2.2.3 Ripple analysis

For simplicity, we consider a homogeneous and isotropic layer with normal incidence. In this case, the microwave transit time delay is equal to $\tau = \frac{2nd}{c}$. The round trip distance of the doubly reflected path is given by (2.6).

$$\frac{c}{n}\tau = 2d = p\lambda_p, \tag{2.6}$$

where p is the on-negative integer and λ_p is a wavelength in the slab corresponding to maximum constructive interference between the direct ray and the delayed ray. The frequency that corresponds to λ_p is $f_p = c/n\lambda_p$. In the frequency domain, the separation between adjacent peaks in the brightness temperature, the periodicity of the ripples, is given by 2.7.

$$\begin{aligned}
\Delta f &= f_{p+1} - f_p \\
\Delta f &= \frac{c}{n\lambda_{p+1}} - \frac{c}{n\lambda_p} \\
\Delta f &= \frac{c}{n}\left(\frac{p+1}{(p+1)\lambda_{p+1}} - \frac{p}{p\lambda_p}\right) \\
\Delta f &= \frac{c}{n}\left(\frac{p+1}{c\tau/n} - \frac{p}{c\tau/n}\right) \\
\Delta f &= \frac{1}{\tau}
\end{aligned} \tag{2.7}$$

Δf is the same regardless of whether it is measured between maxima (points of maximum constructive interference) or between minima (points of maximum destructive interference). In the case of minima, p should be replaced by $p - \frac{1}{2}$ in equation (2.7).

2.2.4 Forward model

The power per resolution bandwidth received at the back end of a radiometer is given by 2.8.

$$P(\omega) = kT_{SYS}B_R G(\omega) \tag{2.8}$$

where k is Boltzmann's constant, T_{SYS} is the system temperature, measured in Kelvin, B_R is the resolution bandwidth, and $G(\omega)$ is the radiometer gain as a function of angular frequency, ω. The system temperature itself is the summation of the receiver temperature, T_{REC}, and the antenna temperature, T_A, both referenced to the antenna aperture ($T_{SYS}(\omega) = T_{REC}(\omega) + T_A(\omega)$). An explicit dependence on frequency is included in this expression. When looking to the sky, $T_A(\omega) = T_{sky}(\omega)$. The sky temperature is rather low and is not a very strong function of frequency from 1 to 10 GHz. When we are looking at an object, the antenna temperature is the brightness emitted by the object filling the main beam, given by equation 2.9.

$$T_A(\omega) = e(\omega)T_{object} \tag{2.9}$$

where $e(\omega)$ is an emissivity, and T_{object} is the physical temperature of the object, which is independent of frequency. Since we are operating in the lower microwave frequencies (somewhere between 1 and 15 GHz), we can consider the atmosphere lossless when looking downwards on the object.

For our measurements, we have, in addition to the sky, two common objects: the slab (ice over water, or dry snow pack over ground), and microwave absorber. For the absorber, the object temperature is substantial (ie. $T_{object} = T_{abs} >> T_{sky}$) and the emissivity is assumed to be near unity, or at least without much frequency dependence (ie. $e_{abs}(\omega) = 1$). The slab target has a well defined physical temperature for ice over water, namely $T_{object} = T_{slab} = 273K$, while it is at most near freezing for snow over ground.

The emissivity of the layered media can be found by first finding the reflectivity of the layered media and then calculating the emissivity by $e = 1 - \Gamma$, where Γ is the reflectivity of the layered media and is equal to $|R_1|^2$. R_1 is given by equation 2.10. In the following, the emissivity of a single layer and bilayer media is analyzed.

Generally for a multi layer structure the reflectivity can be calculated using a transfer matrix method by an iterative recursive algorithm (57). The reflectivity can be given by equation 2.10.

$$R_i = \frac{r_i + R_{i+1}e^{-j\omega\tau}}{1 + r_i R_{i+1} e^{-j\omega\tau}},\ i = M, M-1, ..., 1, \tag{2.10}$$

where r_i is the reflection coefficient at each interface calculated by Fresnel equation. The interfaces are enumerated from top to bottom in this order $(1, 2, ..., M+1)$. The reflection can be calculated by first using $R_{M+1} = r_{M+1}$ and then recursively solving equation 2.10.

For a slab $M = 1$ and for a bilayer media $M = 2$. Therefore, the emissivity of a single layer can be calculated as given by equation 2.11 (78; 11).

$$e(\omega) = \frac{(1 - |r_1|^2)(1 - |r_2|^2)}{1 + |r_1|^2|r_2|^2 + 2|r_1||r_2|cos(\omega\tau)}. \tag{2.11}$$

For a lossy media r_i should be replaced by r_i/L, where L is the extinction of the slab.

For a bilayer structure, using the same procedure, the emissivity can be given by equation 2.12.

$$
\begin{aligned}
r_r &= 1 + |r_1|^2|r_2|^2 + |r_1|^2|r_3|^2 + |r_2|^2|r_3|^2 \\
r_s &= 2|r_2||r_3|(1+|r_1|^2)cos(\omega\tau_2) + 2|r_1||r_2|(1+|r_3|^2)cos(\omega\tau_1) \\
e_b &= \frac{(1-|r_1|^2)(1-|r_2|^2)(1-|r_3|^2)}{r_r + r_s + 2|r_1||r_3|cos(\omega(\tau_1+\tau_2)) + 2|r_1||r_3||R_2|^2cos(\omega(\tau_1-\tau_2))}, \quad (2.12)
\end{aligned}
$$

where τ_1 and τ_2 are the microwave transit time delay in each layer separately. e_b is the emissivity of the bilayer structure. In the autocorrelation response, we expect to see peaks corresponds to each layer thickness as well as the difference and summation of the layers thicknesses. For structures with more than two layers, the transfer matrix method can be used to find the emissivity.

From these two equations 2.11 and 2.12, we found that the term of interest is in the denominator of the emissivity, therefore, $1/e(\omega)$ is of interest. We will show later that this inversion helps us to minimize the impact of radio frequency interference (RFI) in our system response. RFIs are due to the signals transmitted around us such as cell phone signals, WiFi signal, bluetooth signals, Zigbee standard signals, ... This inversion reduce the impact of these signals in the autocorrelation response of our system.

The simulation result for autocorrelation response of a two layer media with time delay of 5ns and 8ns using the emissivity and inverse of emissivity are shown in Fig 2.3. The bilayer media composed of snow over lake ice. The scenario of snow over ice is compared to only ice. The inverse of emissivity is used and the result is shown in Fig. 2.4. The delay peak for the ice only layer is 1.85dB higher than that of snow over ice layer. This reduction is due to the close refractive index of snow and air. The snow layer works as a matching layer between ice and air and the delay peak goes down.

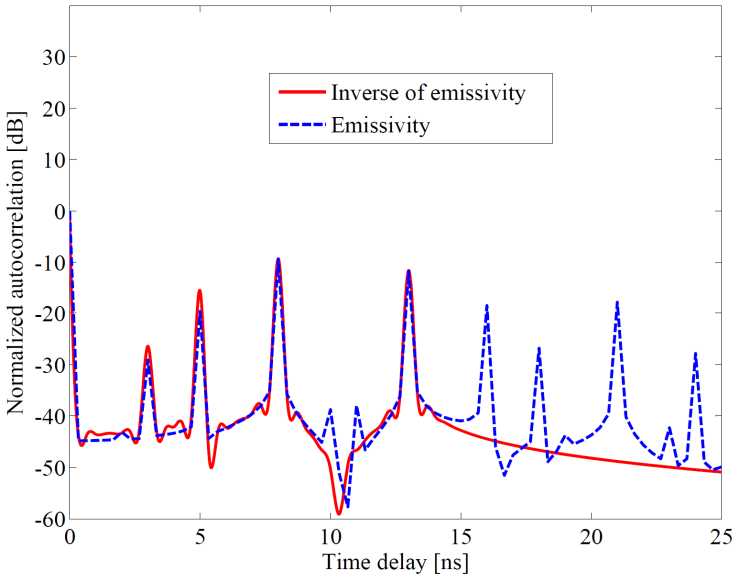

Figure 2.3: The autocorrelation response of a bilayer medium with time delays of 5ns and 8ns using the emissivity (dashed blue line) and inverse of emissivity (solid red line).

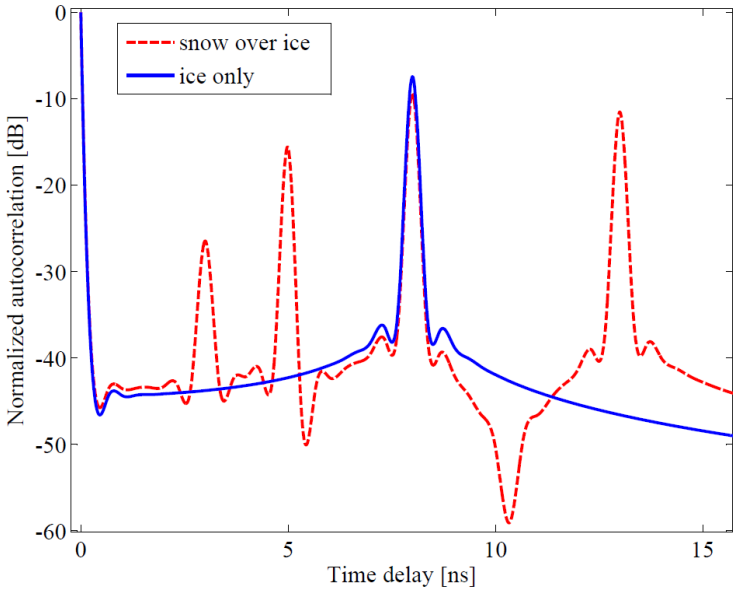

Figure 2.4: The autocorrelation response of a bilayer medium composed of snow over ice (dashed red line) compared with that of ice layer only (solid blue line) with time delays of 5ns and 8ns using the inverse of emissivity.

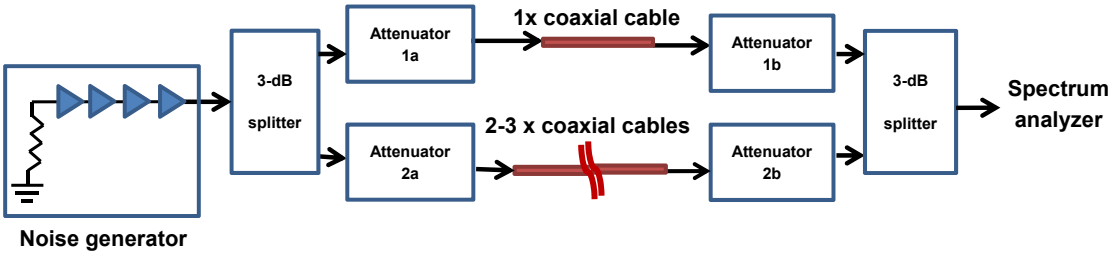

Figure 2.5: The block diagram of the low-order model in the frequency domain.

2.3 Modeling of the wideband autocorrelation radiometry technique

Wideband autocorrelation radiometer (WiBAR) operates based on analyzing the temporal autocorrelation of the received brightness temperature. The wide-bandwidth of WiBAR provides higher dynamic range and reduces the required integration time to extract the information. WiBAR can be realized in the time-domain (22; 23) or frequency domain. We explored both implementation methods in the Subsections 2.3.2 and 2.3.1. Then, WiBAR optimal design procedure and comprehensive sensitivity analysis are investigated.

2.3.1 Proof of concept- frequency domain hardware simulations

The second implementation of WiBAR is by designing the radiometer in the spectral domain and use Wiener-Khinchin theorem to estimate the autocorrelation pattern of the incident brightness temperature. This theorem states that the autocorrelation pattern is the inverse Fourier transform of the power spectral density. Compared to the time domain WiBAR, the second approach can be easily implemented directly in hardware. The second advantage of the power spectral implementation is in the calibration procedure, which is straightforward and is capable of almost removing the WiBAR signature in the post processing module.

In order to examine the possibility of frequency domain implementation, we have

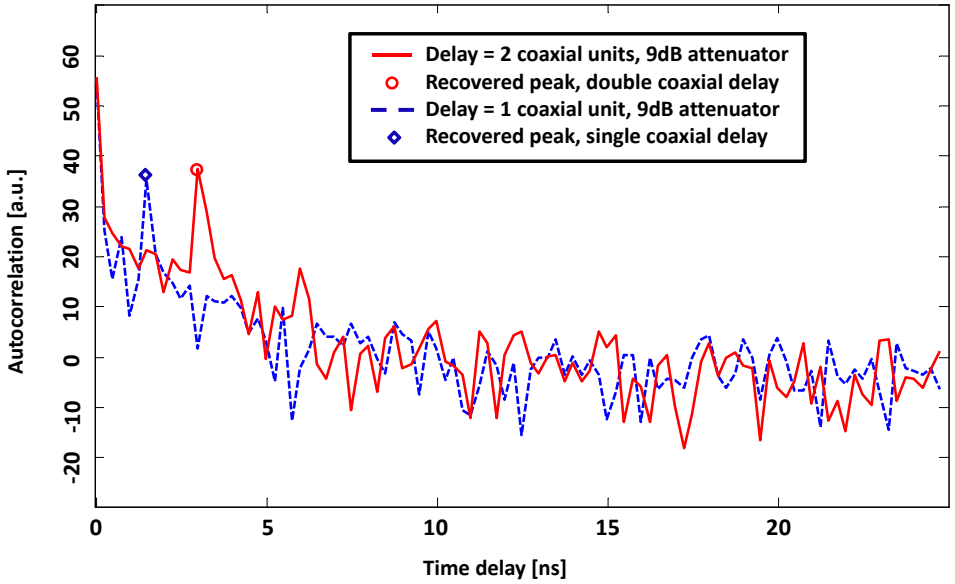

Figure 2.6: The autocorrelation response of the detected waveforms for one (blue dashed line) and two unit delays (red solid line). The doubly reflected path is attenuated $9dB$ more than the direct path.

designed two microwave circuits that mimic the physics of the layered media. The first model only captures the first peak and we call it low-order model. The second model considers multiple reflection inside the layer and we call it high-order model. The low-order model is shown in Fig. 2.5. The inherent thermal noise of a matched load is amplified using a series of cascaded noisy amplifiers. The amplified noise then splits into two branches corresponding to direct path and the doubly reflected path. $1.5dB$ attenuators (attenuator $1a$ and $2a$ in Fig. 2.5) are used to model the attenuation in each path of the brightness temperature. The time delay is also modeled by tuning the extra length of the coaxial cable in the delayed path. The identical noise waveforms are then merged into one signal and fed to a spectrum analyzer. Detecting the relative time delay of the longer path is equivalent to detecting the thickness of the simulated layered medium. Since the longer path experiences more attenuation, the attenuation in the longer path (attenuator $2b$ in Fig. 2.5) is larger than the one in the shorter path (attenuator $1b$ in Fig. 2.5) by $9dB$. The difference between the amplitude of the zero-lag peak and the doubly reflected path peak is $9dB$. A reference

data required for calibration was obtained by disconnecting the coaxial units from the front end attenuators, providing infinite attenuation and no delay for the doubly reflected path. As a result of large attenuation, the open ends of both the splitter and combiner appear to be matched, preventing degradation of voltage standing wave ratio (VSWR) in the shorter path. Each coaxial unit delay is expected to give about $1.5ns$ of unit delay. The results of autocorrelation, which is equal to inverse Fourier transform of the power spectral data is shown in Fig. 2.6 for a single unit delay and two unit delays. Fig. 2.6 shows the successful reconstruction of the time delays (the hollow diamond and circle), which are equal to $1.5ns$ and $3ns$, as expected. The cables have Teflon with dielectric constant of about 2.2 as internal dielectric, therefore, the delay for a foot long cable is equal to $delay = \frac{30.48\times10^{-2}\times\sqrt{2.2}}{3.0\times10^{8}} = 1.507ns$. Therefore, each nanosecond delay corresponds to about $20cm$ of cable length.

For better understanding of the frequency domain implementation, we investigate the dependence of autocorrelation response to the parameters of the model. The noise floor and hence sensitivity of the measurement depends on the ratio of the resolution bandwidth to the video bandwidth and also the number of averaging applied to the captured data. The resolution and video bandwidths are Spectrum analyzer characteristics that defined later in this section at Subsection 2.4.0.2. The autocorrelation response of a 3ns delay line is shown both for a single measurement and for the average of 100 measurements. The variance of the noise should go down by $1/N$, where N is the number of traces used for averaging. However, averaging and video bandwidth are both low frequency operators. Therefore, by interchanging the role of time and frequency, the low time (small delay times) components of autocorrelation response should pass without change. However the high time components (larger delay times) should pass with attenuation. Therefore, variation in the small delay time components in the autocorrelation response is unchanged with or without averaging. However, the variation in the high delay time components is much smaller after

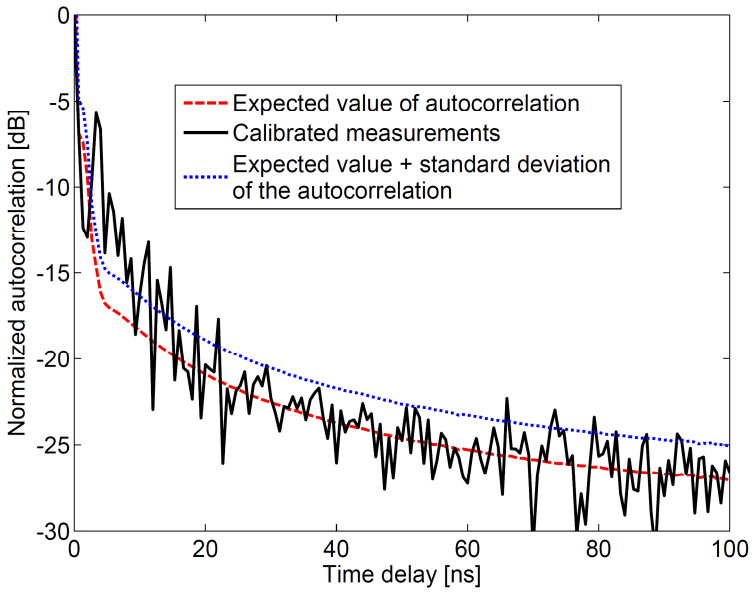

Figure 2.7: The autocorrelation response of the low order microwave circuit model for single measurement (solid black line). The expected value of the autocorrelation response (dashed red line) and the summation of the expected value and the standard deviation of the autocorrelation response (dotted blue line) are also included.

applying the averaging operator. The autocorrelation response for a 3ns delay line with and without averaging are shown in Figs. 2.7 and 2.8. The expected value and the summation of the expected value and standard deviation are also highlighted for better understanding of the autocorrelation response. Both of the figures are shown in Fig. 2.9 for comparison.

The power spectrum is shown in Fig. 2.10 for both a single measurement and average of 100 measurements. The noise is smaller in the averaged curve.

The power spectrum and autocorrelation response for a 6ns delay line is shown in Figs. 2.11 and 2.12, respectively.

The amplitude of the delay peak goes down by adding more and more attenuation. The autocorrelation response and a function of time delay is shown in Fig. 2.13 for three scenarios. No attenuator added, 1dB attenuators are added on both branches, and 1dB and 6dB attenuators added.

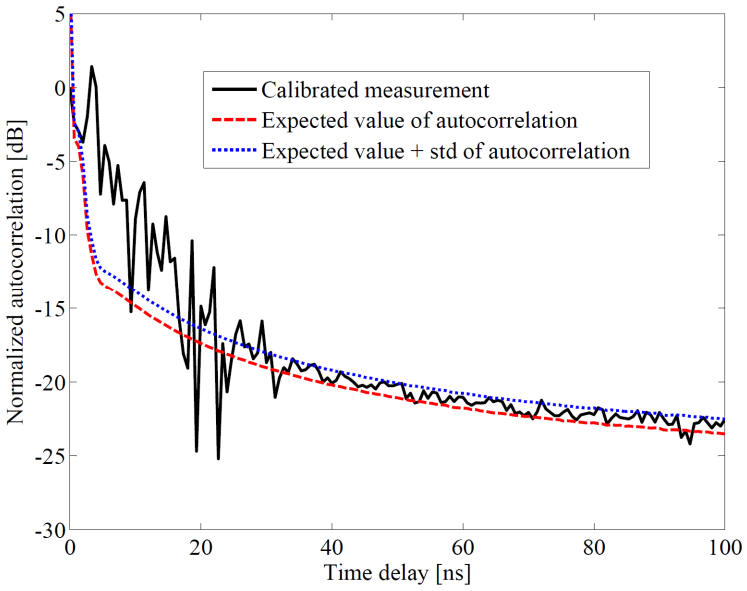

Figure 2.8: The autocorrelation response of the low order microwave circuit model for the average of 100 measurements (solid black line). the expected value of the autocorrelation response (dashed red line) and the summation of the expected value and the standard deviation of the autocorrelation response (dotted blue line) are also included.

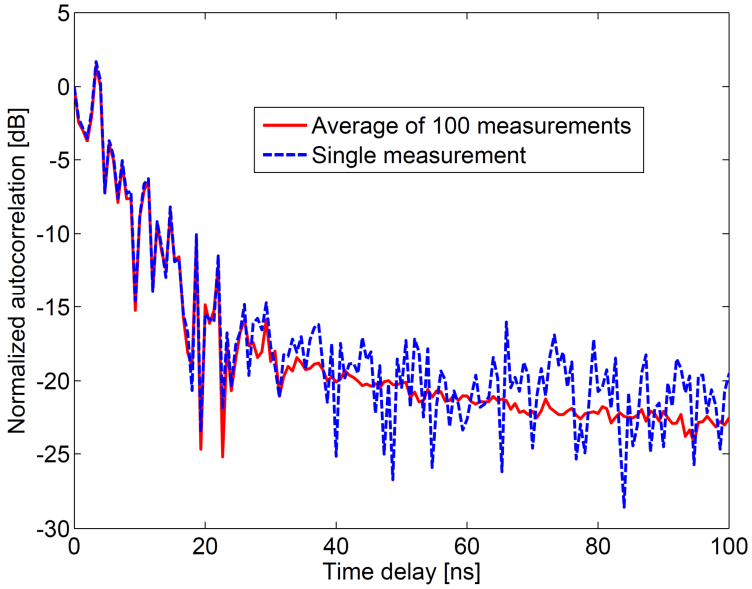

Figure 2.9: The autocorrelation response of the low order microwave circuit model for the average of 100 measurements (solid red line) and the single measurement (dashed blue line) for 3ns delay line.

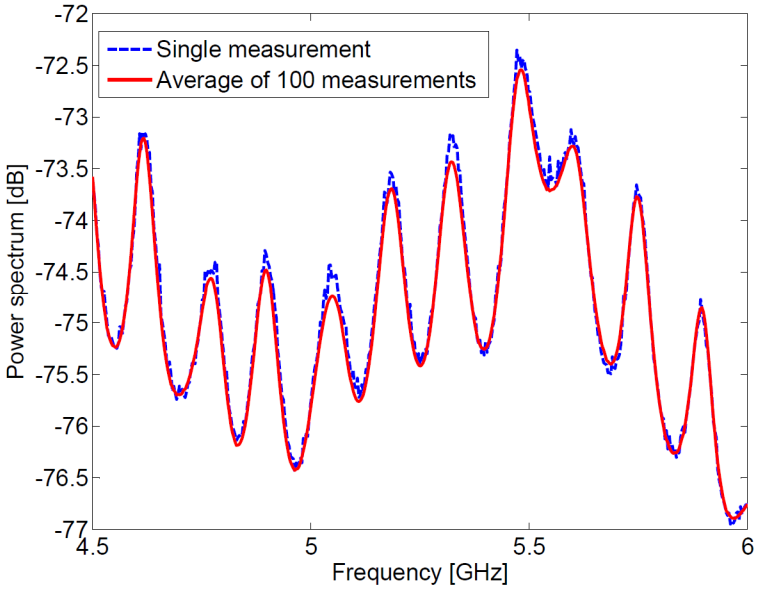

Figure 2.10: The power spectrum of the low order microwave circuit model for the average of 100 measurements (solid red line) and single measurement (dashed blue line) for 3ns delay line.

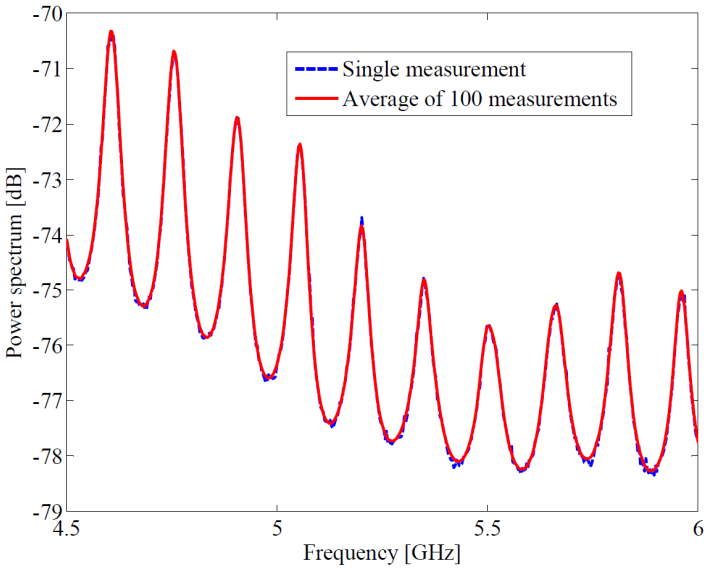

Figure 2.11: The power spectrum of the low order microwave circuit model for the average of 100 measurements (solid red line) and single measurement (dashed blue line) for 6ns delay line.

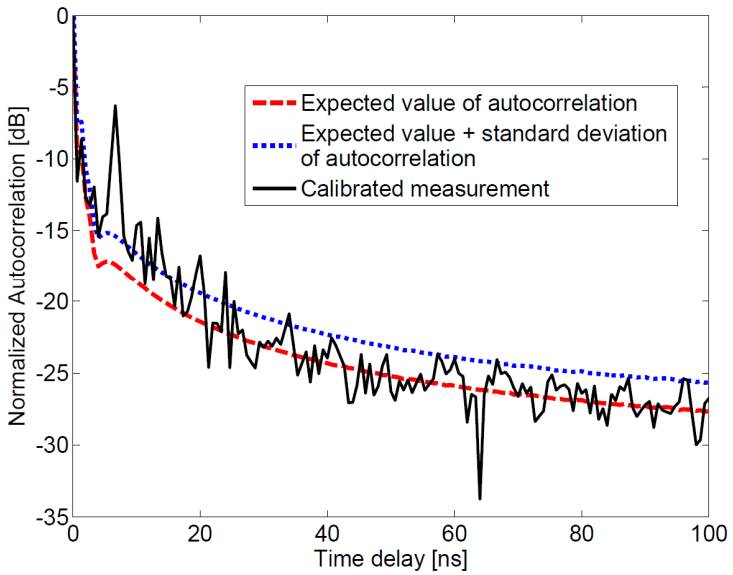

Figure 2.12: The autocorrelation response of the low order microwave circuit model for single measurement (solid black line). the expected value of the autocorrelation response (dashed red line) and the summation of the expected value and the standard deviation of the autocorrelation response (dotted blue line) are also included. 6ns delay line is used.

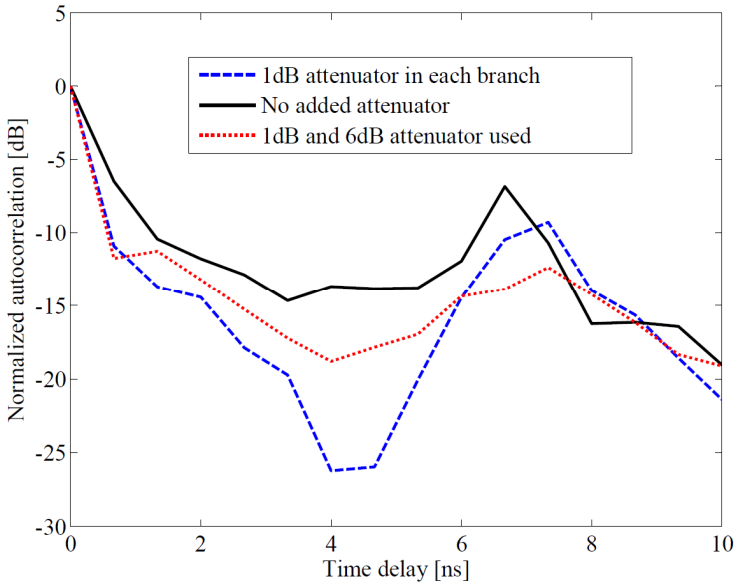

Figure 2.13: The autocorrelation response of the low order microwave circuit model for single measurement with no attenuator added (solid black line), two 1dB attenuators added (dashed blue line), and 1dB and 6dB attenuators added. 6ns delay line is used.

The block diagram of the high-order model is shown in Fig. 2.14(a). The loop, which is formed by two 180 degree hybrid couplers, plays the role of multiple inter-layer reflections. In this schematic, the upper hybrid coupler models the water-ice or snow-terrain interface. The lower hybrid coupler models the ice-air or snow-air interface. The amplified input noise source represent the emission of the underlying medium that can be water or terrain. The rotation of the signal inside the loop is similar to multiple internal reflection inside the layered media. The time delay is due to the microwave transit time inside the transmission lines forming the loop. The reflected wave is 180 degree out of phase with the transmitted signal, this phase shift implemented by applying the input signal to the delta port of the 180 degree hybrid coupler. The input signal splits into two signals with 180 phase difference. The in-phased components of the upper hybrid coupler enters the delta port of the lower hybrid coupler. The signal then splits into two paths. The in-phase component representing transmission in air toward the radiometer enters the spectrum analyzer. The 180 out of phase signal rotate in the loop. This signal represents the internal reflection at the ice-air or snow-air interface, which remains inside the layer.

This high order model has been implemented and tested in the lab and also in open air. In the open air scenario, the termination on the right side of the bottom coupler is replaced by an antenna detecting the cold sky. In the open-air test we have removed the amplifier chain to mimic the actual scenario. The autocorrelation response of the calibrated measurement for the case of no attenuator measured in the lab is shown in Fig. 2.14 (b). The multiple peaks are due to the higher order reflection inside the layered medium. The total cable length of $4ft = 1.22m$ is chosen in this case. The electric length of the adapters as well as the couplers should also be considered in the calculation of total electric length. The autocorrelation response shows the overall length of $4.25ft = 1.3m$, which is very close to the expected value considering the electric path inside the hybrid couplers and adapters. The calibration procedure is by

measuring the test scenario, in which the left branch of the loop has been disconnected and the cables terminated appropriately. The calibration measurement only considers the direct path signal.

We have implemented this technique for several different-length delay lines and the peak temporal location is changing by varying the length of the loop. The power spectrum and the autocorrelation response of these delay lines are as shown in Figs 2.15, 2.16, 2.17, 2.18, 2.19, 2.20, 2.21, 2.22, 2.23, and 2.25.

The impact of system bandwidth on the autocorrelation response is also investigated. In the first measurement, we use the whole bandwidth of $7 - 10$GHz, however in the second measurement, we just use half of the bandwidth $7 - 8.5$GHz. The frequency resolution of the half bandwidth measurement is better than the full bandwidth resolution. The resolution in the frequency domain translates to the higher autocorrelation time delay coefficients. The sensitivity of the system is also a function of bandwidth and is $3dB$ better for the full bandwidth measurement as shown in Fig. 2.41.

The loop structure extended by adding extra 180 degree hybrid couplers to model wave propagation in multilayer media. Each extra hybrid coupler add one more loop and equivalently add one more layer to the model. The power spectrum of a bilayer structure is shown in Fig. 2.26. The ripples are modulated due to the presence of two set of frequencies. The autocorrelation response of the bilayer structure compared to a single layer is shown in Fig. 2.27. The autocorrelation response of a three layer media as a function of microwave delay time is shown in Fig. 2.28. The one layer structure consist of 6ns delay line. The delay line consists of the total length of the cable in a loop. The bilayer structure has another loop with 18ns total length. The peak at 12ns is the combination of 2×6 and $18 - 6$. The three layer structure is similar to the bilayer structure with one extra loop with total delay time of 18ns.

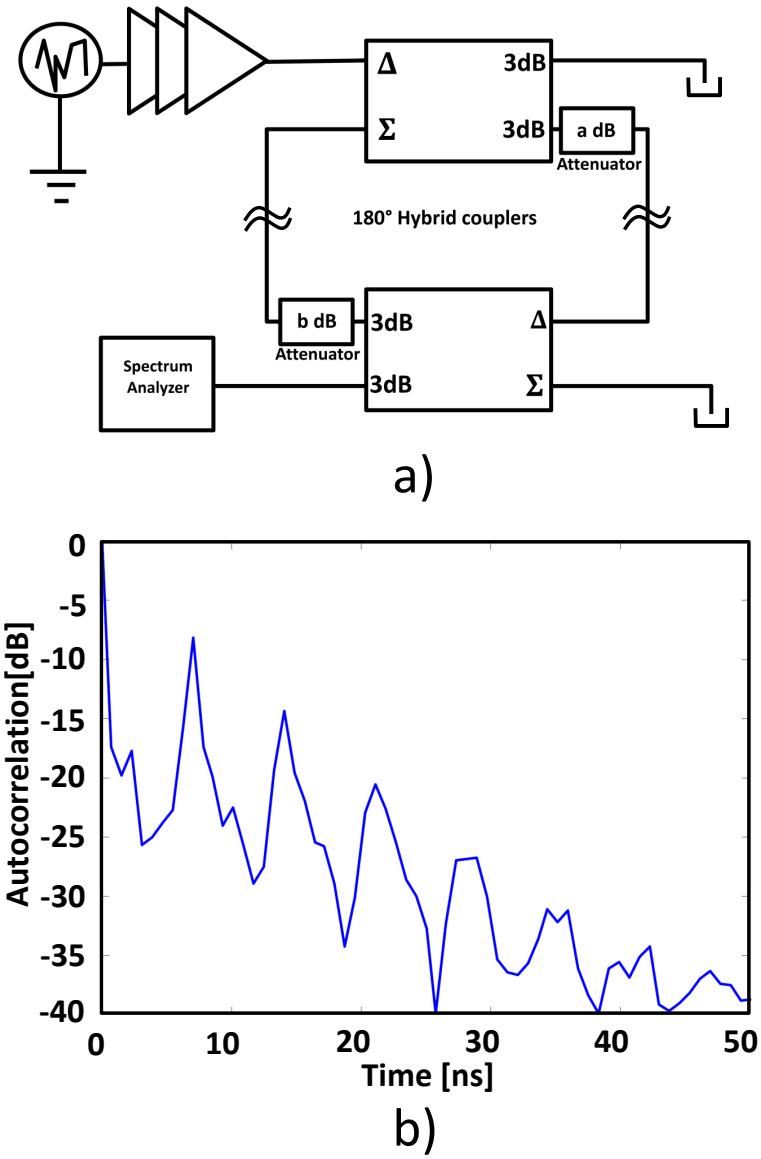

Figure 2.14: (a) The schematic of high-order microwave circuit model of the WiBAR. (b) The autocorrelation response of the high-order microwave circuit model demonstrating the delayed peaks measured in the lab.

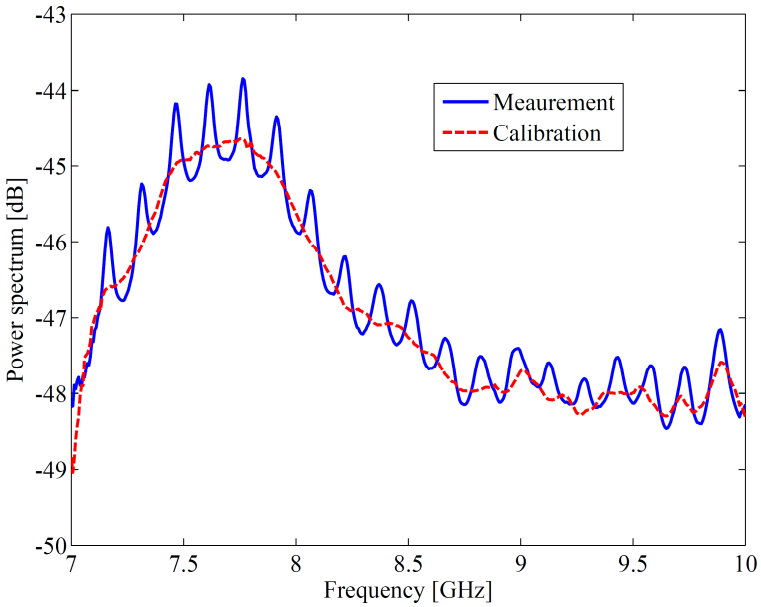

Figure 2.15: The power spectrum of the high order microwave circuit model (solid blue line) and calibration signal (dashed red line) for 6ns delay line measured outside.

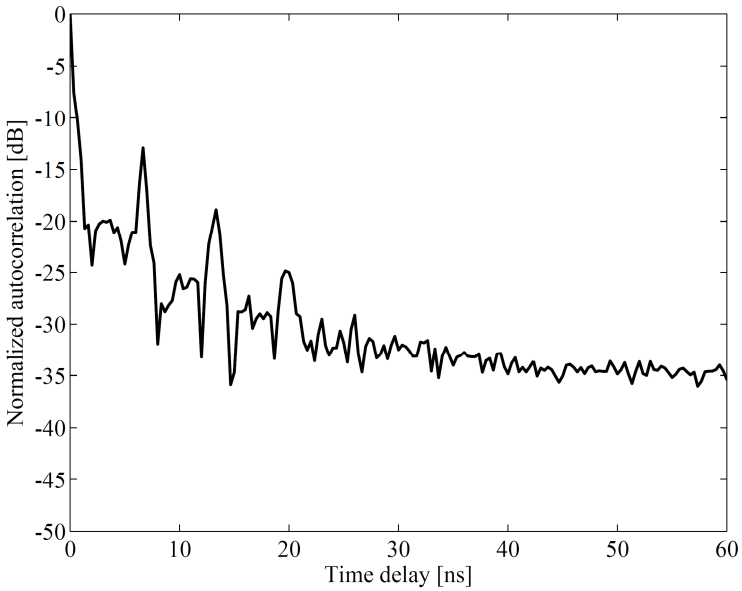

Figure 2.16: The autocorrelation response of the high order microwave circuit model for 6ns delay line measured outside.

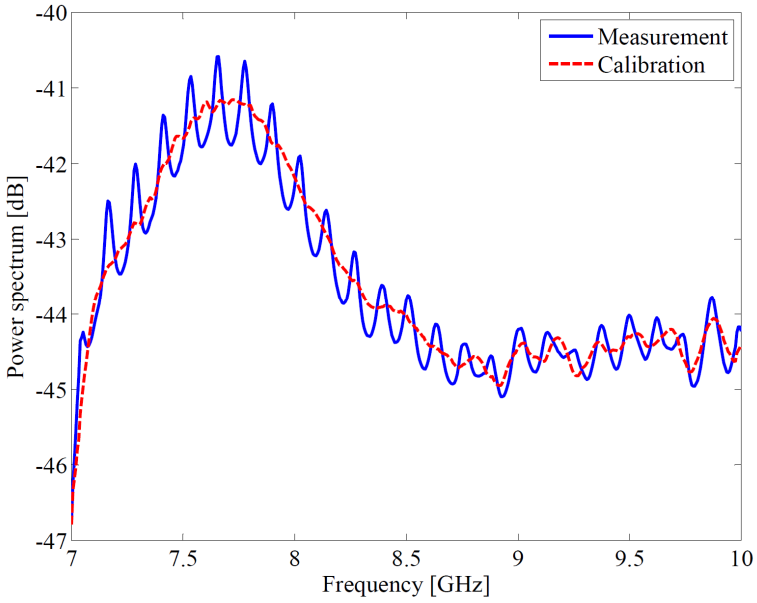

Figure 2.17: The power spectrum of the high order microwave circuit model (solid blue line) and calibration signal (dashed red line) for 8.5ns delay line measured outside.

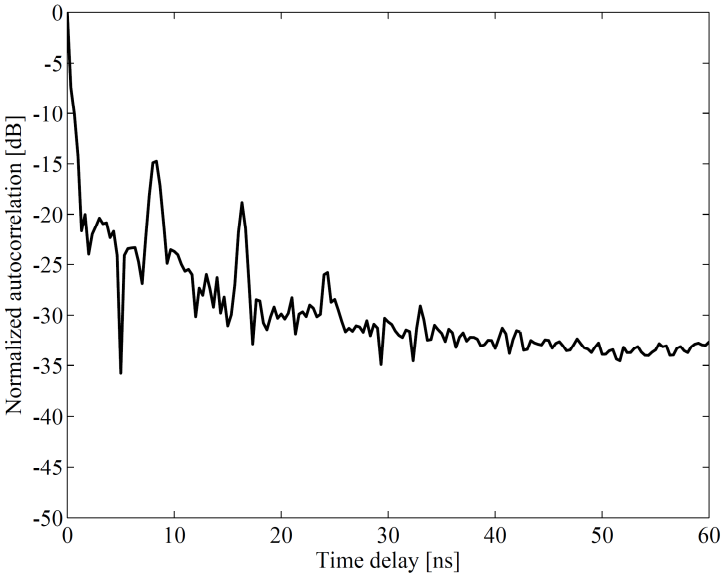

Figure 2.18: The autocorrelation response of the high order microwave circuit model for 8.5ns delay line measured outside.

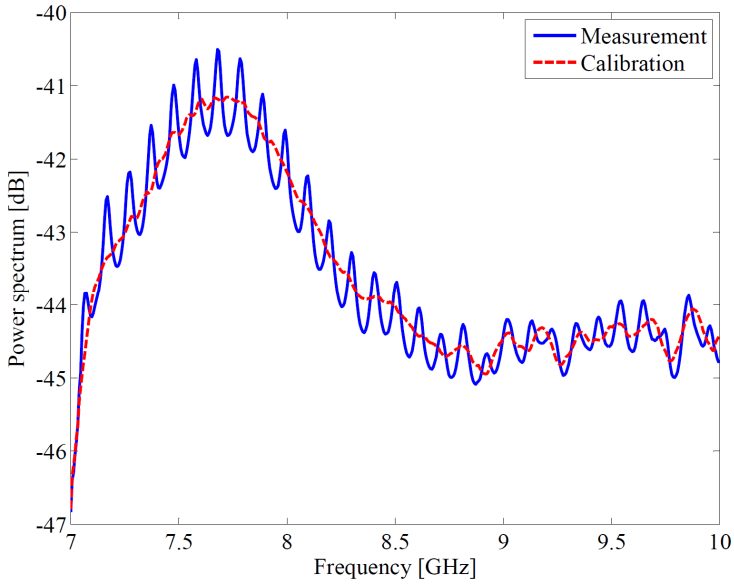

Figure 2.19: The power spectrum of the high order microwave circuit model (solid blue line) and calibration signal (dashed red line) for 10ns delay line measured outside.

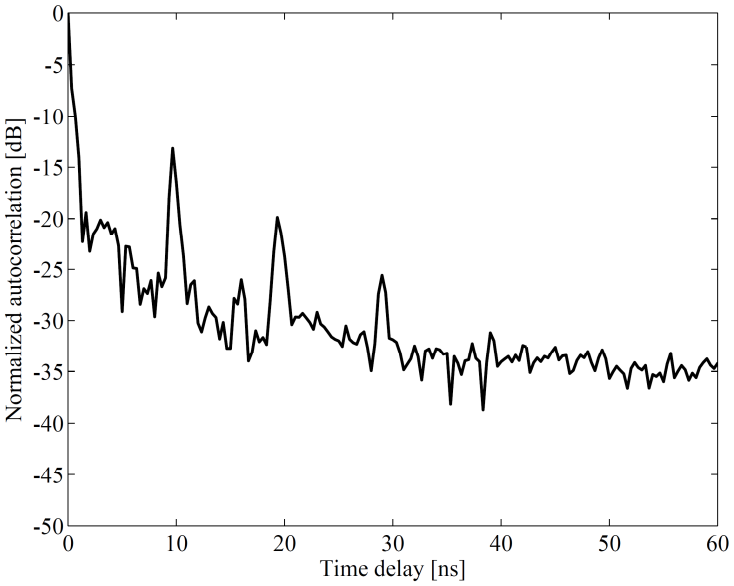

Figure 2.20: The autocorrelation response of the high order microwave circuit model for 10ns delay line measured outside.

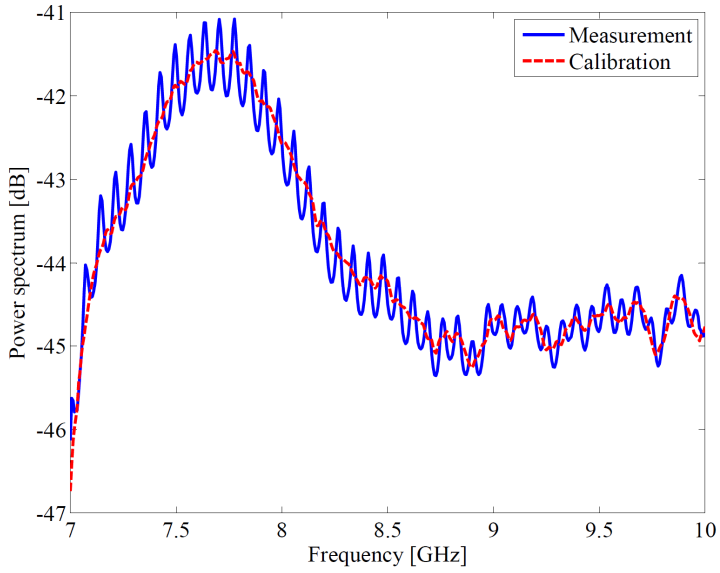

Figure 2.21: The power spectrum of the high order microwave circuit model (solid blue line) and calibration signal (dashed red line) for 12ns delay line measured outside.

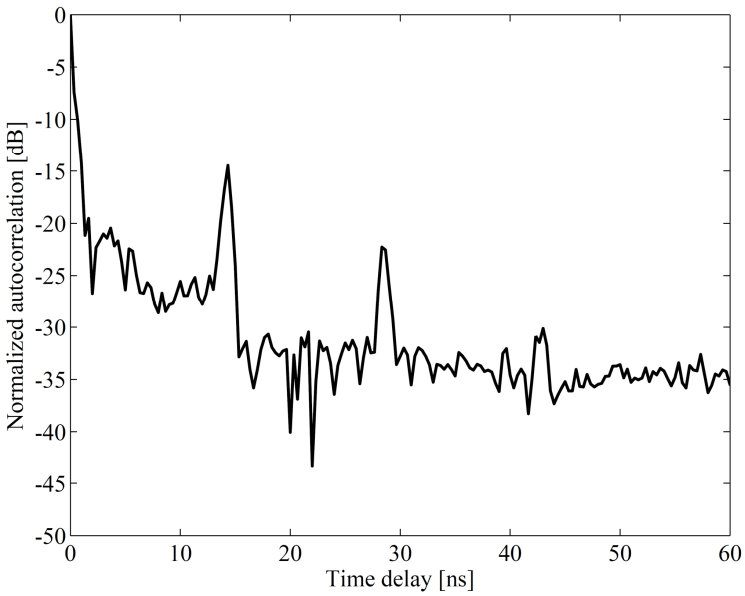

Figure 2.22: The autocorrelation response of the high order microwave circuit model for 12ns delay line measured outside.

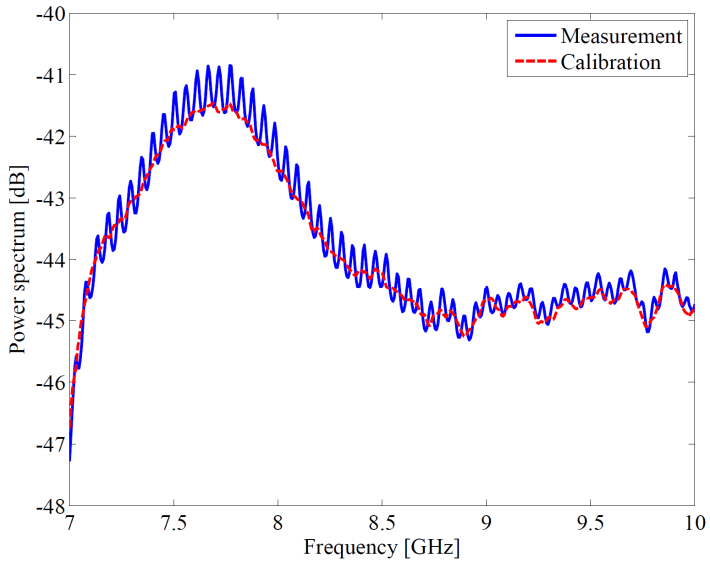

Figure 2.23: The power spectrum of the high order microwave circuit model (solid blue line) and calibration signal (dashed red line) for 18ns delay line measured outside.

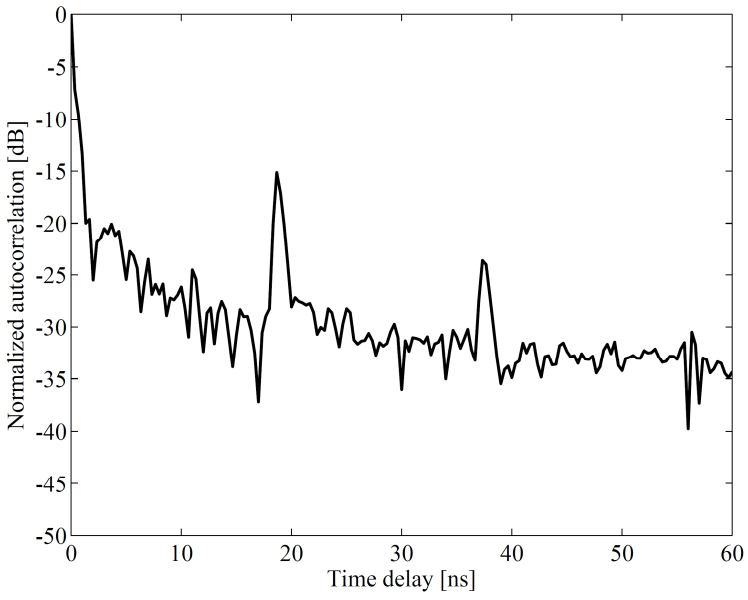

Figure 2.24: The autocorrelation response of the high order microwave circuit model for 18ns delay line measured outside.

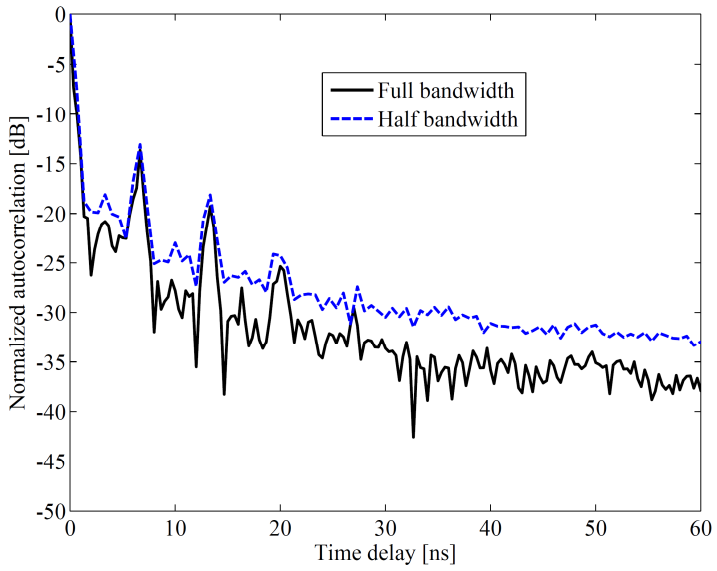

Figure 2.25: The autocorrelation response of the high order microwave circuit model for 6ns delay line measured outside for full bandwidth, $7-10$GHz, (solid black line) and half bandwidth, $7-8.5$GHz, (dashed blue line).

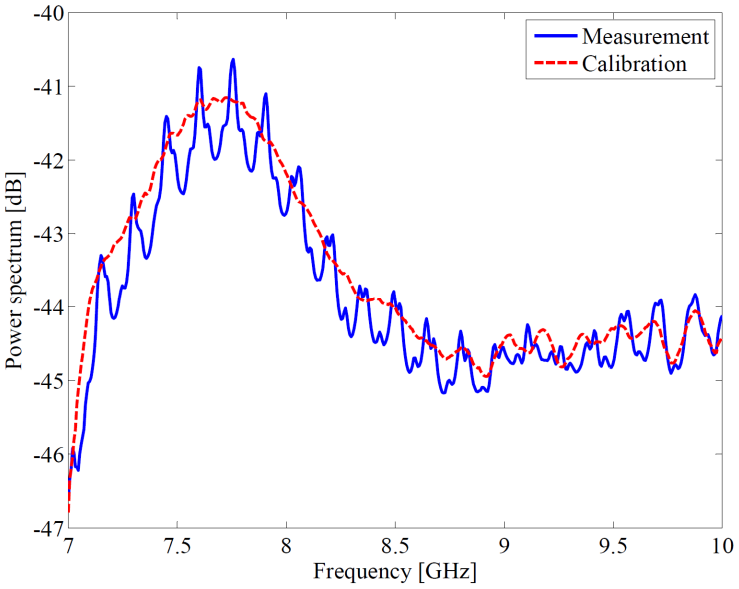

Figure 2.26: The power spectrum of the high order microwave circuit model for a bilayer structure (solid blue line) and calibration signal (dashed red line) for 6ns and 18ns delay line measured outside.

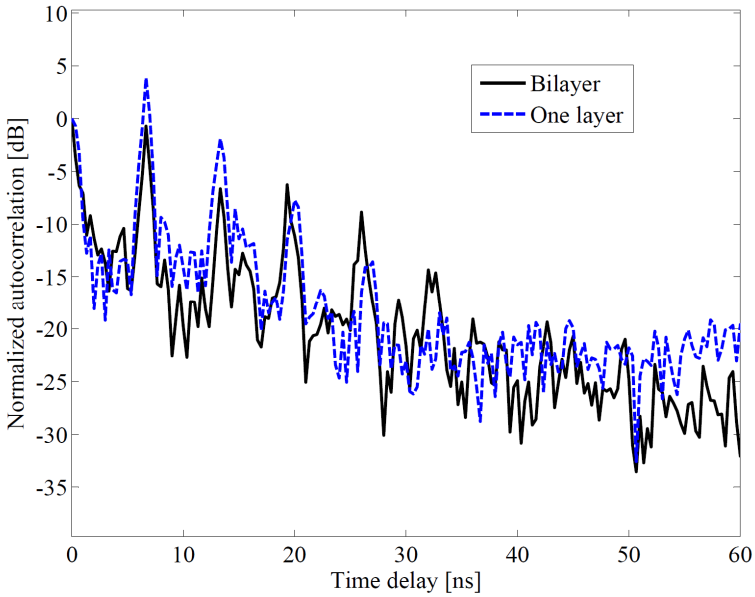

Figure 2.27: The autocorrelation response of the high order microwave circuit model for single layer (dashed blue line) and bilayer (black solid line) structure for 6ns and 18ns delay line measured outside.

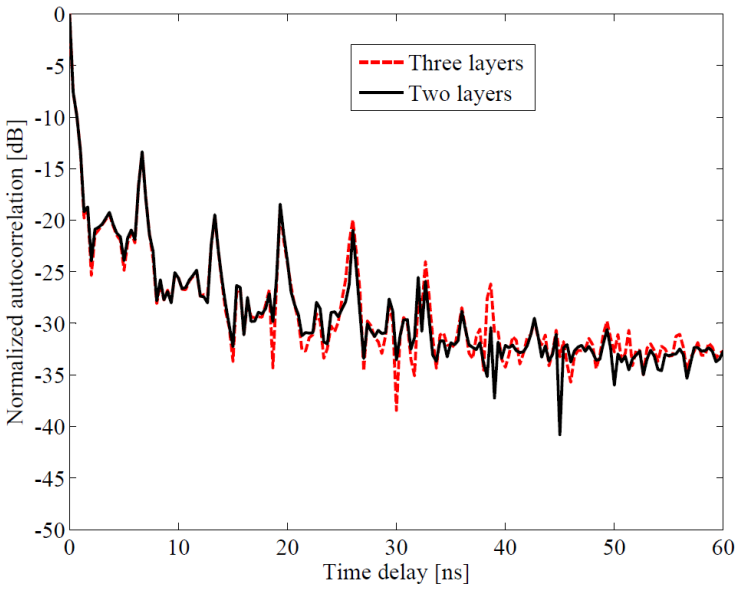

Figure 2.28: The autocorrelation response of the high order microwave circuit model for two (black solid line) and three layer (dashed red line) media with 6ns, 18ns, and 18ns delay line measured outside.

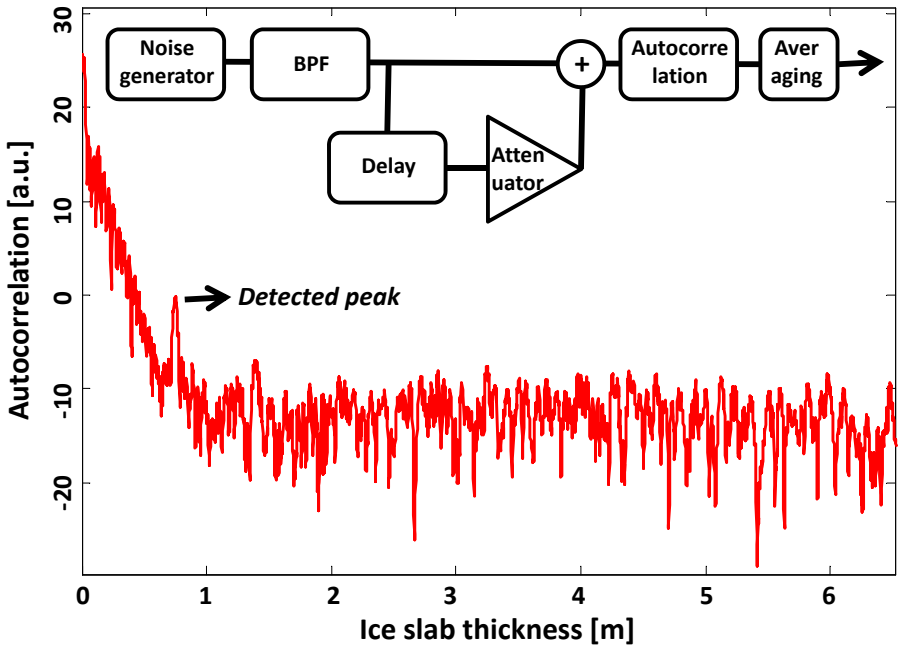

Figure 2.29: The software simulated recovery process of the autocorrelation radiometer in time-domain for a 75cm thick ice using a long integration time and a sharp bandpass filter (BPF). The block diagram of the process is shown in the inset.

2.3.2 Proof of concept- time domain software/hardware simulation

The time domain realization of WiBAR is by processing the autocorrelation pattern of the received signal, called time-domain setup. The block diagram of the signal path in time-domain simulation is shown in the inset of Fig. 2.29. The blackbody radiation of the background medium (water or soil) is modeled by a Gaussian noise generator due to central limit theorem. The signal then passes through a band pass filter (BPF). The filtered noise travels through two different paths to mimic the direct path and doubly reflected path. The autocorrelation of the combined signal is then applied to an averaging stage to diminish its noise level. A test scenario of a $75cm$ ice sheet over water is considered and the simulated waveform of the emitted signal is fed through the block diagram shown in the inset of Fig. 2.29. The bandpass filter is given a response similar to the filter used in the second implementation of WiBAR later in this section. The integration time and the attenuation of the

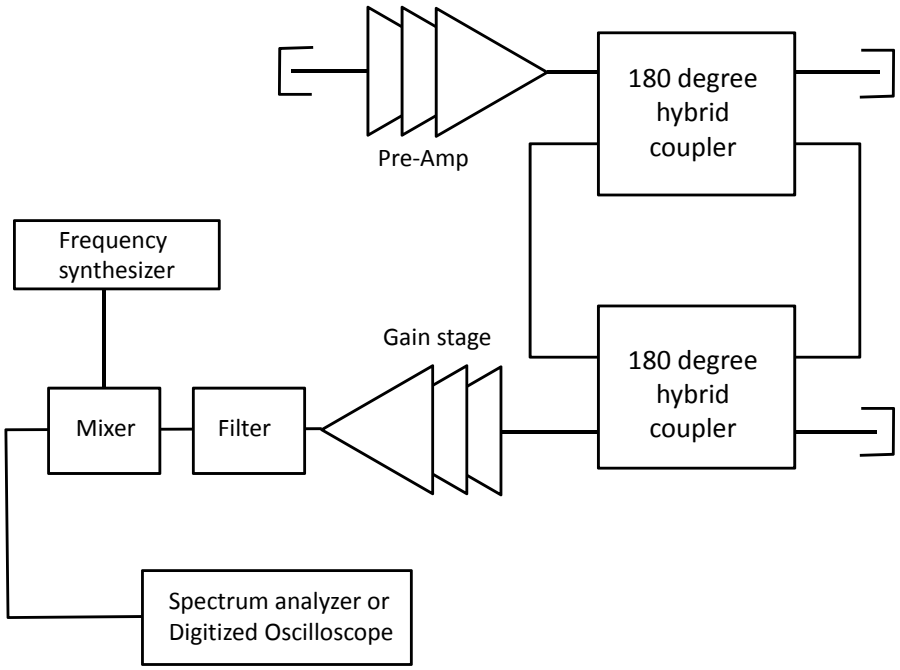

Figure 2.30: The schematic of the modeled microwave circuit for both time and frequency domain measurements.

doubly reflected wave are chosen as the worst case scenario to be $1\mu s$ and $-25dB$, respectively. The hardware implementation of this technique requires a digital signal processing (DSP) board with a very high speed analog to digital converter (ADC). In our desired frequency range of operation, finding a super fast ADC is power hungry, readily available, but expensive.

We have also implemented this idea in the time domain in hardware. The schematics of the microwave circuit model is shown in Fig. 2.30. The amplified input noise is generated by terminating a chain of amplifiers with a matching load terminator. The thermal noise of the load, which is proportional to the ambient temperature, is amplified by a chain of amplifiers. In order to operate at the linear gain operational regime and for stability an attenuator is also added in the path in between the amplifiers. The generated noise then enter the 180 degree hybrid coupler loop structure. This structure has been explained thoroughly in the previous subsection.

The output signal is then amplified and properly filtered in the frequency range of $4 - 6.5$GHz. The signal then down convert to $0 - 2.5$GHz frequency band using a mixer and a frequency synthesizer tuned at 4GHz. The signal then enters a digitized oscilloscope. The digitized O'scope has a bandwidth of 1.5GHz. In order to use all the possible data by this o'scope, we set the sampling frequency to 4GHz. Based on Nyquist theorem, the sampling rate should be at least twice the maximum frequency in the system. The process of data acquiry is automated using MATLAB. We capture 1000 sets of 200ns long data points. The data should not be averaged, because the data is formed as a summation of a noise signal and all delayed versions of it ($< F(x) + F(x - \tau) + \cdots >= 0$).

Oscilloscope captures only the real part of the signal. In order to recover the imaginary (phase) part of the data from the real part, we use the Hilbert transform. Hilbert transform of a function $f(x)$ is given by equation 2.13.

$$H(f)(x) = p.v. \int \frac{f(t)}{\pi(x-t)} dt, \tag{2.13}$$

where $H(f)(x)$ is the Hilbert transform of $f(x)$. The result of this transform is an analytic signal. An analytic signal has no negative frequency components. The Hilbert transform generates a complex data with the same real part as the original signal. The imaginary part has 90° phase shift compared to the real part.

The autocorrelation of the Hilbert transform of the signal is calculated for each set of data separately. The autocorrelation of the measured data is calculated by averaging out all the autocorrelation responses. The sensitivity of this technique is as calculated in (22) and is equal to $1/\sqrt{BT}$, where B is the bandwidth of the system and T is the integration time. The result of this measurement is shown in Fig. 2.31.

The zero lag peak is the dominant peak. The first delayed peak is the desired peak. The peak at 18ns is due to mismatch between the cable and the oscilloscope. The returned signal oscillates between the digitized oscilloscope and the microwave circuit.

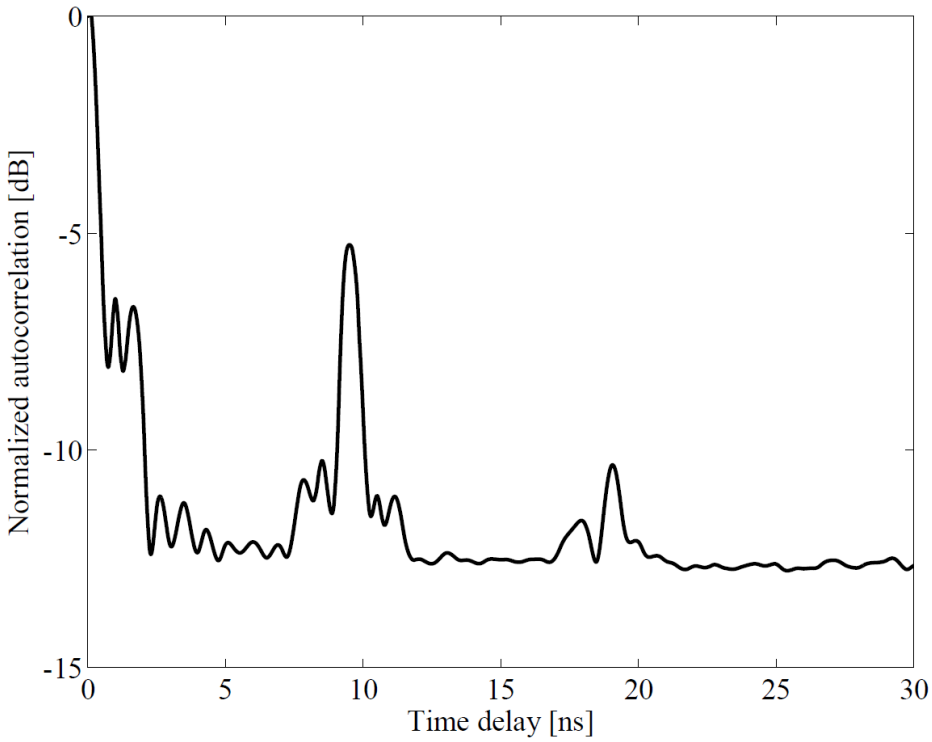

Figure 2.31: The autocorrelation response of the microwave circuit model in time domain for 9ns total delay line.

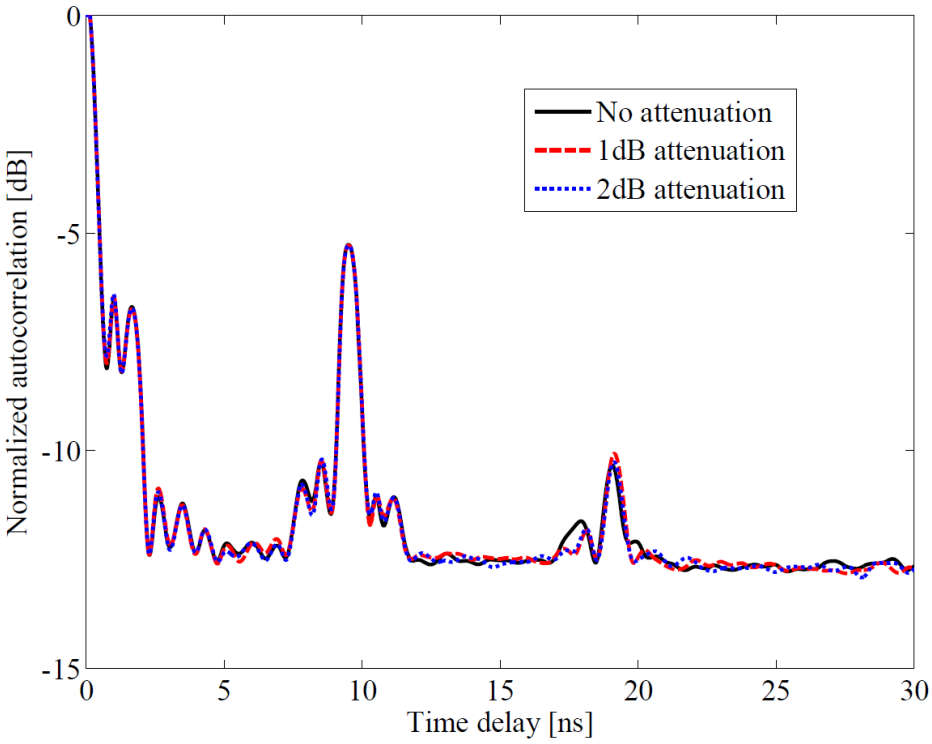

Figure 2.32: The autocorrelation response of the microwave circuit model in time domain for 9ns total delay line without attenuator (black solid line) and with 1dB (dashed red line) and 2dB (dotted blue line) attenuator.

In order to reduce this peak, an attenuator is added to the digitized oscilloscope port. The signal passes through the attenuator twice and is attenuated. The result of this modification is shown in Fig. 2.32. The peak goes down as expected. The detected signal has zero mean. In case the mean value is nonzero, the post processing stage makes the mean value zero by reducing the mean value from the detected signal. This step can also be implemented in the hardware by adding a dc block stage.

A bilayer media can be modeled by adding another loop to the microwave circuit model as shown in Fig. 2.33. This idea can be repeated to model the wave propagation inside any low loss multilayer media. The comparison between the autocorrelation response of the measured signals for one layer and bilayer structures is shown in Fig. 2.34. The circuit consists of a 3ns delay loop and a 9ns delay loop. The delayed peaks at 3ns and 9ns are the first order delays. The 3ns peak is within the sidelobe

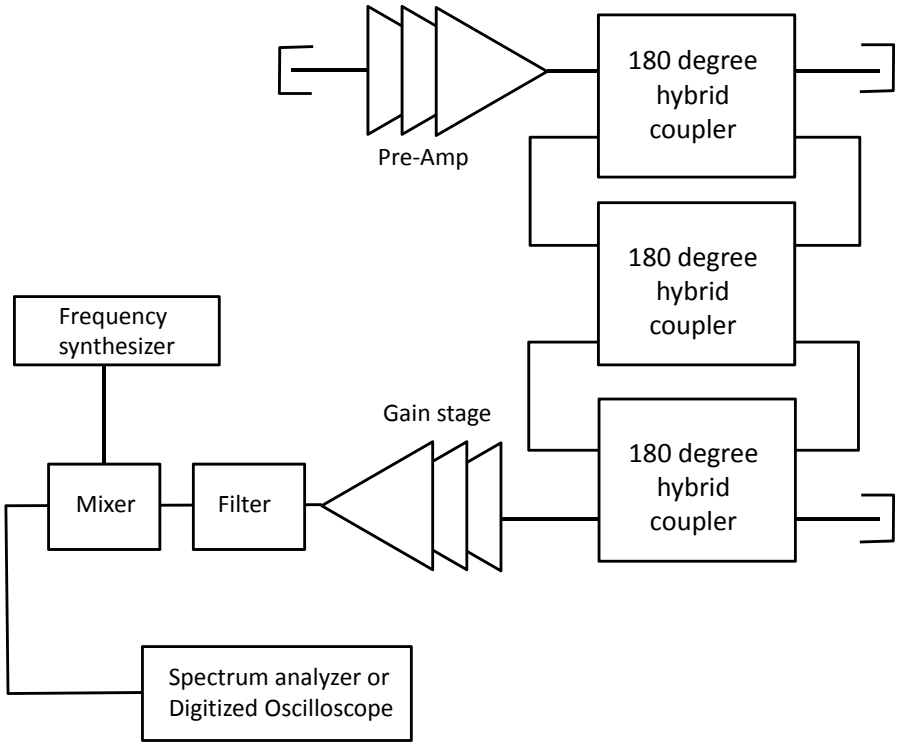

Figure 2.33: The microwave circuit schematics that models the signal propagation inside a bilayer media.

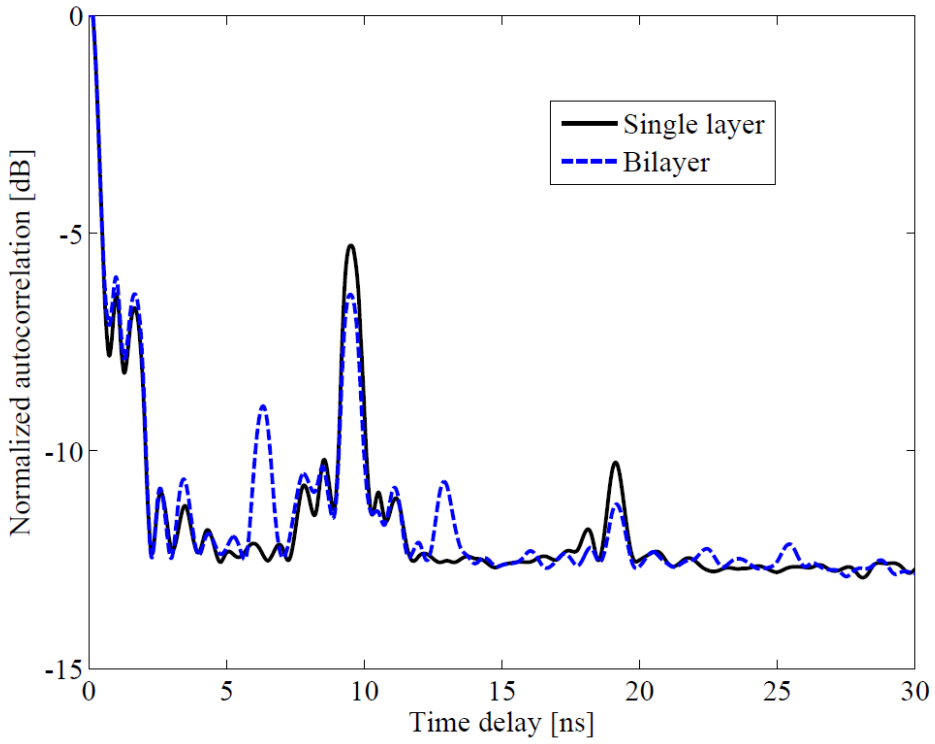

Figure 2.34: The autocorrelation response of the microwave circuit model for monolayer (black solid line) and bilayer (dashed blue line) using the time domain implementation.

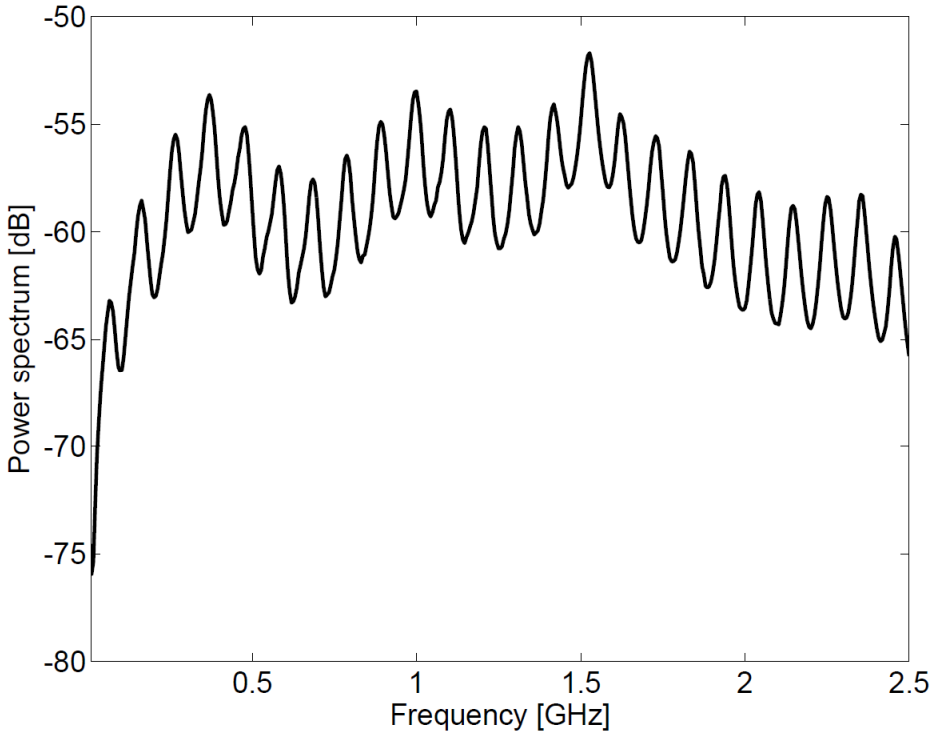

Figure 2.35: The power spectrum of the microwave circuit model of one layer medium. The ripples are easily detectable in the power spectrum.

of the zero lag peak. The peak at 6ns corresponds to the second order peak at 3ns and also the difference between the 9ns and 3ns peaks. The peak at 12ns is because of constructive interference in both layers adding up to $9 + 3 = 12$ns. For comparing the time and frequency domain implementation, we have replaced the digitized oscilloscope with a spectrum analyzer. The same loop structures as used in the time domain measurement are monitored and analyzed. The power spectrum for a single loop microwave circuit is shown in Fig. 2.35. The ripples verify the correct measurement. The autocorrelation response as a function of time delay for a one loop microwave circuit with a 2dB attenuator both in the time and frequency domains is shown in Fig. 2.36. The sensitivity of the time domain is less than the frequency domain. We try to make the sensitivity of both implementation as close as possible. However, due to the limitation at the maximum resolution bandwidth, the sensitivity of two systems are different. The autocorrelation response as a function of time delay

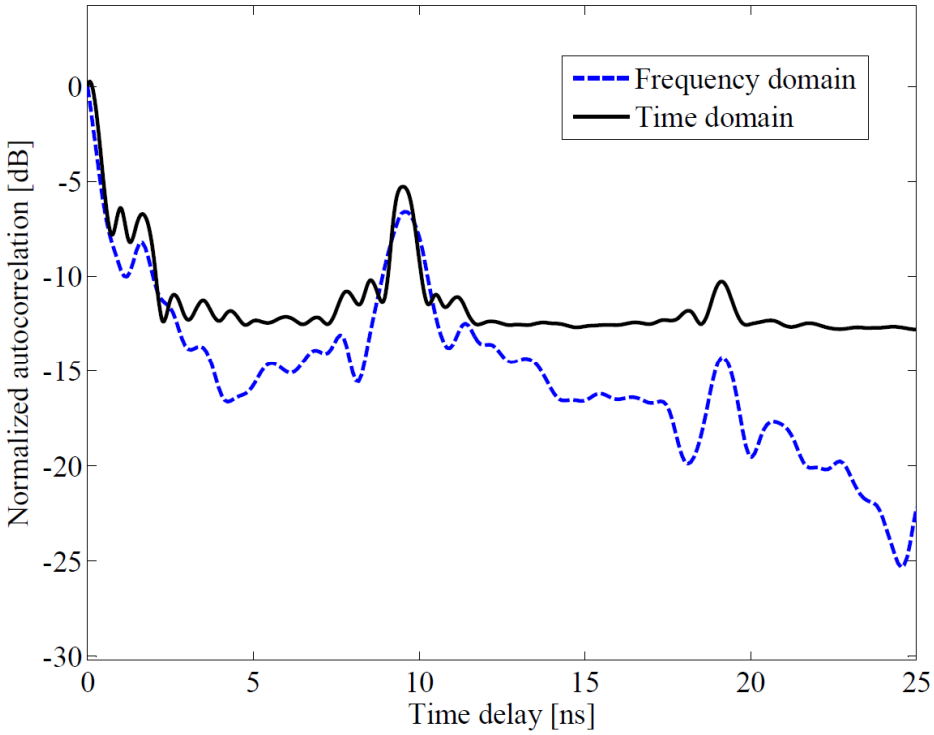

Figure 2.36: The autocorrelation response of the microwave circuit model with a single loop as a function of time delay for both the time domain measurement (black solid line) and frequency domain measurement (dashed blue line).

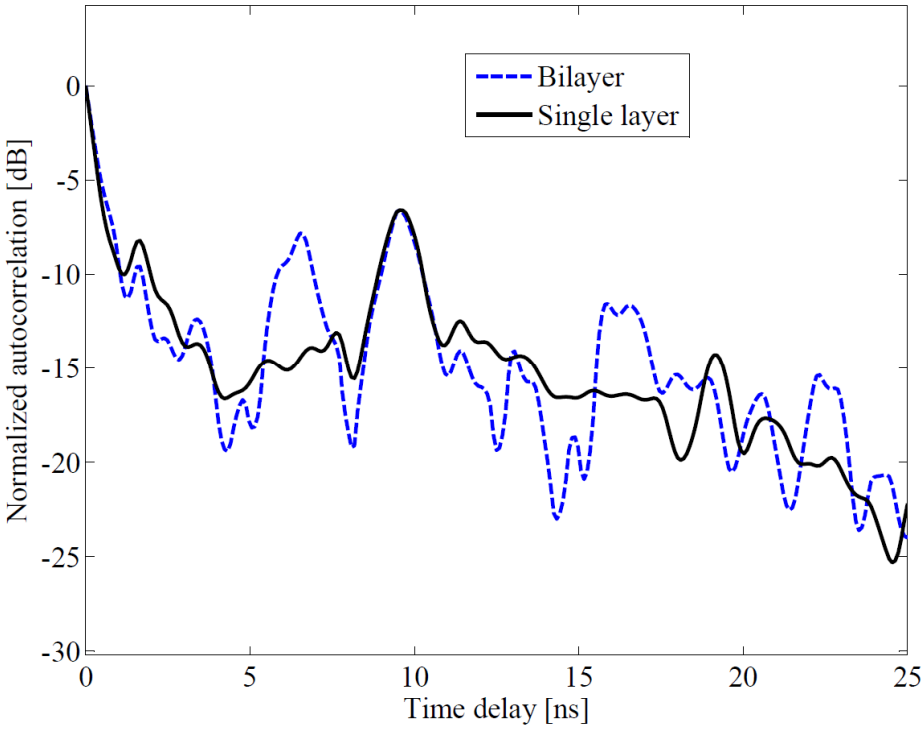

Figure 2.37: The autocorrelation response of the microwave circuit model for monolayer (black solid line) and bilayer (dashed blue line) using the frequency domain implementation.

for both monolayer and bilayer media are shown in Fig. 2.37. The same conclusion as the time domain data can be inferred from the figure. The peak at 3ns is also detectable in this implementation. The sidelobes are much smaller than the time domain counterpart. Therefore, the minimum detectable thickness is smaller.

2.4 Sensitivity Analysis

2.4.0.1 Radiometer

The system input noise temperature (T_{SYS}) is the summation of the noise temperature of the receiver plus the contribution of the antenna. T_{SYS} can be formulated as in (2.14).

$$T_{SYS} = \eta T_A + (1-\eta)T_p + FT_0, \tag{2.14}$$

where T_A is the scene temperature. η is the efficiency of the antenna. T_p is the antenna physical temperature, and F is the overall receiver noise factor. The third term in the right hand side of (2.14) is also known as T_{rec}. The sensitivity can be formulated as $\frac{\Delta T}{T_{SYS}}$, where ΔT is the minimum detectable temperature using WiBAR.

2.4.0.2 Spectrum Analyzer

Spectrum analyzer is an instrument that is capable of measuring the power spectral density as a function of frequency. The received signal passes through an internal tunable super-heterodyne receiver, in which the intermediate frequency (IF) filter is swept through the overall bandwidth. This filter is also known as resolution bandwidth filter. The filtered signal then enters a square-law detector. The detected power is averaged out to diminish the noise level using a low pass filter also known as video bandwidth filter. The ratio of the resolution bandwidth to the video bandwidth

determines the noise floor in the measurement (10).

A spectrum analyzer operates as the processing unit in our implemented WiBAR. Using the Wiener Khinchin theorem, the inverse Fourier transform of the power spectral density (Spectrum analyzer display) is equal to the autocorrelation response applied to the received data. By applying an external inverse Fourier transform to the spectrum analyzer data, the autocorrelation pattern can be estimated. The ripples in the frequency spectrum are transformed to the peaks in autocorrelation domain.

In a spectrum analyzer, there are several parameters that should be tuned prior to operation for maximum achievable sensitivity, resolution, and data collection time. These parameters are listed as frequency span (F_s), sweep time (T_s), resolution bandwidth (B_r), and video bandwidth (B_v).

We start by choosing resolution bandwidth. Two signals that are separated by $\Delta f[Hz]$ and the amplitude difference of $\Delta A[dB]$ can be distinguished on spectrum analyzer if the resolution bandwidth is chosen as in (2.15).

$$\begin{aligned} \Delta A &= -3-(60-3)\frac{\Delta f - B_{r3dB}/2}{B_{r60dB}/2 - B_{r3dB}/2} \\ B_r &= \frac{-114\Delta f}{10(3+\Delta A)-57}. \end{aligned} \tag{2.15}$$

B_{rndB} is the resolution bandwidth measured at ndB bandwidth. The default value for B_r is measured at $3dB$ bandwidth. Equation (2.15) is obtained by the resolution bandwidth filter characteristics, which is a bandpass filter. In case that the spectrum analyzer is using digital filters, the number 10 in the denominator should be changed to 4. Using this formula and the periodicity of the ripples, we can find an optimum value for the resolution bandwidth. In case of thin ice, the resolution bandwidth can be set to $3MHz$ easily. In case of very thick ice without thickness variation and trapped air bubbles (the ideal case), the resolution bandpass filter will provide a margin of $4dB$ for the adjacent ripples to be detected using the same resolution

bandwidth of $3MHz$. In case of a very thick layer, we should use a smaller resolution bandwidth such as $1MHz$ for capturing the ripples.

In spectrum analyzer, the sweep time (T_s) can be calculated using the resolution bandwidth (B_r), video bandwidth (B_v), and frequency span (F_s) as given by (2.16). The sweep time is a time required for a full sweep of the frequency span and can be translated as the waiting time for each measurement.

$$T_s = 2.694 \frac{F_s}{B_r.B_v}. \tag{2.16}$$

Equation (2.16) is valid when $B_v < B_r$, which is the case in our measurements. The constant number in front of the fraction in (2.16) depends on the type of spectrum analyzer and is around 2.5 for different types of spectrum analyzer. In our setup, we have chosen $B_v = 300Hz$, $B_r = 3MHz$, $F_s = 3GHz$. The required sweep time was almost $9s$, which is in agreement with this formula. We do have some flexibility in reducing the frequency span but in order to get higher accuracy in the autocorrelation peak and its spread, we aim for maximum available span. The maximum span is equal to $3GHz$ in our measurement setup. The smallest suggested frequency span should cover at least 2 periods of the ripples. In case of very thin ice, this interval should be larger due to the relatively longer period of the ripples. The number of periods in the overall bandwidth (m) directly maps to the number of the frequency bin ($m + 1$), in which the autocorrelation peak occurs. Due to strong self correlation, this minimum number should be at least two or more.

The noise level in radiometers can be calculated using (2.17) (78).

$$\frac{\Delta T}{T_{SYS}} = \frac{1}{\sqrt{B\tau\prime}}, \tag{2.17}$$

where B is the radiometer bandwidth and $\tau\prime$ is the integration time. In WiBAR,

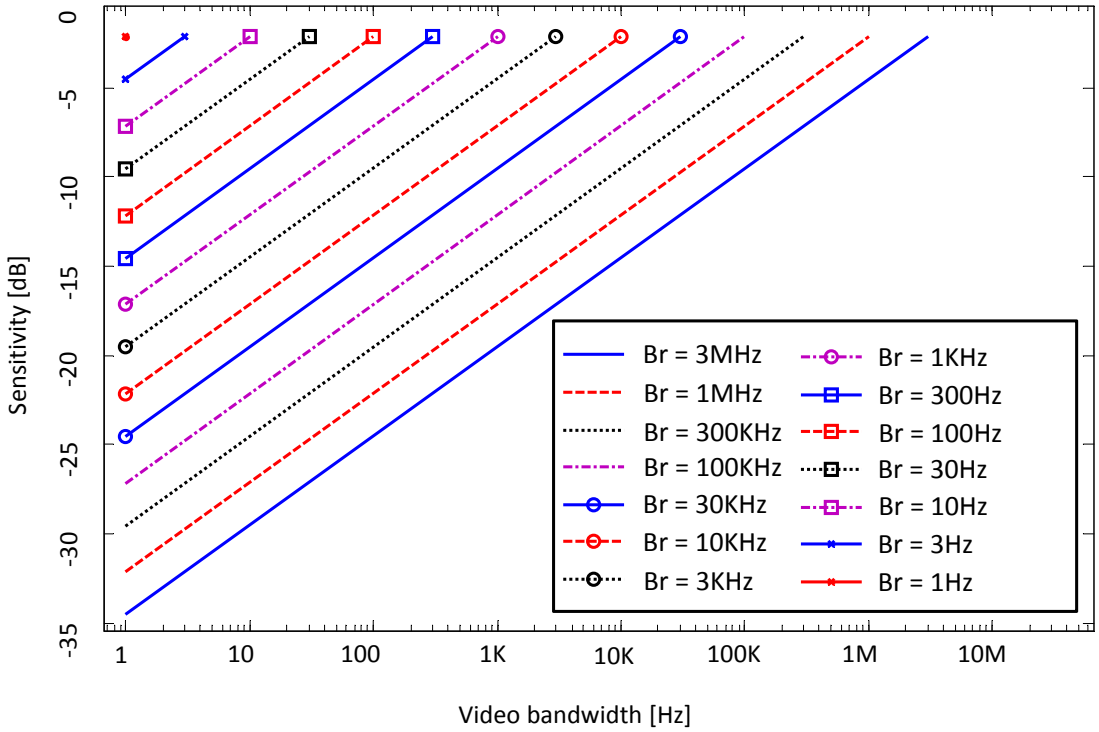

Figure 2.38: Variation of the $NE\Delta T$ as a function of video bandwidth for several values of resolution bandwidths.

B should be substituted by resolution bandwidth and τ by the time that the spectrum analyzer spends in each resolution element. Therefore, $\tau\prime = \frac{B_r}{df/dt} = \frac{B_r}{F_s/T_s}$. By substituting for T_s from (2.16) in τ, the noise level can be calculated as in (2.18).

$$\frac{\Delta P}{P} = \frac{\Delta T}{T_{SYS}} = \frac{1}{\sqrt{2.694\frac{B_r}{B_v}}}, \tag{2.18}$$

where P is the noise power and can be substituted by $kT_{SYS}B$. Equation (2.18) is the well known equation for the noise-equivalent uncertainty in brightness temperature, aka $NE\Delta T$ of a radiometer. Equation (2.18) can be used to set the video bandwidth based on the required sensitivity. It also suggests that by reducing video bandwidth and increasing resolution bandwidth, the maximum sensitivity can be achieved.

Equation (2.15) can easily be satisfied even with the maximum value of resolution bandwidth, which is $3MHz$. The $NE\Delta T$ can be plotted as a function of video

bandwidth for a range of possible resolution bandwidths as shown in Fig. 2.38. The possible resolution bandwidths for a commercial off-the-shelf (COTS) spectrum analyzer can be formulated as $a \times 10^b Hz$, where $a \in \{1, 3\}$ and $b \in \{0, 1, 2, 3, 4, 5, 6\}$. The minimum required sensitivity can be calculated by considering the reflection of the brightness temperature at the top and bottom of the layer, the volumetric scattering inside the layer, and the surface scattering due to the roughness of the top and bottom interfaces. The volumetric scattering ranges from 2 to 8 dB/m depends on the volume fraction of air bubbles captured in the lake ice layer (*Vickers*; 39). The surface scattering from the top and bottom of the lake ice is within $2dB$ (31). $NE\Delta T$ of less than $-20dB$ is desirable, which can be achieved by setting the resolution bandwidth to $3MHz$ and the video bandwidth to $300Hz$. In the case of an airborne/spaceborne setup, the overall time of data collection is limited. Therefore, the design should aim for high sensitivity considering minimum achievable sweep time.

The optimum value for the video bandwidth and resolution bandwidth have been calculated using an optimization procedure. The constraint is sensitivity of less than $-20dB$ and the goal function is the sweep time. The optimum values for $F_s = 3GHz$ are listed in Table 2.1. The best choice is for $B_r = 3MHz$ and $B_v = 300Hz$.

Table 2.1: Minimum sweep time for optimum video and resolution band widths

parameter	Optimum values			
Video bandwidth [Hz]	300	100	100	30
Resolution bandwidth [MHz]	3	3	1	3
Sweep time [s]	8.96	26.9	80.7	89.6
Sensitivity [dB]	-22.15	-24.54	-22.15	-27.15

2.5 Theoretical investigation of the autocorrelation response

We previously calculate the emission of a half-space dielectric medium beneath a dielectric slab as given by equation 2.11. The probability distribution of the brightness temperature is Gaussian. The detected power by the radiometer (P_{REC}) should have

the closed form given by equation 2.19.

$$P_{REC} = \frac{(1-|r_1|^2)(1-|r_2|^2)\overline{P}G(\omega)}{1+|r_1|^2|r_2|^2+2|r_1||r_2|cos(\omega\tau)}, \tag{2.19}$$

where $\overline{P}$ is the average background emission power, $G(\omega)$ is the gain of the WiBAR as a function of angular frequency. In the first part of our analysis, where the grazing angle is unique, without loss of generality, we assume a flat top shape for the WiBAR gain. By assuming the real and imaginary part of $V(x)$, emission voltage detected by antenna in radiometer, has Gaussian distributions, the power will be in the form of Chi-squared distribution. The ratio of the optimum resolution bandwidth to video bandwidth of spectrum analyzer ($3MHz/300 = 10,000$) is the number of repetition in detecting power spectrum. Using this number of repetition and averaging, the Chi-squared distribution (also known as Erlang distribution) approaches to a Gaussian distribution (using central limit theorem) with different mean value and variation. The mean value of the averaged result can be calculated as given by equation 2.20.

$$\begin{aligned} X_i &\backsim Exponentialdistribution(\lambda) \\ \Sigma_{i=1}^{k} X_i &\backsim Erlang(k, k\lambda), \end{aligned} \tag{2.20}$$

where λ is the number of square Gaussian distributions involved in the power and in our case is equal to 2. $k = RBW/VBW$,where RBW is the resolution bandwidth and VBW is the video bandwidth. The mean value and variance of the Erlang distribution of $Erlang(k, \lambda)$ is equal to k/λ and k/λ^2, respectively.

In our case, the mean value and variance of $Erlang(k, k\lambda)$ are equal to $\mu = k/k\lambda = 1/\lambda$ and $\sigma^2 = k/(k\lambda)^2 = 1/(k\lambda^2)$, respectively. In spectrum analyzer, resolution bandwidth is a tunable bandpass filter swept over the bandwidth of the radiometer. Therefore, the distribution of the received stationary process in each resolution bandwidth is uncorrelated and independent from other received process at other resolution

bandwidth. We can assume that the probability distribution of the received random process in each resolution bandwidth is $\overline{P_j}$. Therefore, the joint pdf (probability density function) is a Gaussian distribution (using central limit theorem) indicated by $P(\overline{P_1}, \overline{P_2}, ..., \overline{P_N})$, where $N = (f_{max} - f_{min})/RBW$. f_{min} and f_{max} are the minimum and maximum detectable frequencies by WiBAR. We also can further simplify the joint pdf by considering the independence of the processes and the simplified formulation is $P(\overline{P_1}, \overline{P_2}, ..., \overline{P_N}) = \overline{P_1} \times \overline{P_2} \times ... \times \overline{P_N}$. The mean values and variances of all of them are the same and ripples, is are given by equation 2.21.

$$\begin{aligned} p(x) &= Erlang(k, k\lambda) = \frac{(k\lambda)^k x^{k-1} e^{-k\lambda x}}{(k-1)!} \; x \geq 0 \\ \mu_E &= \int x p(x) dx = \frac{(k\lambda)^k}{(k-1)!} \int \frac{x^k}{e^{k\lambda x}} \\ \mu_E &= \frac{(k\lambda)^k \Gamma(k+1)}{(k-1)!(k\lambda)^{k+1}} = \frac{1}{\lambda} \\ \mu_E^2 + \sigma_E^2 &= \int x^2 p(x) dx = \frac{(k\lambda)^k}{(k-1)!} \int \frac{x^{k+1}}{e^{k\lambda x}} \\ \mu_E^2 + \sigma_E^2 &= \frac{(k\lambda)^k \Gamma(k+2)}{(k-1)!(k\lambda)^{k+2}} = \frac{k+1}{k\lambda^2}, \end{aligned} \tag{2.21}$$

where $\Gamma(x)$ is the Gamma function and for integer x is equal to $(x-1)!$.

In the following subsections, our goal is to find the expected value and variance of the autocorrelation function.

2.5.1 Expected value calculation

Expected value of the autocorrelation response ($E(R(\tau, \overline{P}))$) can be formulated as given by equation 2.22 using Weiner-Khinchin theorem.

$$\begin{aligned} R(\tau\prime, x) &= \int P_{REC} e^{-2i\pi f\tau\prime} df \\ E(R(\tau, \overline{P})) &= \int\int \cdots \int P_{REC} e^{-2i\pi f\tau\prime} P(\overline{P_1}, \overline{P_2}, ..., \overline{P_N}) df d\overline{P_1} \cdots d\overline{P_N} \\ &= \Sigma_{j=1}^{N} \left(\int_{f_{min}+(j-1)RBW}^{f_{min}+jRBW} \frac{C_P e^{-2i\pi f\tau\prime} df}{1 + |r_1|^2|r_2|^2 + 2|r_1||r_2|cos(\omega\tau)} \right) I_j, \end{aligned} \quad (2.22)$$

where $C_P = (1 - |r_1|^2)(1 - |r_2|^2)\overline{P}G(\omega)$ and $I_j = \int \overline{P_j} P(\overline{P_j}) d\overline{P_j} = \mu_E$. The problem is reduced to find a closed form for the Σ term. The integrand is independent of j and only the limits of the integral are depending on j. Therefore, we can combine all the terms and calculate a single integral given by equation 2.23.

$$E(R(\tau, \overline{P})) = \mu_E \int_{f_{min}}^{f_{max}} \frac{cos(2\pi f\tau\prime) + isin(2\pi f\tau\prime)}{1 + |r_1|^2|r_2|^2 + 2|r_1||r_2|cos(2\pi f\tau)} df \quad (2.23)$$

, where we define $a = 2\pi\tau\prime, b = 2\pi\tau$, and $\beta = |r_1||r_2|$. $P(\overline{P_j}) = \frac{1}{\sigma\sqrt{2\pi}} e^{\frac{(\overline{P_j}-\mu)^2}{2\sigma^2}}$ is the probability density function (pdf) of the averaged power.

The integral (I) has been solved in closed form in two different approaches. In the first approach, by considering the typical values for the reflection for ice and snow layers, the denominator is very close to one and can be approximated by its Taylor expansion around one. Based on reflection coefficients values the first order term is only used for snow layers and the first and second order terms are used for the ice layers. The integral can be solved as given by equation 2.24. The integral limits are

the lower and upper $3dB$ bandwidth of the WiBAR.

$$
\begin{aligned}
I &= \int \frac{cos(af)+isin(af)}{1+\beta^2+2\beta cos(bf)}df = \int \frac{cos(af)+isin(af)}{(1+\beta^2)(1+\frac{2\beta}{1+\beta^2}cos(bf))}df \\
I &= \int \frac{cos(af)+isin(af)}{1+\beta^2}(1-\frac{2\beta}{1+\beta^2}cos(bf)+\left(\frac{2\beta}{1+\beta^2}cos(bf)\right)^2)df \\
I &= \kappa(f_{max})-\kappa(f_{min}) \\
\kappa(f) &= \frac{sin(af)-icos(af)}{a(1+\beta^2)}+\frac{2\beta}{(1+\beta^2)^2(a^2-b^2)}\times \\
&\times \ (ibsin(af)sin(bf)+iacos(af)cos(bf)-acos(bf)sin(af)+bcos(af)sin(bf))+ \\
&+ \ 4\beta^2\frac{2b^2sin(af)-a^2cos^2(bf)sin(af)+2abcos(af)cos(bf)sin(bf)}{a(4b^2-a^2)(1+\beta^2)^3}+ \\
&+ \ 4\beta^2\frac{ia^2cos(af)cos^2(bf)-2ib^2cos(af)+2iabcos(bf)cos(af)sin(af)}{a(4b^2-a^2)(1+\beta^2)^3},
\end{aligned}
\tag{2.24}
$$

the second approach is given by equation set 2.25.

$$
\begin{aligned}
I &= \int_{f_c-\frac{B}{2}}^{f_c+\frac{B}{2}} \frac{e^{iaf}}{1+\beta^2+\beta(e^{ibf}+e^{-ibf})}df \\
I &= \int_{f_c-\frac{B}{2}}^{f_c+\frac{B}{2}} \frac{e^{iaf}}{1+\beta^2}\left(1-\frac{\beta(e^{ibf}+e^{-ibf})}{1+\beta^2}+\frac{\beta^2(e^{ibf}+e^{(}-ibf))^2}{(1+\beta^2)^2}\right)df \\
I &= \Delta(f_c+\frac{B}{2})-\Delta(f_c-\frac{B}{2}) \\
\Delta(f) &= \frac{1}{1+\beta^2}\left(\frac{e^{iaf}}{ia}-\frac{\beta}{1+\beta^2}(\frac{e^{i(a+b)f}}{i(a+b)}+\frac{e^{i(a-b)f}}{i(a-b)})\right)+ \\
&+ \ \frac{\beta^2}{(1+\beta^2)^3}\left(\frac{e^{i(a+2b)f}}{i(a+2b)}+\frac{e^{i(a-2b)f}}{i(a-2b)}+\frac{2e^{iaf}}{ia}\right)
\end{aligned}
\tag{2.25}
$$

From the solution of these integrals, it is obvious that the maxima of the expected value of autocorrelation response are at the specific values of $b = a$ and $b = a/2$, representing the $\tau\prime = \tau$ and $\tau\prime = 2\tau$. In these specific values, the denominator goes to zero, represents a peak in the autocorrelation response. We have assumed a flat top shape for the gain of the radiometer, therefore, the expected value has a Sinc

function with the peak to peak distance equal to $1/B$. a Sinc function is defined as $sinc(x) = sin(x)/x$.

A slightly better analysis, assume a Gaussian shape for the passband of the resolution bandwidth filter inside the spectrum analyzer with $2\sigma = RBW$ and $f_c\prime = f_{min} + (j + 1/2)RBW$. The formulation can be simplified as given by equation 2.26.

$$\begin{aligned} E(R(\tau\prime)) &= \mu \sum_{j=1}^{N} \frac{e^{-\frac{f_c^2\prime}{2\delta^2}}}{(1+\beta^2)\sqrt{2\pi\delta^2}} \left(L\left[f_{min} + (j-1)\,RBW\right] - L\left[f_{min} + jRBW\right]\right) \\ L\left[f\right] &= \left(1 + \frac{2\beta^2}{(1+\beta^2)^2}\right) G\left(a, f\right) - \frac{\beta}{1+\beta^2}\left(G\left(a+b, f\right) + G\left(a-b, f\right)\right) + \\ &+ \frac{\beta^2}{(1+\beta^2)^2}\left(G\left(a+2b, f\right) + G\left(a-2b, f\right)\right) \\ G(a, f) &= \sqrt{\pi}\frac{\delta}{\sqrt{2}} e^{\frac{\delta^2}{2}\left[ia + \frac{f_c'}{\delta^2}\right]^2} \left[1 - \Phi\left(\frac{\left(-\frac{f_c'}{\delta^2} - ia\right)\delta}{\sqrt{2}} + \frac{f}{\delta\sqrt{2}}\right)\right], \end{aligned} \tag{2.26}$$

where $\Phi(.)$ is the complex error function.

For the purpose of completion, the same technique has been applied to the low-order microwave model. We assume that the input voltage has Gaussian distribution. The detected power can be formulated as given by equation 2.27.

$$P_o(t) = \frac{G}{2}(P(t)L_1L_2 + P(t-\tau)L_1\prime L_2\prime), \tag{2.27}$$

where G is the gain of the amplifier chain, L_1 and L_2 are the attenuation caused by the attenuators and the cable loss and τ is the time delay because of the extra length in one of the branches compared to the other one. $P(t)$ is the input power of the noise source.

The expected value of the autocorrelation response is given by equation 2.28.

$$
\begin{aligned}
P_{REC} &= (L_1L_2 + L_1'L_2'e^{i\omega\tau})P(P_1, P_2, \cdots, P_N)G' \\
E(R(\tau\prime, x)) &= E(\int P_{REC}e^{-i2\pi f\tau'}df) \\
E(R(\tau\prime, x)) &= \mu\sum_{j=1}^{N}\int_{f_{min}+(j-1)RBW}^{f_{min}+jRBW}\left(L_1L_2 + \frac{L_1'L_2'e^{i2\pi f\tau}}{2}\right)e^{-2i\pi f\tau'}df) \\
E(R(\tau\prime, x)) &= \frac{\mu}{\pi}(\frac{L_1L_2e^{-2i\pi f_c\tau'}sin(\pi B\tau')}{\tau'} + \frac{L_1'L_2'e^{2i\pi f_c(\tau-\tau')}sin(\pi B(\tau'-\tau))}{2(\tau-\tau')}) \\
&, \qquad (2.28)
\end{aligned}
$$

In the low order model, only the first order delay is presented. The peaks are at zero lag ($\tau' = 0$) and at $\tau' = \tau$.

Using the Gaussian bandwidth for the resolution bandwidth filter in the spectrum analyzer, the expected value of the autocorrelation response is given by equation 2.29.

$$
\begin{aligned}
E[R(\tau')] &= \sum_{j=1}^{N}\frac{\mu e^{-\frac{f_{cj}^2}{\sigma^2}}}{\sqrt{2\pi\sigma^2}}(L_{mw}[f_{min} + (j-1)RBW] - L_{mw}[f_{min} + jRBW]) \\
Lmw[f] &= L_1L_2G[-2\pi\tau', f] + \frac{L_1'L_2'}{2}G[-2\pi(\tau'-\tau)], \qquad (2.29)
\end{aligned}
$$

2.5.2 Standard deviation calculation

The variance of $R(\tau')$ is formulates as $Var[R] = E[(R - E[R])(R - E[R])^*]$, where $*$ denotes the complex conjugation operator. For simplicity the variables are omitted in the above formulation. We also know that $\left(\int F(f)df\right)^* = \int F^*(f)df$, because the frequency is a real variable and we also know that P is a real value parameter, therefore, the complex conjugate operator can be removed from the expectation value argument and we have $E[R^*] = E^*[R]$. The variance of the autocorrelation response is given by equation 2.30.

$$
\begin{aligned}
Var[R] &= E[RR^*] - E[R]E[R^*] - E^*[R]E[R] + E[R]E^*[R] \\
Var[R] &= E[RR^*] - E[R]E[R^*] = E[RR^*] - |E[R]|^2 \\
E[RR^*] &= \int\int\cdots\int[\int P_{REC}e^{-2i\pi f\tau'}df \times \int P^*_{REC}e^{2i\pi f'\tau'}df']PdP, \quad (2.30)
\end{aligned}
$$

where P is $P(\overline{P_1},\cdots,\overline{P_N})$ and $dP = d\overline{P_1}\cdots d\overline{P_N}$. By partitioning the bandwidth into several equi-distance intervals with the width equal to resolution bandwidth and write the expression in the summation form we can simplify the equation into equation given by (2.31).

$$
\begin{aligned}
E[RR^*] &= \int\cdots\int[\sum_{j=1}^{N}\overline{P_j}l_j][\sum_{k=1}^{N}\overline{P_k}l_k]^*P(\overline{P_1})\cdots P(\overline{P_N})d\overline{P_1}\cdots\overline{P_N} \\
E[RR^*] &= \int\cdots\int[\sum\sum\overline{P_jP_k}l_jl_k^*]P(\overline{P_1})\cdots P(\overline{P_N})d\overline{P_1}\cdots\overline{P_N}, \quad (2.31)
\end{aligned}
$$

where $l_j = \Delta(f_{min}+jRBW) - \Delta(f_{min}+(j-1)RBW)$. In order to simplify this equation, the following two integral solutions have been used as given by equation 2.32.

$$
\begin{aligned}
\int x_i^2P_i(x_i)dx_i &= \mu^2+\sigma^2 \\
\int\int x_ix_jP_i(x_i)P_j(x_j)dx_idx_j &= \mu^2 \quad (2.32)
\end{aligned}
$$

$$
\begin{aligned}
E[RR^*] &= \sum_{i=1}^{N} |l_i|^2(\mu^2+\sigma^2) + \sum_{i\neq j}\sum l_i l_j^* \mu^2 \\
E[R]E^*[R] &= \sum_{i=1}^{N} |l_i|^2(\mu^2) + \sum_{i\neq j}\sum l_i l_j^* \mu^2 \\
Var[R] &= \sum_{i=1}^{N} |l_i|^2\sigma^2
\end{aligned} \tag{2.33}
$$

In the microwave low order model $l_j = (L_1L_2)/(\pi\tau')e^{-2i\pi f_{cj}\tau'}sin(\pi RBW\tau')$ + $+ (L_1'L_2')/(2\pi(\tau'-\tau))e^{-2i\pi f_{cj}(\tau'-\tau)}sin(\pi RBW(\tau'-\tau))$. For Gaussian shaped resolution bandwidth filter, $l_j = \frac{e^{-\frac{-f_{cj}^2}{\sigma^2}}}{(1+\beta^2)\sqrt{2\pi\sigma^2}}(L[f_{min}+(j-1)RBW] - L[f_{min}+jRBW])$. Using Gaussian filter for RBW in the microwave low-order model we have $l_j = \frac{e^{-\frac{-f_{cj}^2}{\sigma^2}}}{\sqrt{2\pi\sigma^2}}(L_{mw}[f_{min}+(j-1)RBW] - L_{mw}[f_{min}+jRBW])$.

In the post processing of ice and snow layers, the inverse of the emission is used for better efficiency and resiliency to RFI. The expected value and standard deviation can be formulated as given by equation 2.34.

$$
\begin{aligned}
E[R(\tau')] &= \mu\sum_{k=1}^{3} f(\alpha_k;\tau_k) \\
f(\alpha;t) &= \frac{i\alpha}{\pi t}e^{i\omega_c t}sin(2\pi Bt),
\end{aligned} \tag{2.34}
$$

where $\alpha_1 = 1+|r_1|^2|r_2|^2$, $\alpha_2 = \alpha_3 = 2|r_1||r_2|$, $\tau_1 = \tau'$, $\tau_2 = \tau+\tau'$, and $\tau_3 = \tau-\tau'$. The higher order peaks are absent if we use the inverse of emissivity in the post processing technique. Standard deviation can be calculated exactly in the same way as before except for replacing the expected value with the equation 2.34.

The expected value of the autocorrelation response for 20 cm of lake ice over water is shown in Fig. 2.39. The result of expected value of the autocorrelation response

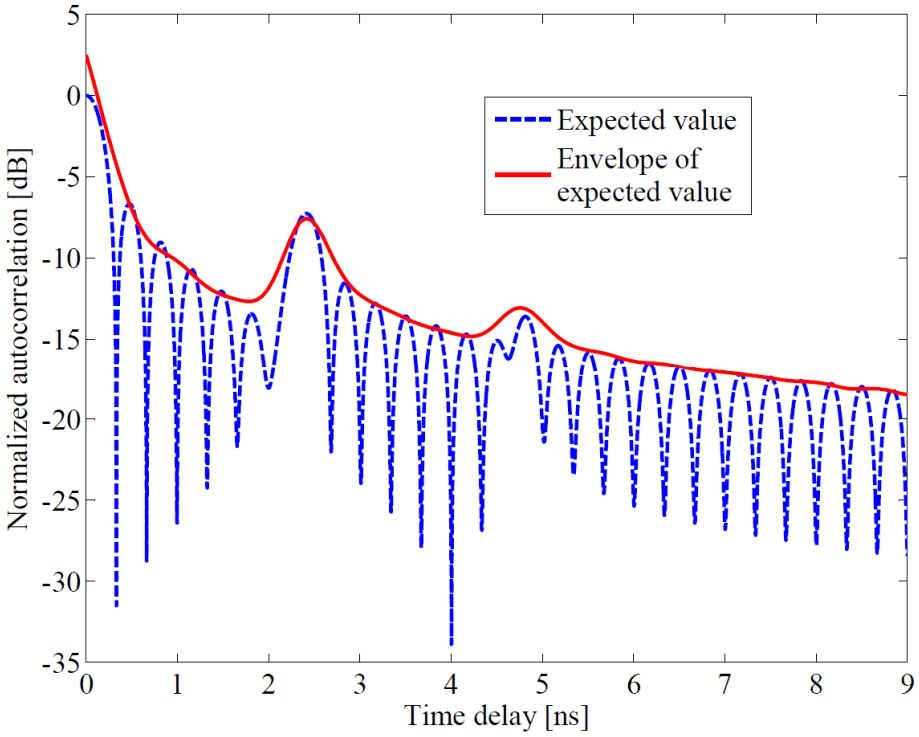

Figure 2.39: The expected value (dashed blue line) and the envelope of the expected value (solid red line) of the autocorrelation response as a function of time delay for 20cm of lake ice over water.

as a function of time delay for 40cm of snow over terrain is shown in Fig. 2.40. The effect of the bandwidth on the expected value of the autocorrelation response for 50cm of ice is shown in Fig. 2.41. The 3dB reduction in the level of signal is the effect of decreasing the bandwidth to half of its value. Standard deviation is shown in Fig. 2.42. The comparison between the model and the measurement is shown in Fig. 2.43. The modified theoretical model accounts for the system noise figure, limited frequency samples, and averaging.

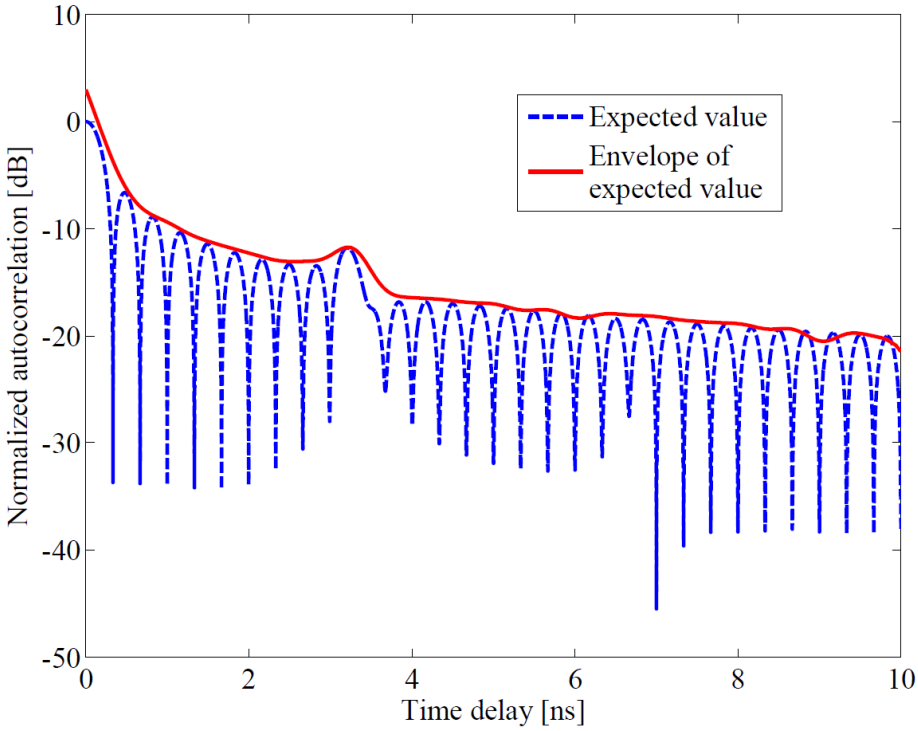

Figure 2.40: The expected value (dashed blue line) and the envelope of the expected value (solid red line) of the autocorrelation response as a function of time delay for 40cm of snow over terrain.

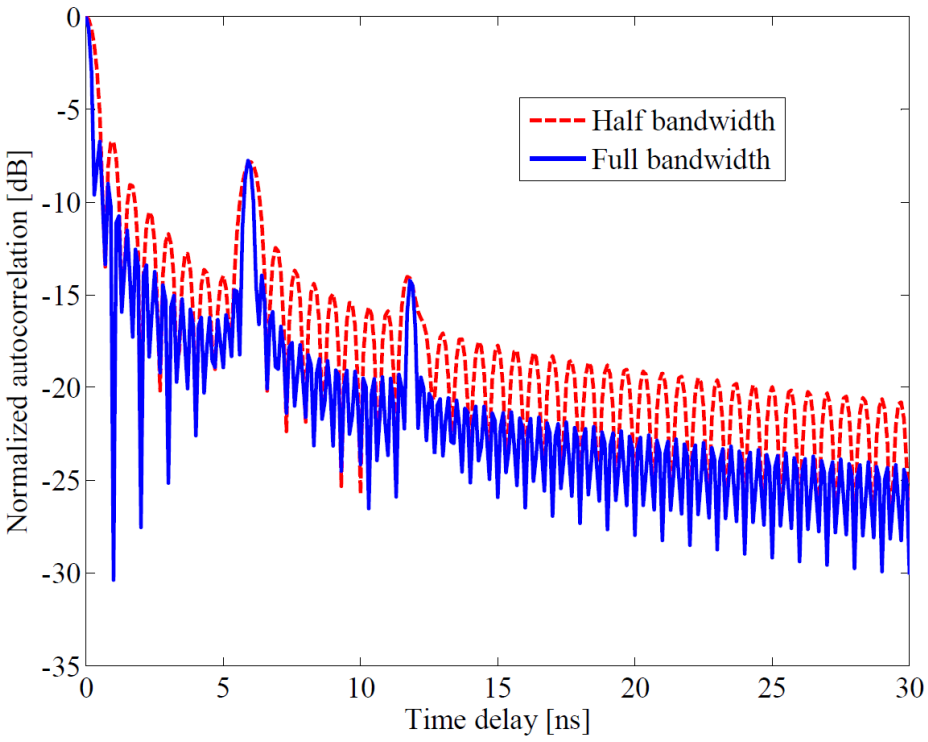

Figure 2.41: The expected value of half bandwidth (dashed red line) and full bandwidth (solid blue line) of the autocorrelation response as a function of time delay for 50cm of ice over fresh water. The Gaussian shape resolution bandwidth is used.

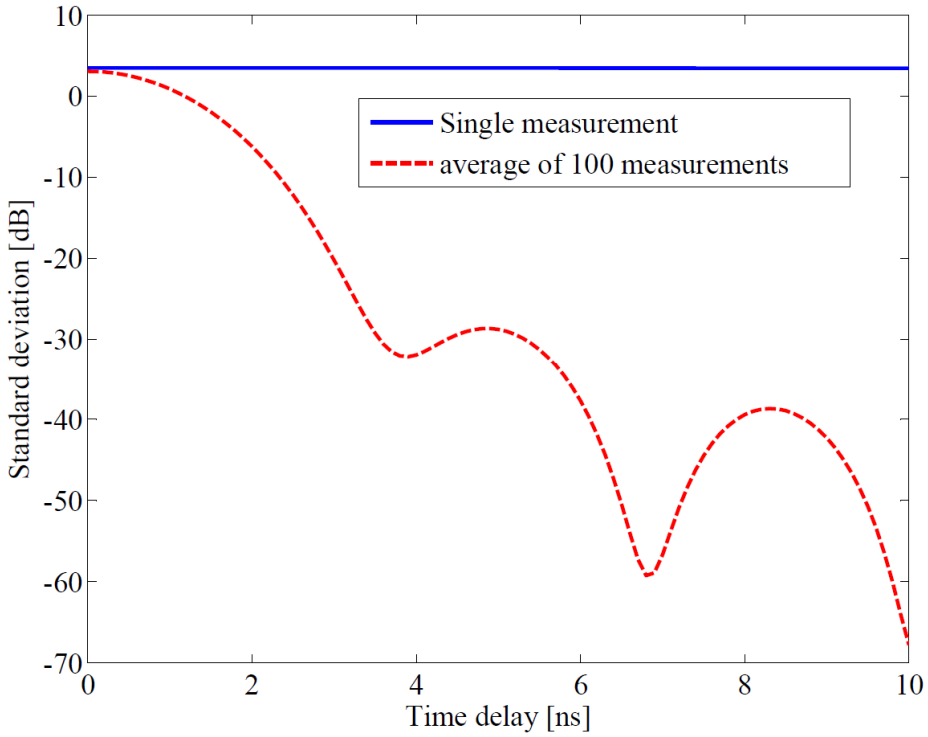

Figure 2.42: The standard deviation of the autocorrelation response of a single measurement (solid blue line) and average of 100 measurements (dashed red line) as function of time delay for 20cm of ice over fresh water. The Gaussian shape resolution bandwidth is used.

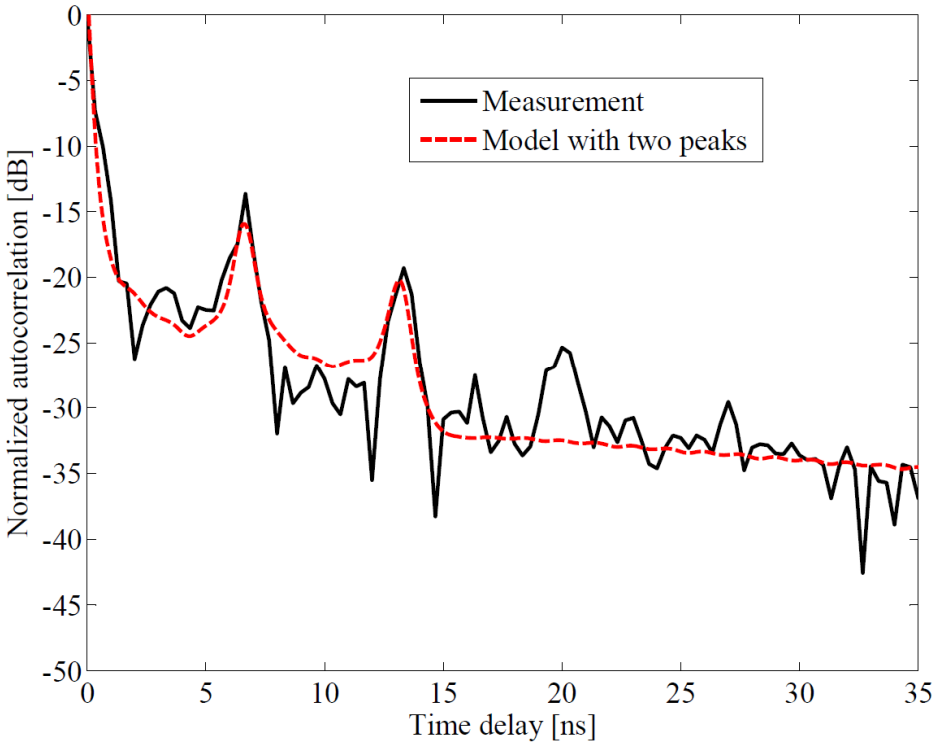

Figure 2.43: The measurement of high order microwave model (black solid line) compared with the envelope of the expected value of the theoretical model with considering two peaks only.

CHAPTER III

Design and Optimal Operation of WiBAR

3.1 Introduction

The thickness detection of low absorbing media are of interest in several applications including the snowpacks and fresh water lake ice. Snowpack is the accumulation of snow found mainly in mountainous and higher latitude regions. The importance of monitoring the snowpack thickness detection is due to its vital significance in water resource management, flood and avalanche prediction as well as ecosystem and climate studies (56; 67; 82; 45; 26). Climate change causes the non-stationary annual statistics in the snowpacks' characteristics that should be monitored in a nearly daily time intervals (50; 68; 3; 1; 2; 74; 81).

Traditionally, differential scatter darkening has been the most common technique to measure the snow water equivalence (SWE) and also the thicknesses of snowpacks (20; 21; 14; 34; 25; 62; 86; 61; 16; 27; 33; 18; 71; 41). This phenomenon is due to the volumetric scattering of the snow grains at very high frequencies. This technique relies on observing the snowpack at two different frequencies with scatter darkening stronger at the higher frequency. Using this approach an empirical formulation is usually derived to estimate the snowpack thickness. However, the empirical formula is specific to the region (61; 16; 30; 29; 49; 15). The formula, which has been used in Finland for example does not work for western Canada and vice versa (42).

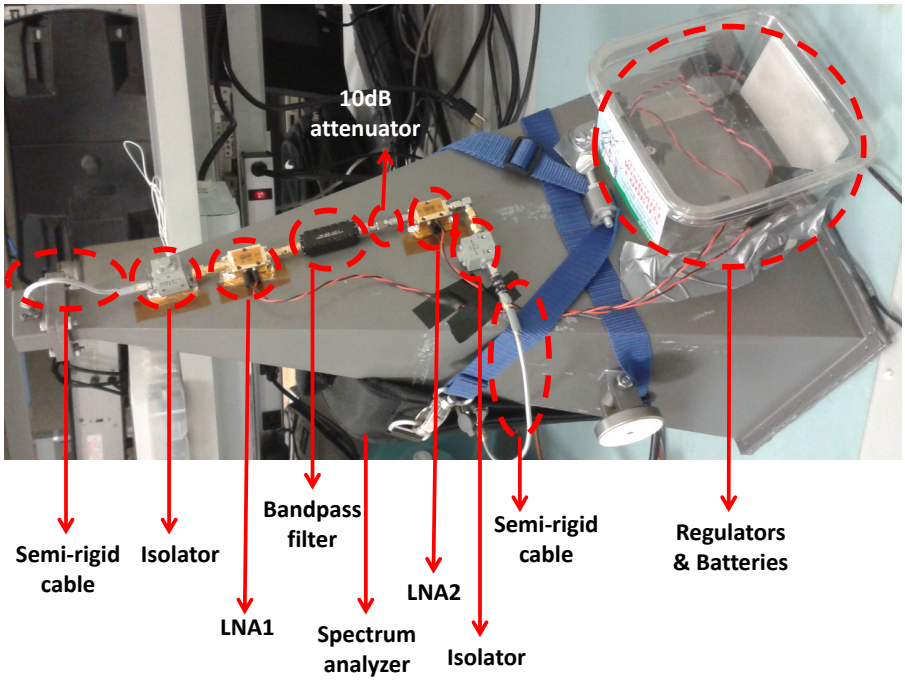

Figure 3.1: Image of the actual implementation of WiBAR.

Hence, a unique general method independent of location is highly desired.

Lake ice thickness plays an important role in the total pressure exerted to the off-shore structures (47) in winter. Estimating this pressure is a prominent factor in the design process of off-shore structures such as wind farm sites in cold regions. Ice thickness monitoring is also required in navigability of frozen inland waterways (48). The traditional way to measure the lake ice thickness is by a cumbersome *in-situ* drilling process through the ice, which is a dangerous, labor intensive task due to the risk of lake ice breaking. Therefore, the requirement for an accurate remote measurement setup, which can estimate the ice thickness without disturbing/breaking the ice is desirable.

Traditionally, radiometers are the most common instrument to sense snowpacks (46; 12). A radiometer is a passive instrument that can detect the incident brightness temperature to the aperture of the antenna. When ground/lake is covered by snow/ice, the received brightness temperature is a combination of the thermal emission of the underlying ground/lake water, the reflection of the downwelling sky brightness tem-

Figure 3.2: Block diagram of the wideband autocorrelation radiometer.

perature, and the self emission of the snowpack/lake ice. When the layer is dry, the major contribution of the detected brightness temperature is due to the thermal emission of the underlying medium, illustrated in Fig. 2.1(a) and (b). This term is composed mainly of two parts. One is due to the direct transmission of the brightness temperature and the other is the result of the doubly reflected emitted wave inside the dry snow/ice layer due to reflection at the top and bottom interfaces. The doubly reflected wave has a transit time delay compared to the direct path wave and this delay is directly proportional to the thickness of the layer. The direct and the doubly reflected background brightness temperatures are shown by arrows in Fig. 2.1 (a) and (b). The doubly reflected path experiences more attenuation due to more absorption and scattering in the snowpack/ice layer as well as reflection at the top and bottom interfaces. The attenuation of the higher order bounced back path (quadruple reflected path) is high enough that we can ignore their presence in natural scenarios including lake ice and snowpack.

A photo of our implemented wideband autocorrelation radiometer (WiBAR) is shown in Fig. 3.1. We are utilizing our radiometer for three scenarios. In the first scenario, the thickness of air gap between a thin sheet with high dielectric constant and water is detected to prove the operation of the instrument. The second scenario pertains to lake ice thickness detection, in which there is a layer of ice above water as shown in Fig. 2.1(a). The last scenario is related to snow layer thickness detection, in which a layer of snow is naturally formed over ground as shown in Fig. 2.1(b).

3.2 WideBand Autocorrelation Radiometer (WiBAR)

3.2.1 Radiometer design

We have designed, modelled, developed, and implemented three generations of WiBAR. The frequency range of operation of the first generation WiBAR is chosen to be $7-10\ GHz$. This frequency range is chosen as the size of the antenna remains small enough to implement a handheld system, while, the volumetric scattering inside each layer remains small. This frequency range also has minimum number of radio frequency interferences (RFI) (*https://science.nrao.edu/facilities/vla/observing/RFI*). The chosen frequency band is appropriate for lake ice detection or snow over flat terrain, however lower frequencies are desirable for the thickness detection of snow layer over undulating terrain. The proposed radiometer is composed of two low noise amplifiers (LNAs), a band pass filter (BPF), and hand held spectrum analyzer (S/A). The isolators and the attenuators are used for providing wideband matching among adjacent stages. The wideband impedance matching is required to remove the internal oscillation in the structure due to the instability of the LNAs. In order to stabilize the chain of high gain amplifiers and make sure that they both operate on their linear gain regime, we add an attenuator in between the amplifiers. The block diagram of the final design of the direct detection radiometer as well as a photo of final implementation are shown in Figs. 3.2 and 3.1, respectively. The overall noise figure of WiBAR is calculated using Friis formula to be $2.46dB$. The dominant contribution to the noise figure is due to the first LNA in the chain. The noise contribution of other components is negligible. Specially, the noise contribution of the BPF is much less than that of the attenuator and is neglected in the calculation of the noise figure. This calculation is formulated as given by equation (5.20) of Chapter V, Section (5.4).

The second generation of WiBAR is designed for snow characterization. Snow layers are mainly accumulated over rough surfaces or terrains. The frequency of

operation of the second generation of WiBAR is chosen to be $1-3$GHz. The larger wavelength of the second generation WiBAR, compared to the first generation, makes it an improved sensor for snow characteristics. The block diagram and photo of the second generation WiBAR are shown in Figs. 3.3 (b) and (e). We choose an antenna with wide beamwidth as the first stage of this sensor. The LNA is installed right after antenna to minimize the noise figure of the whole system. A semi-rigid cable is used as an inflexible and sturdy support structure. A post amplifier and filter are used for operation of the WiBAR in the $1-3$GHz frequency band. The radiometer runs on two $9V$ batteries connected to $5V$ regulators. The radiometer output is connected to a handheld Spectrum analyzer using a long coaxial cable to measure the power spectrum of the incident brightness temperature. The radiometer is installed over a light-weight PVC pipe structure with two degrees of freedom that provides easy orientation required for measurements.

This system is capable of detecting the thickness of snow accurately. The wide beamwidth and low directionality of the antenna provides detection of average snow thickness in the footprint of the antenna in open air. Even in the presence of vegetation and forest canopy, this WiBAR is capable of detecting the thickness of snow. This generation of WiBAR enables us to detect the snow thickness in the presence of smooth rough interfaces, forest canopy, and radio frequency interference. The third generation of WiBAR is designed to operate under harsh environmental condition, remotely and autonomously. We used the same structure as in the first generation with the frequency range. The block diagram of the third generation WiBAR is shown in Fig. 3.3 (c). The WiBAR has been installed inside an enclosed box, aka Ice Sensing Network (ISN) system. An image of the ISN system is shown in Fig. 3.3 (f). The ISN is part of Ice Force Measuring System (IFMS), which is used to measure the force exerted from ice to a metallic structure. The IFMS mechanical structure and analysis is outside the scope of this dissertation. The IFMS system was installed on the South

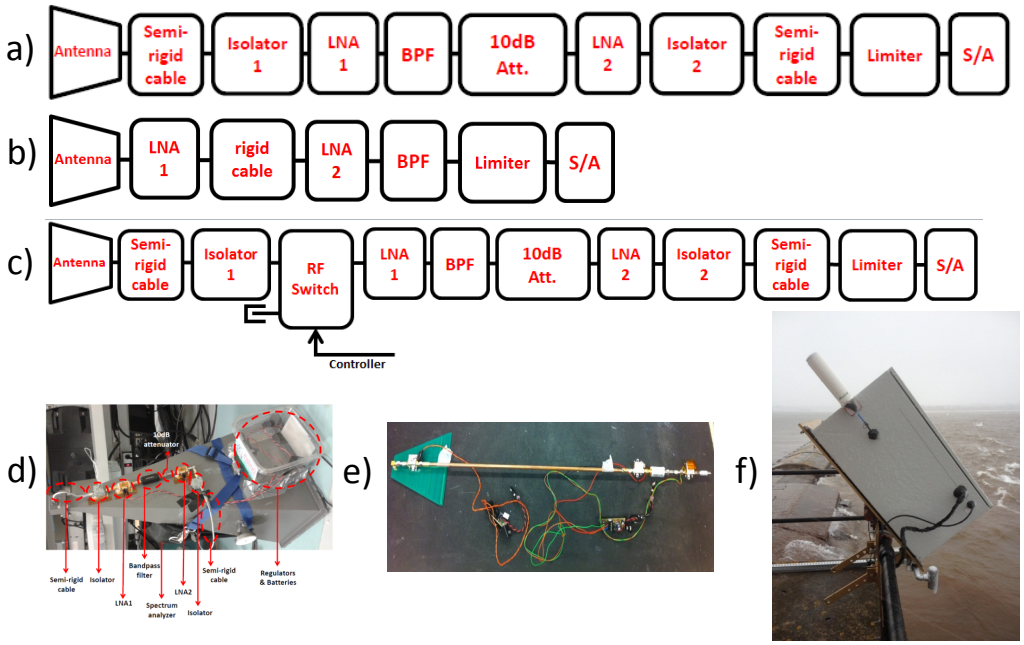

Figure 3.3: Schematics of the (a) first, (b) second, and (c) third generations of the WiBAR. The photo of the (d) first, (e) second, and (f) third generation.

Entry lighthouse in Keweenaw Bay, Lake Superior. The goal of this system, which WiBAR is a part, is to measure the ice force exerted to a vertical structure (offshore wind farm) as a function of ice thickness. The tracking of ice activity is also possible using this system. The system configuration is shown in Fig. 3.4. The system in the box consists of a router and ethernet switch, which handle the data transfer to the internet. The controller is a BeagleBone, that can control all the devices in the system. The power is provided by solar panels. The spectrum analyzer is connected to the WiBAR to capture the data. All the actions and timing are controlled by controller. The data is sent to internet using the cellular network.

In order to make the system weather-resistant, several thermal tests have been performed on the different parts of the system separately. The thermal test setup is shown in Fig. 3.5 (a) and (b). The changes in the WiBAR gain as a function of frequency at 35°C and −40°C are shown in Fig. 3.6. The gain is higher at lower temperature by about 1dB in average compared to higher temperature. This increase

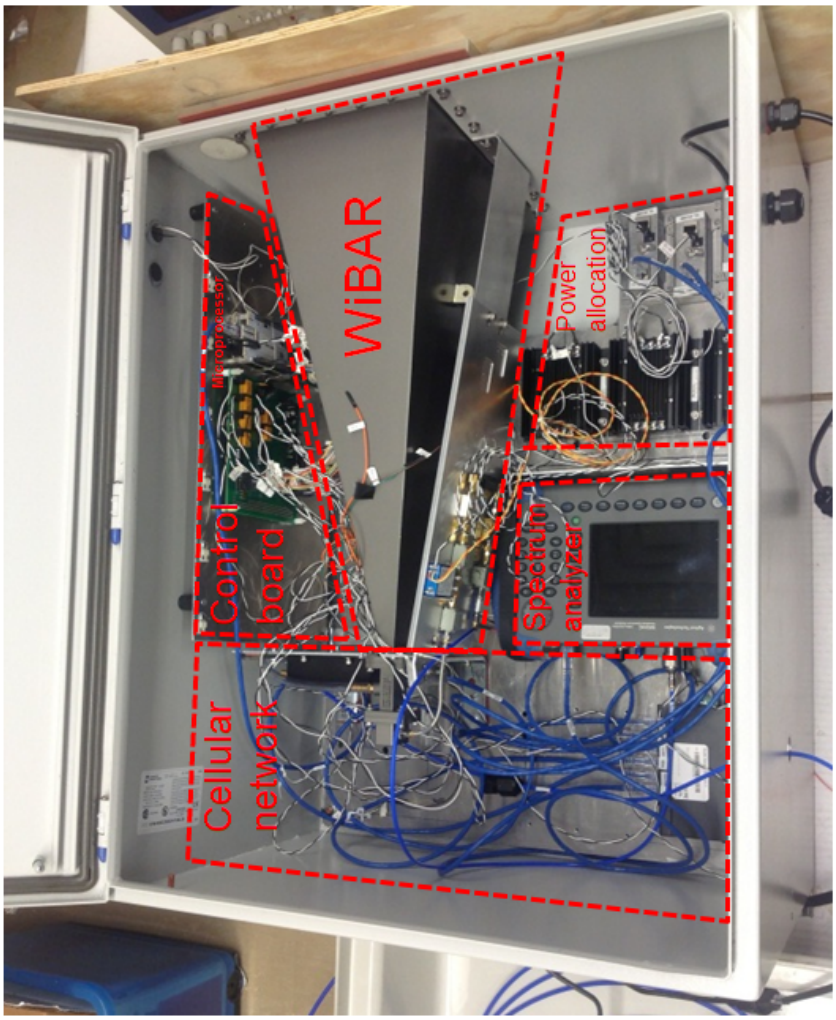

Figure 3.4: The WiBAR system integrated into a box.

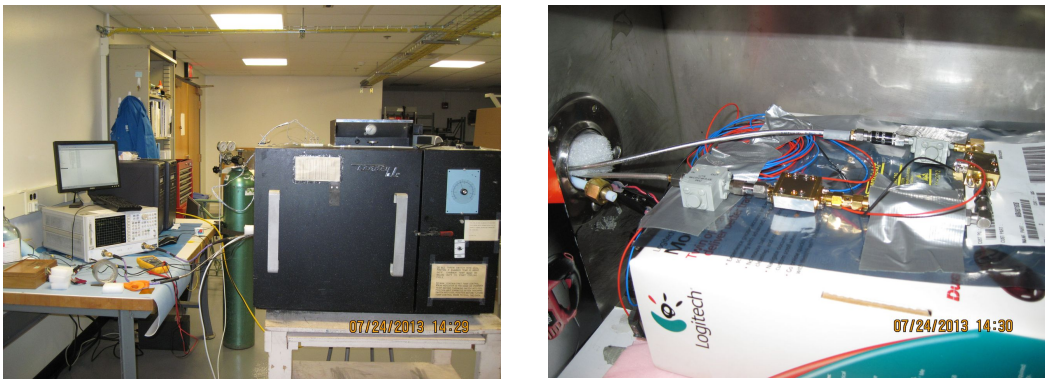

Figure 3.5: (a) The thermal setup used to characterize the system response. (b) The microwave circuit inside the thermal chamber.

in the gain is due to the increase in the gain of LNAs inide the WiBAR and also increase in the gain of Spectrum Analyzer at low temperatures.

3.2.2 Calibration Procedure

Since in WiBAR the accurate absolute value of brightness temperature is not required, the calibration procedure is different from other radiometers. In the calibration procedure, three sets of measurements are obtained from cold sky, ambient absorber, and the layered medium.

In each resolution bandwidth the detected power spectral data is equal to $P(\omega) = kT(\omega)B_rG_s(\omega)$, where k is the Boltzman's constant, T is the system temperature in Kelvin, B_r is the resolution bandwidth, and G_s is the radiometer gain. The system temperature consists of the summation of the receiver temperature (T_R) and the antenna aperture temperature (T_A). In the first measurement, sky measurement, $T_A(\omega) = T_{sky}(\omega)$, which is low and almost constant over our desired frequency band. In our other measurements, the antenna aperture temperature is equal to $T_A(\omega) = e(\omega)T_{object}$, where $e(\omega)$ is the emissivity and T_{object} is the physical temperature of the object and can be assumed constant with respect to frequency. In our frequency range

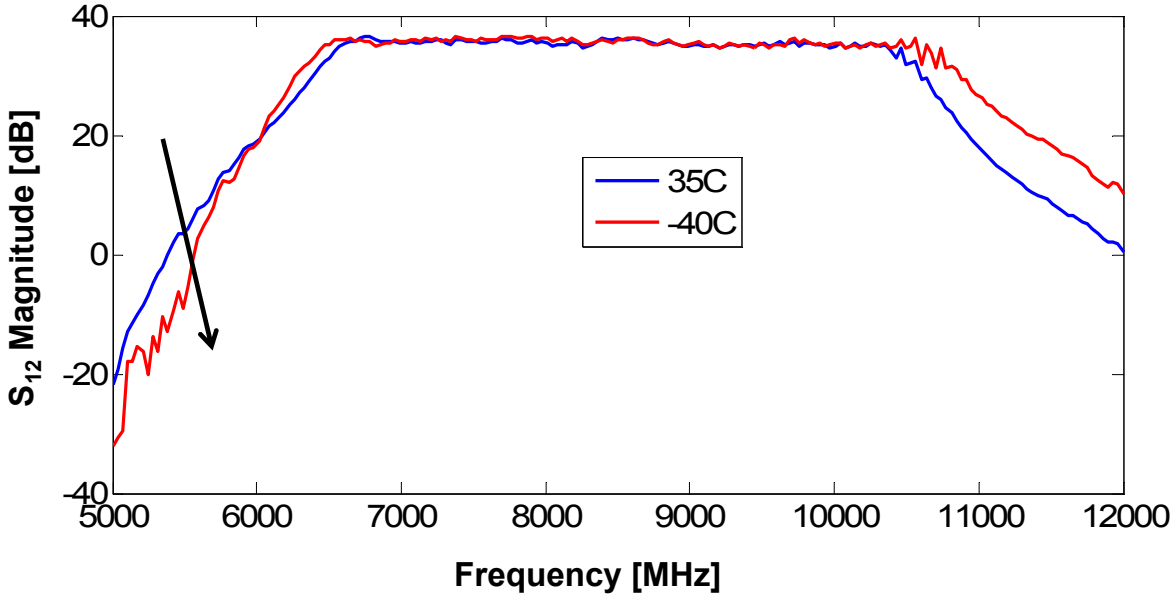

Figure 3.6: WiBAR response as a function of frequency at 35 and −40 degree Celsius. The changes are shown by arrow as temperature decreases.

of interest the atmosphere can be considered lossless, when looking downward to the object. The physical temperature of the hot absorber and the slab are significantly larger than the sky temperature. The emissivity of the hot absorber is almost unity. The slab emissivity as a function of angular frequency is given by (3.1) (78).

$$e_{slab}(\omega) = \frac{(1-|\rho_1|^2)(1-|\rho_2|^2)}{1+|\rho_1|^2|\rho_2|^2+2|\rho_1||\rho_2|cos(\omega\tau)}, \tag{3.1}$$

where τ is the microwave transit time delay between the direct path and the doubly reflected path due to the internal reflection inside the layer. ρ_1 and ρ_2 are the top and bottom surface reflection coefficients, respectively. In this formulation, we assumed that the slab is almost lossless (low-absorbing and low scattering); therefore both the extinction of the slab and self-emission of the slab are both negligible.

In order to isolate $e_{slab}(\omega)$ from other frequency dependent parameters, we can use the ratio of the power spectral density of the slab corrected by that of sky over

the hot absorber power spectral density corrected by that of sky as given by (3.2).

$$
\begin{aligned}
& \frac{P_{slab} - P_{sky}}{P_{abs} - P_{sky}} \\
= \; & \frac{G_{slab}(e_{slab}(\omega)T_{slab} + T_{R,slab}) - G_{sky}(T_{sky} + T_{R,sky})}{G_{abs}(e_{abs}T_{abs} + T_{R,abs}) - G_{sky}(T_{sky} + T_{R,sky})} \\
= \; & \frac{e_{slab}(\omega)T_{slab}G_{slab} + (T_{R,slab}G_{slab} - T_{R,sky}G_{sky}) - T_{sky}G_{sky}}{e_{abs}T_{abs}G_{abs} + (T_{R,abs}G_{abs} - T_{R,sky}G_{sky}) - T_{sky}G_{sky}} \\
\approx \; & \frac{(e_{slab}(\omega)T_{slab} - T_{sky})G_{slab}(\omega)}{(e_{abs}T_{abs} - T_{sky})G_{abs}(\omega)} \\
\approx \; & \frac{e_{slab}(\omega)T_{slab} - T_{sky}}{e_{abs}T_{abs} - T_{sky}},
\end{aligned}
\tag{3.2}
$$

The subscripts abs, sky, and $slab$ corresponds to instantaneous value of T_R and G at the time those targets were observed. The following simplifications is considered, $T_{R,slab}G_{slab} = T_{R,sky}G_{sky} = T_{R,abs}G_{abs}$ and also $G_{slab}(\omega) = G_{sky}(\omega) = G_{abs}(\omega)$, because the radiometer is stable over the duration of the measurements. Equation (3.2) can be used in the calibration process to solve for the emissivity of the slab. Therefore, the only frequency dependent term is $e_{slab}(\omega)$ and all the other terms are constant with respect to the frequency.

3.2.3 Autocorrelation Response

Finding the amplitude of the autocorrelation response from a finite set of spectral data is similar to spectral analysis of truncated time domain data. In our measurements, the spectral data demonstrate a periodic patterns that we call ripples. The spectral response of these ripples corresponds to a peak in the autocorrelation domain. We have used the inverse fast Fourier transform to extract the temporal response of the power spectral data. We found out that at least two ripples over the frequency span are required for detection of the layer thickness. The minimum detectable thickness is limited by the minimum ripples presented in the bandwidth of the WiBAR.

The maximum thickness is limited by the resolution bandwidth and the number of points in spectrum analyzer.

The minimum and maximum detectable thicknesses depend on the refractive index of the medium (ice or snow) as well as the antenna's angle of incident. On the other hand, the minimum or maximum delayed travel time (τ) is primary a function of the layer thickness and antenna angle of incident. The measured power spectral response has ripples in the frequency domain with their amplitude directly proportional to the amplitude of the autocorrelation peak. The limitation in maximum detectable travel time is due to inability to separate the peaks in the power spectral domain, limited by the resolution bandwidth and the number of frequency bins. The minimum detectable travel time is constrained by the overall bandwidth. Our findings suggest that at least two full cycles of the ripples are required for correct reconstruction of the travel time. From these information, the minimum and maximum travel times can be bounded as given by (3.3). The choice of the resolution bandwidth is limited by the maximum detectable thickness that we plan to detect with WiBAR. The choice of the frequency span is limited by the minimum detectable thickness criteria.

$$\frac{m}{(f_{max} - f_{min})} < \tau < min\{\frac{N_p}{2(f_{max} - f_{min})}, \frac{1}{2B_{resolution}}\}, \tag{3.3}$$

where m and N_p are the number of full period of ripples in the overall bandwidth and the number of total frequency bins in spectrum analyzer. $f_{max/min}$ is the maximum/minimum allowable frequency. In case, $m = 2$, $f_{min} = 7GHz$, and $f_{max} = 10GHz$, the minimum detectable thickness for snow and ice are approximately $8.33cm$ and $5.6cm$, respectively. The thickness resolution can be as good as $4.15cm$ and $2.8cm$ for snow and ice layers, respectively.

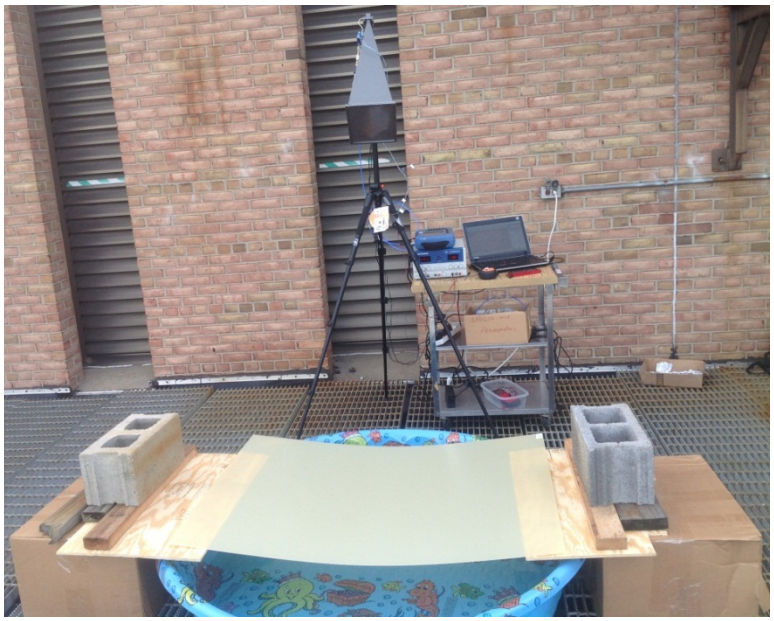

a)

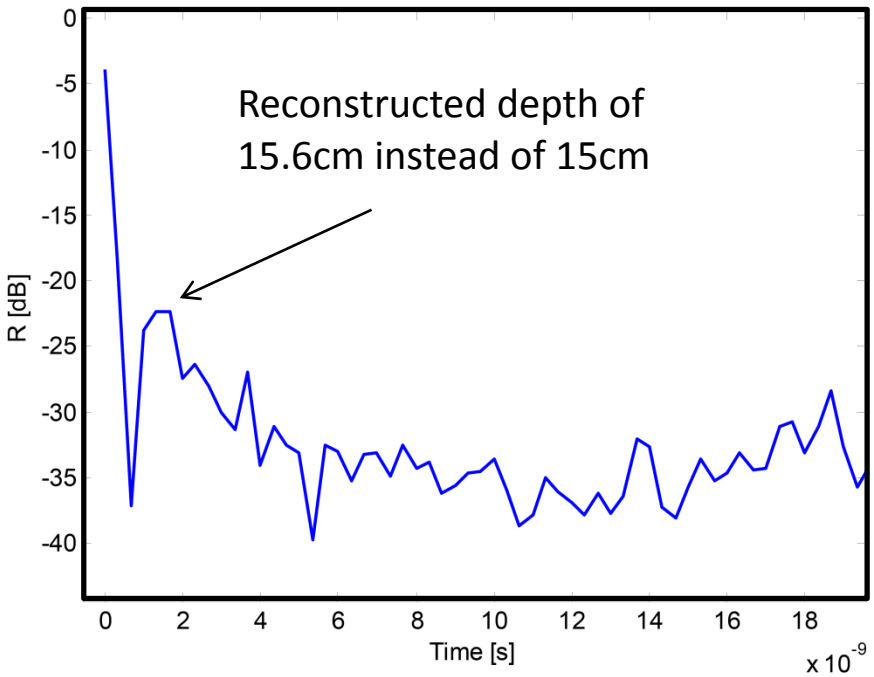

b)

Figure 3.7: (a) The measurement setup for the thickness measurement of air gap over water. (b) The autocorrelation response of the measurement as a function of microwave transit time. The equivalent thickness is shown by the arrow in the inset.

3.3 Measurement Results

In this section the measurements are collected by a handheld spectrum analyzer ($AgilentN9344C$) with a maximum frequency of operation of $20GHz$. The resolution bandwidth is set to $3MHz$, the frequency span is $3GHz$ covering the frequency range of $7-10GHz$. The video bandwidth is fixed at $300Hz$ as suggested by the optimization procedure explained in Subsection 2.4.0.2. The signal to noise ratio (SNR) is $-22.15dB$. In order to verify the functionality of the WiBAR as well as the validity of our thickness detection algorithm, we have performed several measurements on different layered media including air gap between water and a thin high dielectric constant sheet ($FR4$), fresh water ice, and snow layer over the terrain. In our analysis, we have assumed that the dielectric constant of ice at our frequency range of interest is 3.15 (80). Based on the measurements that we performed and also theory, the minimum detectable ice thickness should be $5cm$. We gathered the horizontally polarized (H-pol) far field measurements of lake ice or snow covered terrains using our implemented WiBAR at several locations in Michigan under varying conditions and thickness values. Rather than use of model-based estimates of the snowpacks average dielectric properties, we used the refractive index mixing formula and snow density profiles measured in snow pits. The reconstructed estimated snow thicknesses are in good agreement with *in-situ* measurements. The far-field measurement is the basis for remote sensing of ice and snow. The accuracy of the test scenarios verify the potential of the WiBAR for airborne/spaceborne remote sensing of snow and ice. In the following Subsections 3.3.1,3.3.3, and 3.3.2, the farfield thickness measurement of air gap, lake ice, and snow over asphalt are presented.

3.3.1 Far-field measurement of air gap between fresh water and FR4 sheet

We claimed that our WiBAR is capable of detecting the thickness of any low-absorbing layered media. In order to verify this claim, we prepare a test scenario,

a)

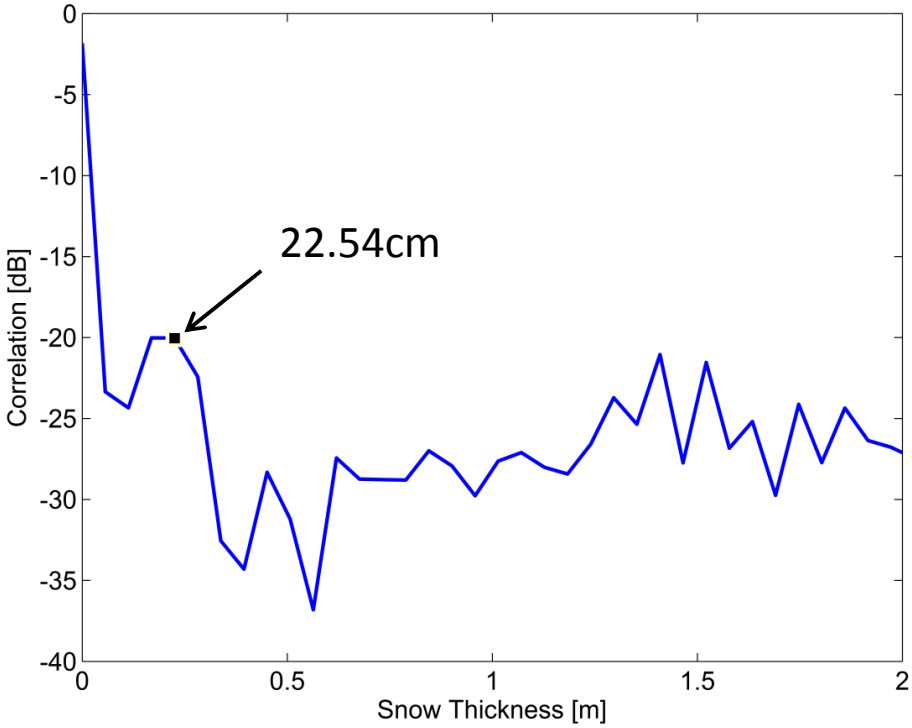

b)

Figure 3.8: (a) The measurement setup for the thickness measurement of snow over terrain. (b) The autocorrelation response of the measurement as a function of snow layer thickness. The reconstructed thickness is shown by the arrow in the inset.

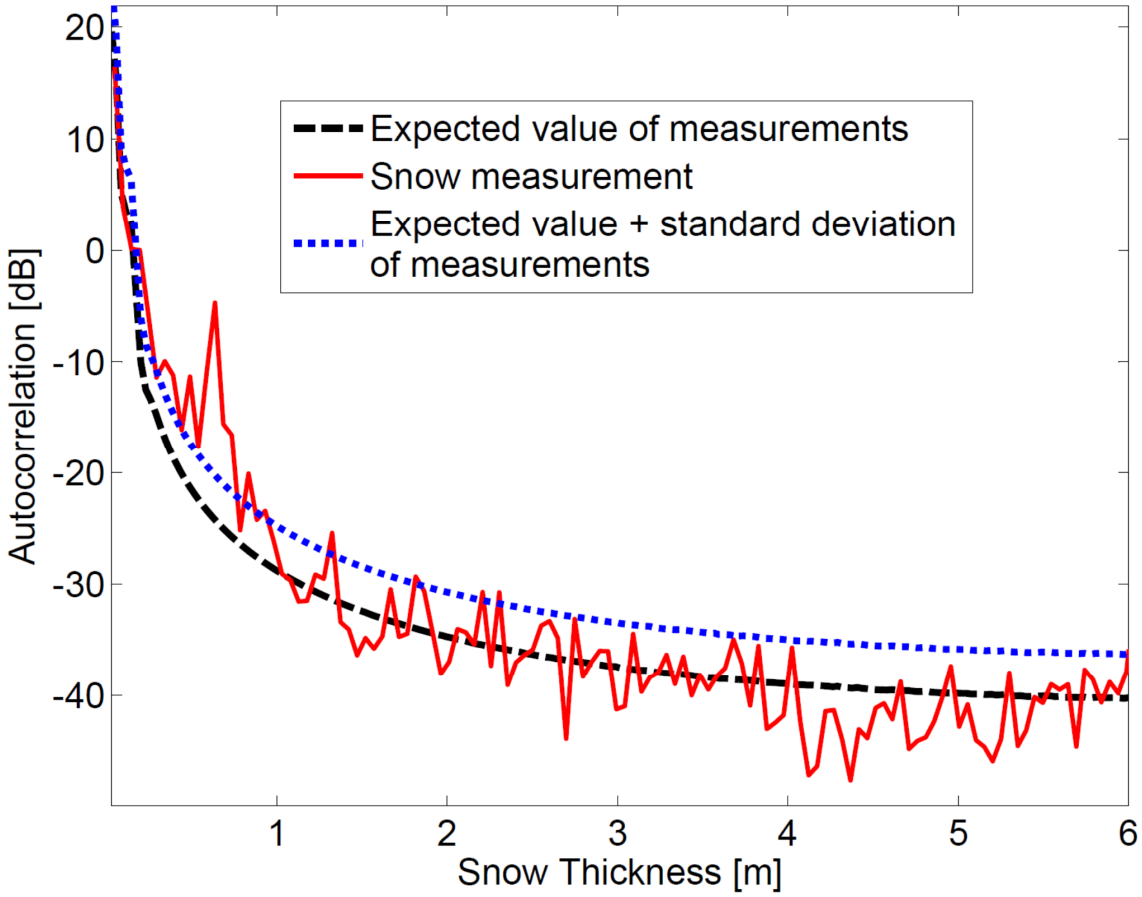

Figure 3.9: The autocorrelation response of the measurement as a function of the snow layer thickness (solid red line) as well as the expected value of the measurement (dashed black line) and the summation of standard deviation and expected value of the autocorrelation response (dotted blue line) using modified post processing technique. The first generation WiBAR is used.

Figure 3.10: The setup used to measure the snow thickness using the second generation of WiBAR. 64cm of snow (ground-truth) is detected at University of Michigan Biological Station (UMBS) at Pellston, MI.

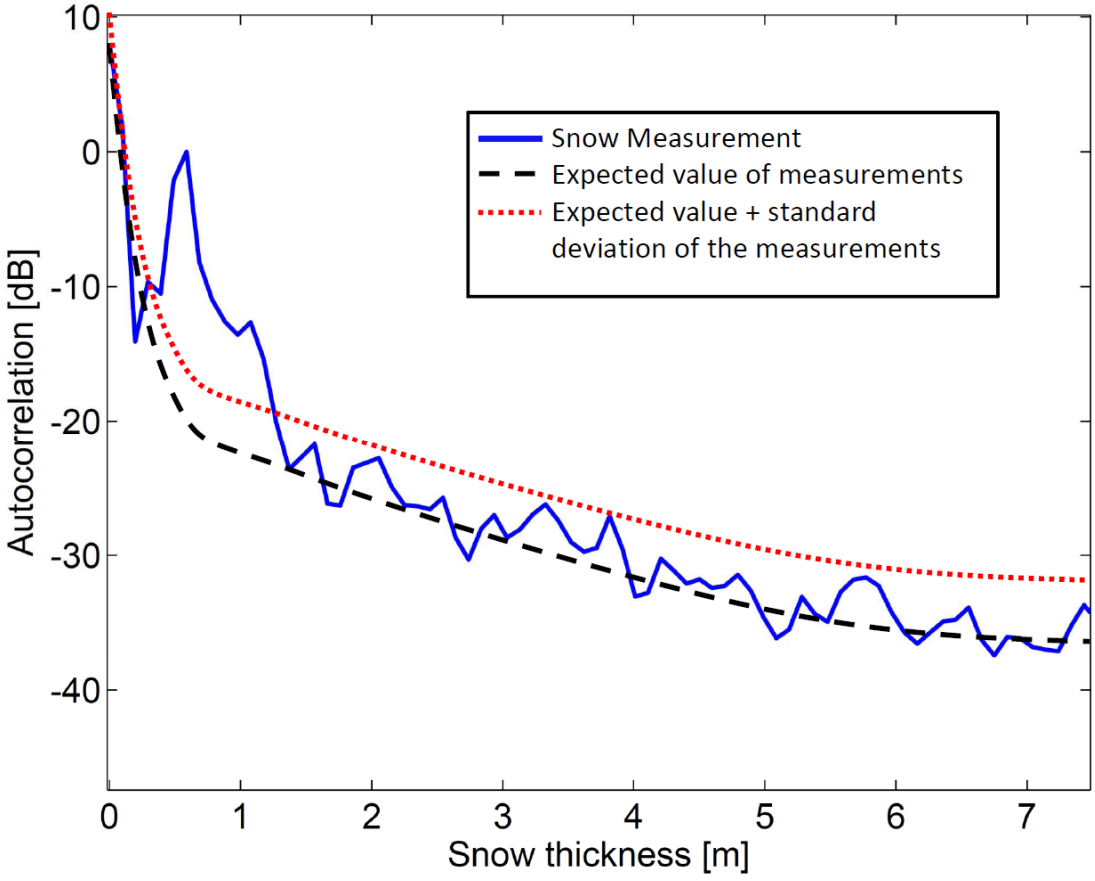

Figure 3.11: The autocorrelation response of the measurement as a function of the snow layer thickness (solid red line) as well as the expected value of the measurement in the absence of layer (dashed black line) and the summation of standard deviation and expected value of the autocorrelation response (dotted blue line) using modified post processing technique. The second generation WiBAR is used.

in which an air gap is between the water inside a small pool and a high dielectric constant thin sheet. We have chosen $FR4$ due to its high dielectric constant (ϵ 4.3) and stiffness. Our calculations as well as simulation results show that the water emission is reflected back partially at the interface of the sheet. We have verified our calculations by placing two antennas at the far field of each other with and without the sheet placed in the middle of them. The measurement setup consists of two antennae a $FR4$ sheet in the middle and a network analyzer. The S_{12} (transmission) of two cases including the measurement with and without the sheet are compared and the reflectivity of 0.11 is estimated. By placing the sheet over the pool the water emission is partially reflected back and forth inside the air gap layer. Using WiBAR, we have been able to find the thickness of the air gap for several scenarios by varying the water level in the pool. One test scenario as well as the reconstructed results are shown in Fig. 3.7 (a) and (b), respectively.

The measurement results, shown in Fig. 3.7 (b), are in good agreement with the $in-situ$ measurement of the gap using a measure tape. The error in the measurement is within $0.6cm$. The effect of curvature in the $FR4$ (sag) is the widening of the peak.

3.3.2 Far-field measurement of snow layer

The second set of measurements are performed for further verification of the radiometer's operation. In the first scenario, a naturally formed snow pack with the depth of $21cm$ is considered over the asphalt. A representative measurement setup as well as the autocorrelation response as a function of snow layer thickness are shown in Fig. 3.8 (a) and (b), respectively.

The detected peak is located at $22.54cm$. The dielectric constant of snow is calculated using refractive index mixing formula for a proper portion for the ice and air. The proper ratio is observed on site by measuring the density of the snow. The accuracy of this method is within $1.5cm$ for the snow measurements.

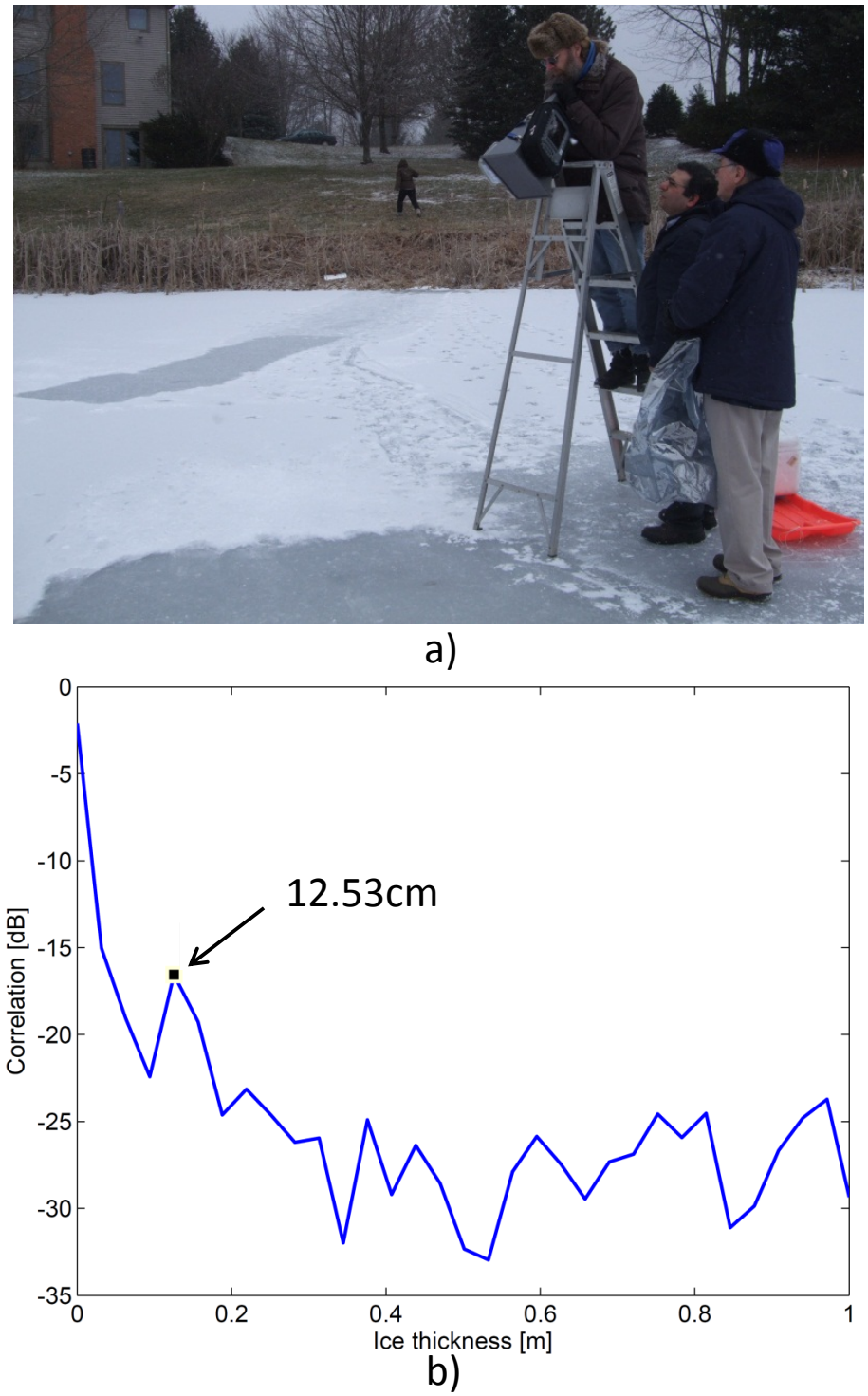

Figure 3.12: (a) The measurement setup for the thickness measurement of lake ice over water. (b) The autocorrelation response of the measurement as a function of the ice layer thickness. The reconstructed thickness is shown by the arrow in the inset.

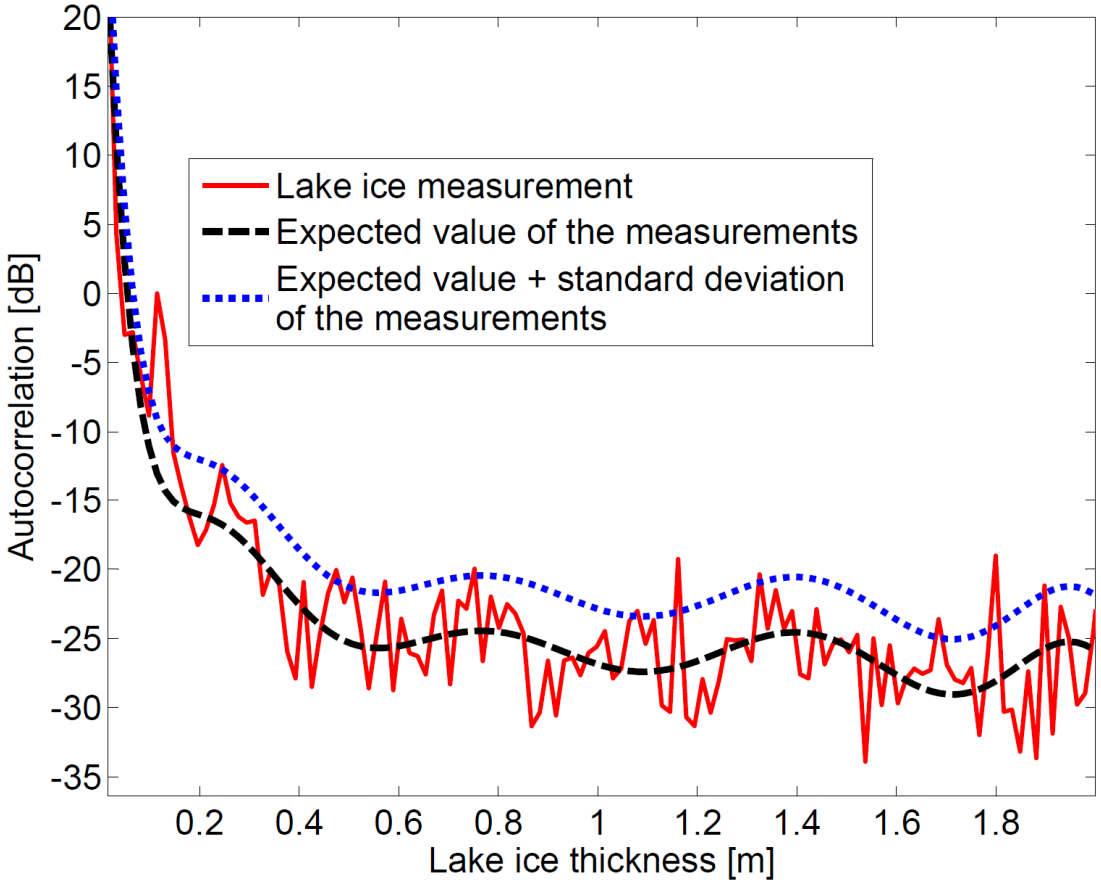

Figure 3.13: The autocorrelation response of the measurement as a function of the ice layer thickness (solid red line) as well as the expected value of the measurement (dashed black line) and the summation of standard deviation and expected value of the autocorrelation response (dotted blue line) using modified post processing technique.

In the second snow thickness measurement, a naturally formed snow pack with the thickness of $64cm$ over a smooth terrain is observed using the second generation WiBAR. The measurement result and test setup are shown in Figs. 3.9 and 3.10, respectively. The accuracy of this measurement compared to ground-truth measurement is within $1cm$. The third measurement is performed with $64cm$ of snow over undulated terrain under the forest canopy. The measurement result is shown in Fig. 3.11. The accuracy of this measurement is within $1.5cm$.

3.3.3 Far-field measurement of ice layer

The measurement of fresh-water ice thickness is performed on a Dexter,MI pond with ice thickness around $11.7cm$. The thickness has been measured *in-situ* using a tape measure in a hole drilled through the ice by a hand drill. We should also highlight that the *in-situ* measurements have accuracy within $1cm$ due to the ice layer perturbation caused by the drilling. The measurement setup is shown is Fig. 3.12 (a) and the autocorrelation response is shown in Fig. 3.12 (b). The accuracy of this measurement is within $0.87cm$. The ice thickness measurement using autocorrelation radiometer is in good agreement with the $in-situ$ measurement.

3.4 Ice activity at the Lake Superior

The third generation of WiBAR is installed over Lake Superior as shown in Fig. 3.14. The ice activity is monitored and analyzed over the Winter 2014. The result is shown in Fig. 3.15 and compared with the ice thickness estimated using stereo imaging. The autocorrelation response of the WiBAR for February 8th and 19th are shown in Fig. 3.16.

Figure 3.14: The installation of the system over Lake Superior. Photo is the courtesy of kite Aerial Photography, with Nathan Invincible.

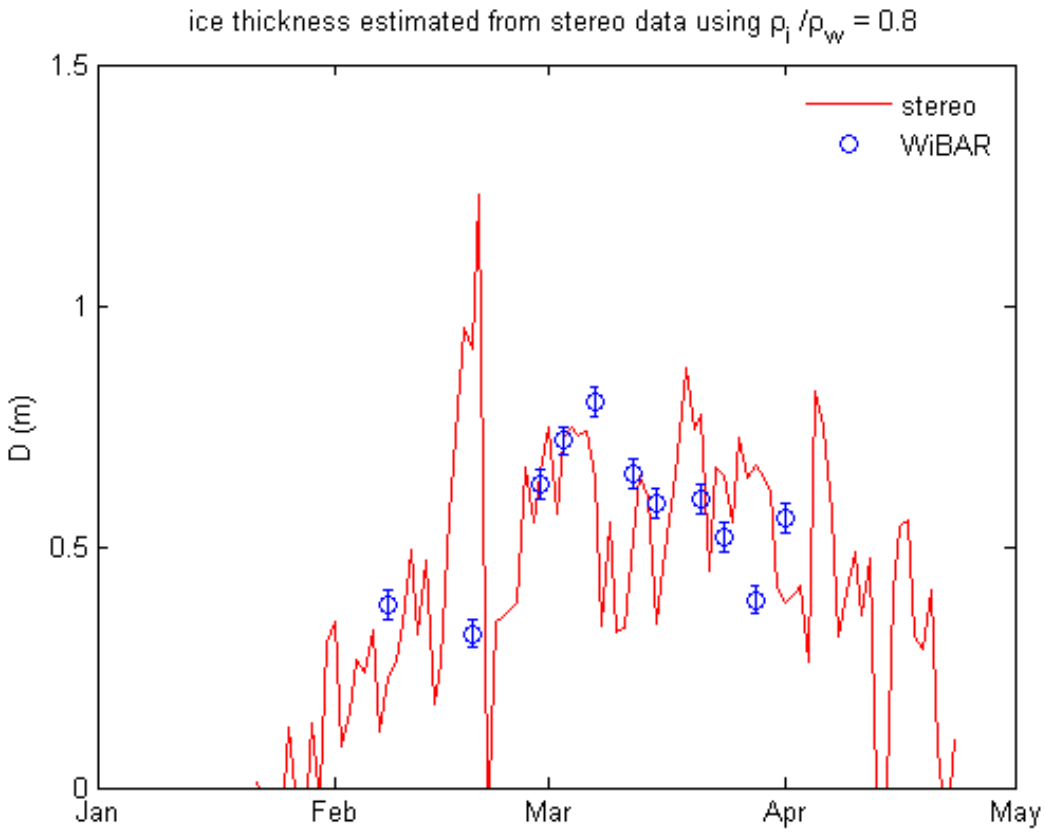

Figure 3.15: The result of WiBAR analysis (blue circles) is compared with the stereo imaging (red solid line). Courtesy of David Lyzenga.

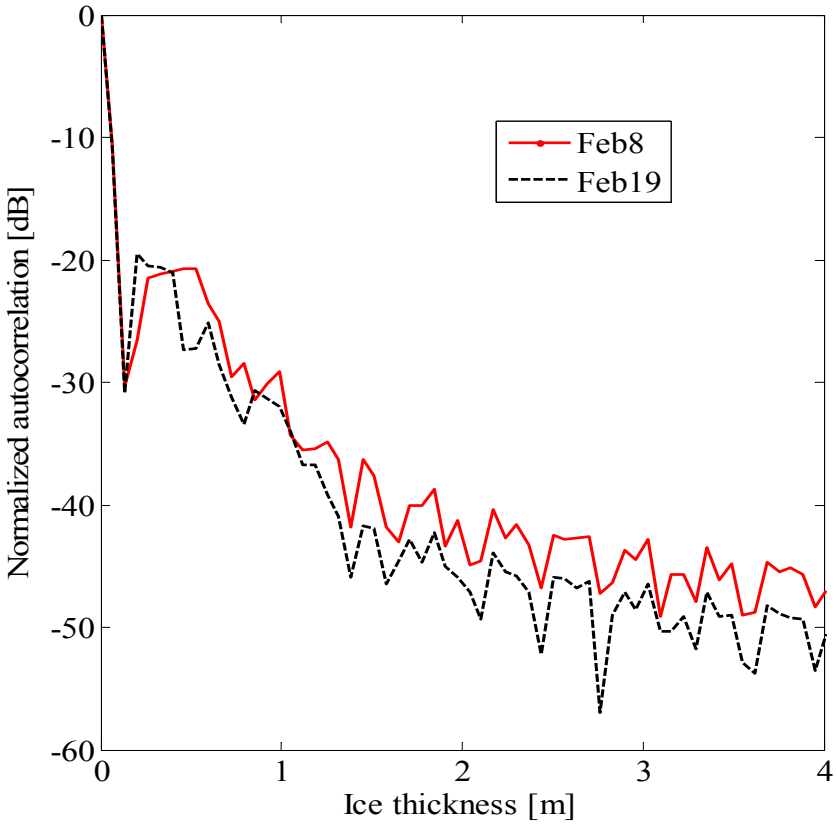

Figure 3.16: The autocorrelation response as a function of ice thickness for February 8th and 19th, 2014. The measurement is over the Lake Superior at the south entry lighthouse Keweenaw bay near Houghton, MI.

CHAPTER IV

Theoretical Investigation of WiBAR

4.1 Introduction

In this chapter, the post processing techniques to detect the microwave transit time delay is presented. In the first part of this section, the post processing techniques to detect the periodicity of the strong and weak ripples are introduced. In the second part of this section, theoretical analysis of the sloped top interface as well as the impact of roughness on the coherent emissivity is explored. The impact of the antenna beam width, marching out of the antenna foot print, and analysis of the impact of radio frequency interference (RFI) are investigated. At the end of this section, a compressive sensing based technique using approximate message passing and orthogonal matching pursuit algorithms applied to a random demodulation structure is explained.

4.2 Post processing

In this section, the post processing techniques are explained. We are interested to detect a sine wave (ripples) buried in noise. It should be pointed out that in our system the role of time and frequency are interchanged from their usual roles. We are interested to find a sine wave in the frequency domain. However, the common

techniques rely on finding a sine wave in time domain. We refer to the autocorrelation response as the estimated spectrum in this chapter. The common technique to recover the sinusoidal wave is the spectrum estimation techniques used in time series analysis. These techniques can be classified into parametric and non-parametric methods. The parametric methods assume a known statistics for the process with a number of parameters. The most common parametric methods are autoregressive (AR) and moving average (MA). In these algorithms, the goal is to estimate the parameters. However, in the non-parametric methods the covariance or the spectrum is estimated without any assumption for the underlying process. Eigenanalysis procedures or harmonic decomposition techniques are also of interest for certain applications. These methods try to find the best estimate for the spectrum using a basis vector formed by the eigen values or the Fourier basis vectors. The Multiple Signal Classification (MUSIC), Pisarenko harmonic decomposition, and eigen vector based techniques are used in the literature.

The most common non-parametric algorithms are FFT (70), periodogram, windowed periodogram, which are called based on the choice of the window as Bartlett, Bartlett-Hanning, Welch, Multitaper, Blackman, Blackman-Harris, Bohman, Chebyshev, Rectangular (Flat top), Triangular, Gaussian, Hamming, Hann, Kaiser, Nuttall, Parzen, Tukey. The windowed periodograms can be overlapping or non-overlapping. In the overlapping windows, the adjacent windows overlap. The overlap reduces the noise floor and the variance of the estimated spectrum.

By comparing the variance and bias of all the above mentioned spectrum estimation techniques, the autoregressive technique based on Yule-Walker equation (73; 72) has been chosen. The Yule-Walker equation is capable of reducing the noise and variance by computing the expectation of the model parameters with the their lags, which reduced the impact of ambient noise on the autocorrelation response. The input data should be zero mean.

After calibrating the measured data by the load and sky data, the inverse of the calibrated data is used as the input to our spectrum estimation technique. We apply a high order autoregressive method based on Yule-Walker equation. The peaks of the resulted estimated spectrum is then tested by weak signal detection techniques. In the case of weak sinusoidal wave detection buried in strong noise, several algorithms have been developed for applications such as seismic wave detection used for earthquake analysis, or machinery fault detection in the early stage of the fault. These techniques are mainly focuses on efficient noise reduction techniques. The noise reduction can be performed by filteration and utilization of chaotic oscillators (84; 83; 85; 44).

Chaos is long-term non-predictive aperiodic behavior in certain nonlinear dynamical systems. Due to the high sensitivity of the system to the initial state, any perturbation of the system will grow exponentially in time resulting in the non-predictive behavior of the system. These characteristics of the system response can be utilized as a random sequence generator, which is widely used for security purposes, such as cryptography, communication channel testing, and random bit generation (9; 53; 55; 7; 19; 6; 8). Chaos based systems can be categorized into two different classes including discrete-time chaotic maps and continuous-time chaotic oscillators (54; 52).

A chaotic oscillator is a dynamical system that generates a deterministic behavior, which is a strong function of the initial values. Chaotic oscillating systems can be defined by a set of nonlinear differential equations. The source of nonlinearity can be the non-linear resistors or elements in the autonomous chaotic oscillator. However, in non-autonomous systems, the source of non-linearity is the excitation signal included in the system. Non-autonomous chaotic oscillators have different reactions to input signal. Some systems strongly depend on the input signal for oscillation so that the system parameters vanish abruptly or increase infinitely when there is no excitation. The next type of these systems merges to an oscillatory scheme by

removing the excitation. The last type is a low power system, in which the chaotic output signal can be generated even when we remove the input excitation. Chaotic oscillators have a great potential to be utilized in the generation of random bits for cryptographic systems, and chaos based communications. In addition, chaos-based system analysis is a potential emulator for human organs in biomedical applications, such as emulating the performance of the brain and heart. Discrete-time chaotic maps are discrete in nature and have a great potential for digital applications, such as random number generation. Chaotic oscillators are continuous-time chaotic sources that can be utilized in continuous-time systems, such as chaos based communications and the modeling of biological systems. Chaotic oscillators can be realized by the introduction of a non-linear element in the conventional oscillator circuits. The non-linearity could be realized by either non-linear elements or input excitation pulses. Autonomous chaotic oscillators, such as Chuas circuits, are examples of chaotic oscillators with non-linear resistors. Autonomous chaotic oscillators can be excited by any noise accumulated inside the circuit, such as the charge noise accumulated on a capacitor or the environmental magnetic noise accumulated on an inductor. Therefore, autonomous chaotic oscillators do not need any external excitation signals. On the other hand, non-autonomous chaotic oscillators are driven by an input bipolar pulse train as the source of non-linearity and excitation. Comparators are also used as other sources of non-linearity. The chaotic behavior of the system is strongly dependent on the input pulse train, hence, changing the duty cycle or the frequency of the excitation pulse can lead to a different chaotic trajectory in the phase space. Leveraging the fixed level of the pulse train as the source of excitation in the circuit results in fixed equilibrium points in the trajectory diagram of the system.

Chaotic oscillators can be implemented by inserting a nonlinear element in the conventional oscillators. Chaotic oscillators can produce an almost uniform response in the neighborhood of the oscillators main frequency. This uniform frequency re-

sponse can be used in the generation of nonpredictive signals close to the desired frequency and can be utilized for the secure transmission and synchronization of the data through chaotic signals. In chaos-based communication systems, chaotic oscillators can replace the conventional sinusoidal oscillators due to the simultaneous achievement of good synchronization and security. In these systems, it is necessary that the bandwidth of the chaotic carrier be larger than that of the transmitted message for the proper operation of the system.

The Duffing chaotic oscillator is the most common chaotic oscillator that can be used for noise removal. The Duffing oscillator can be formulated as given by equation 4.1.

$$\ddot{x} + a\dot{x} + bx + cx^3 = dcos(\omega t), \tag{4.1}$$

where a, b, c, and d are the coefficients. t, x, and ω refer to time, position and angular frequency, respectively. By a wise choice of the coefficients, the dynamic behavior of this oscillator is a function of the value of the coefficient d. For very small value of d, the dynamic system is on small-scale periodic state, however after a threshold, the system is in the chaotic state and for larger values of d, the system enters the large-scale periodic state. If we set the chaotic oscillator slightly below the threshold between the chaotic state and the large-scale periodic scale and add the signal of interest to the right side of the differential equation given by equation 4.1, the chaotic oscillator is capable of removing the noise. The signal of interest should have the same frequency as ω. One way to find a signal of interest with unknown frequency is by scanning the spectrum. The scanning can be efficient and quick, if we only choose the peaks in spectrum estimation.

Lyapunov exponent is a measure that can predict the state of a chaotic system. In general, a negative Lyapunov exponent refers to a stable system and in our dynamic system means oscillatory response. However, the positive Lyapunov exponent refers

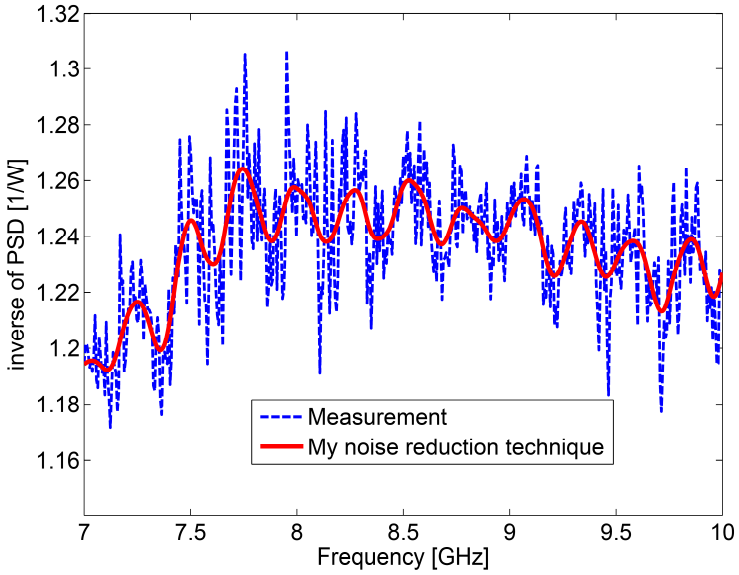

Figure 4.1: The inverse of power spectrum of the measured data at Keweenaw bay, MI. The calibrated data (dashed blue line) and the low pass filtered data (solid red line) are shown. The ripples are easily distinguishable in the filtered data.

to unstable system. The unstability can be due to a chaotic state or due to a diverging system. In our system of equations, the positive Lyapunov exponent means that the system is in the chaotic state. The Duffing oscillator has been solved using 4th order Runge-Kutta method. This method uses four coefficient to estimate the derivative. The Lyapunov exponent is a function of ω. Finding the threshold between the oscillatory and chaotic state requires an accurate estimation of Lyapunov exponent, which is time consuming.

As an example, we have applied this technique to a data set measured at the Keweenaw bay of Lake Superior over winter 2014. The calibrated data is shown in Fig. 4.1. The low pass filter applied to the data for reducing the noise.

The post processing algorithm is shown graphically in Fig. 4.2. In this algorithm, the input data, which is the calibrated data, is fed to a matching filter. This matching filter removes the system response in the calibrated data and ensure that the mean value of the signal is zero. The moving average stage is responsible for this operation.

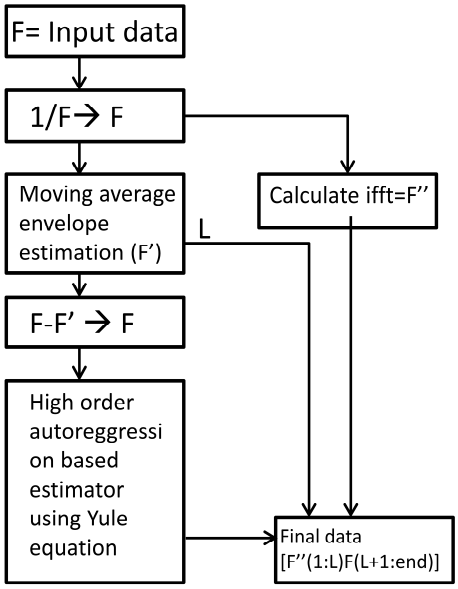

Figure 4.2: The spectrum estimation algorithm used for estimating the autocorrelation response.

The matching filter removes the zerolag peak, because there is no DC term in the response. Based on the order of the matching filter, several low order terms (L terms) vanishes. This operation limits the minimum detectable ice thickness to 20cm. In order to compensate for that, we replace the low order terms by applying the IFFT algorithm to the data. The order of our matching filter is 10, which removes the first 4 data. The algorithm has been applied to a set of measured data and the results compared with the simple IFFT applied to the data. The results are shown in Fig. 4.3. The noise floor is much smaller in our post processing algorithm compared to IFFT. The estimated spectrum using the Yule-Walker autoregressive technique is shown in Fig. 4.4. The delay peak is higher than the summation of the expected value and the standard deviation. The peak is tested by chaotic oscillator and the trajectory is chaotic as shown in Fig. 4.5. We have tested other peaks using the chaotic oscillator

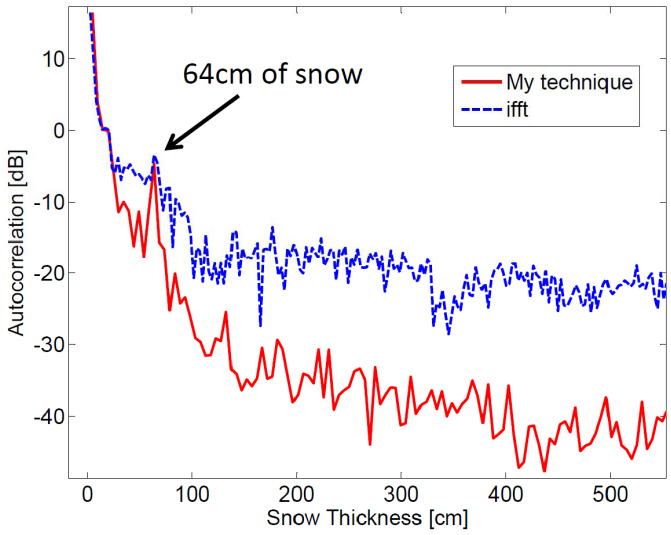

Figure 4.3: The autocorrelation response of the measured snow thickness of 64cm measured at University of Michigan Biological Station (UMBS), Pellston, MI. The autocorrelation response using our algorithm (red solid line) is compared with IFFT algorithm (dashed blue line).

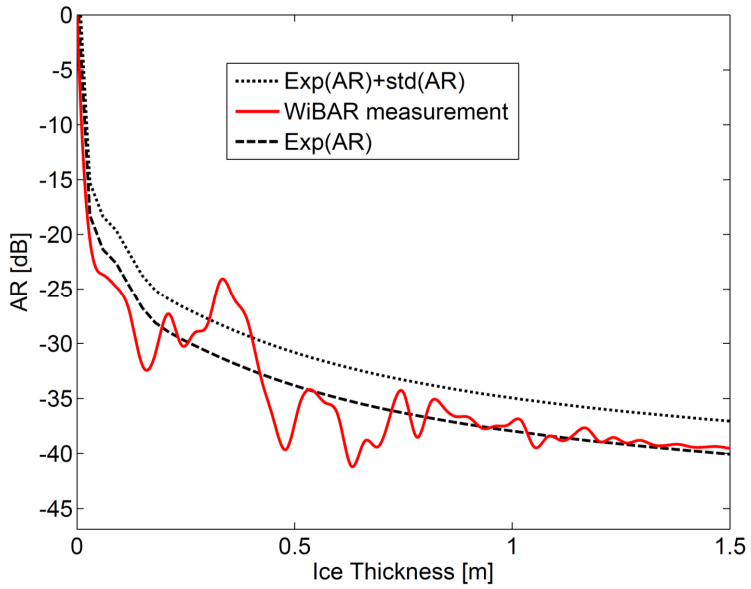

Figure 4.4: The autocorrelation response of the measured ice thickness data measured at Keweenaw bay, MI. The autocorrelation response (red solid line) as well as the expected value of the autocorrelation response (dashed black line) and the summation of the expected value and the standard deviation of the autocorrelation data (dotted black line) as a function of ice thickness are shown.

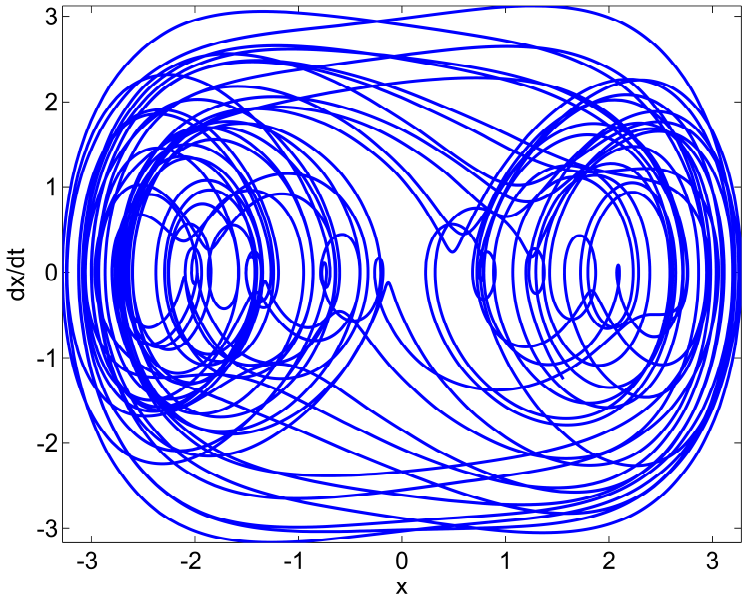

Figure 4.5: The trajectory of the Duffing oscillator for the chaotic state obtained at the peak of the estimated spectrum.

and the trajectory is oscillatory as illustrated in Fig. 4.6.

4.3 Radio frequency interference (RFI)

Any transmitter antenna radiates at specific bandwidth. When the transmitter antenna is in the footprint of the radiometer antenna and its frequency is within the frequency bandwidth of the radiometer, its radiation is detected by the radiometer. These manmade signals are referred as radio frequency interference (RFI). The remote sensing community has demonstrated that microwave radiometry is subject to radio frequency interference (RFI) (17; 51). RFI is additive and usually narrowband. In our wideband implementation, narrowband RFI is presented in power spectral data recording. However, applying the inverse Fourier transform in the post-processing unit diminishes the impact of RFI. Narrowband RFI can be modeled as impulse delta function in the power spectral domain. Applying the inverse Fourier transform to the impulse delta function distributes equally the power of RFI among different autocorrelation time components. Therefore, the effect of narrowband RFI is often

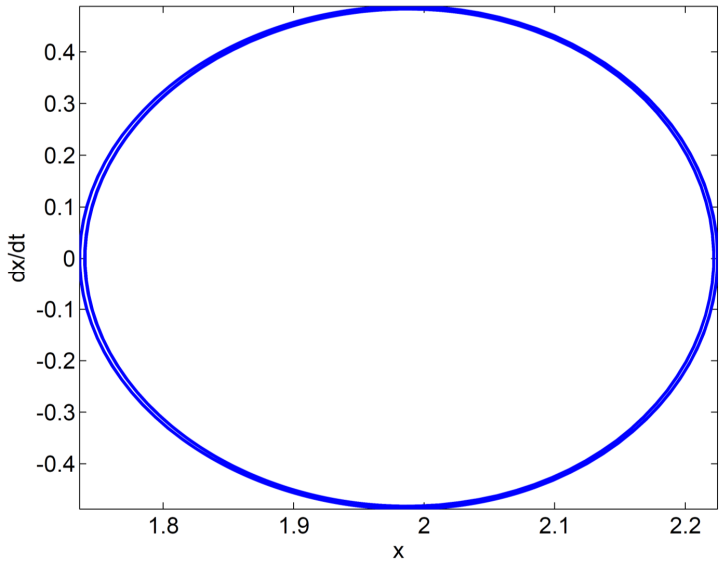

Figure 4.6: The trajectory of the Duffing oscillator for the oscillatory state obtained at other peaks of the estimated spectrum.

negligible except for increasing the noise floor. We are able to successfully recover the autocorrelation response in the presence of RFI. RFI signals can be both in the continuous wave (CW) or discrete pulse train forms. For proper detection of brightness temperature of the scene under test, these RFIs should be detected and eliminated. There are several techniques to detect RFIs, including temporal, spectral, spatial, Stokes, and statistical detections. Statistical techniques are of interest due to the Gaussian nature of the detected brightness temperature. Here we use an entropy based technique to detect the RFIs. Entropy is a measure of information in data. If the data are deterministic, there is no information in the data and entropy is zero. Gaussian noise has the maximum entropy among all signals. Finding the entropy of the detected data assists us to find deterministic signals including RFIs. The entropy can be estimated using the distribution (histogram) of detected brightness temperature. The unit of entropy ($H = -\sum p_i log(p_i)$) is *nat*, which is the natural unit for information entropy. The entropy of some common noise distributions are listed below: $H_{Gaussiannoise} = ln(\sigma\sqrt{2\pi e})$, $H_{Uniformnoise} = ln(b-a)$, $H_{Erlang} = (1 -$

$k)\psi(k) + ln(\Gamma(k)/\lambda) + k, \cdots$, where a and b are the interval limits, σ is the standard deviation of Gaussian distribution, and $\psi(x) = \frac{d}{dx}Log(\Gamma(x))$ (38).

The effect of RFI on the expected value of autocorrelation can be investigated using equation 4.2.

$$\begin{aligned} f_v(v) &= \frac{v}{\sigma} e^{-\frac{v^2+P^2}{2\sigma}} I_0(\frac{vP}{\sigma}) \\ f_w(w) &= \frac{1}{2\sqrt{w}}[f_v(-\sqrt{w}) + f_v(\sqrt{w})], \end{aligned} \tag{4.2}$$

where $f_v(v)$ is the distribution of the envelope of the voltage also known as Rice distribution (64) and $f_w(w)$ is the distribution of the detected power in the presence of a sinusoidal RFI with amplitude P. $f_v(v) = 0$ if $v < 0$. Replacing this value in the integral calculation of the expected value shows that there is a slight change in the level of the expected value due to RFI.

Our post processing technique is based on the inverse of the detected signal, therefore, the impact of RFI is insignificant and can be fully ignored. The artificial RFI is added to a snow thickness measurement signal at 2.4GHz and the amplitude of the RFI is increased from zero to 15dB external RFI source and the WiBAR still can detect the snow thickness of 64cm. The effect of measurement in the presence of all RFIs at 1GHz, 2Ghz, and 2.4GHz frequencies is included in Fig. 4.8. These RFI signals are due to GSM, cell phone, data on the cell phone, and bluetooth or Zigbee, respectively.

4.4 Impact of surface roughness

The effect of roughness in our study is twofold. It will reduce the amplitude of the delayed peak with respect to zerolag peak and it also changes the emissivity. In order to formulate these effects, we derive the coherent reflectivity and using the equation $e = 1 - |\Gamma|^2$, we can find coherent emissivity.

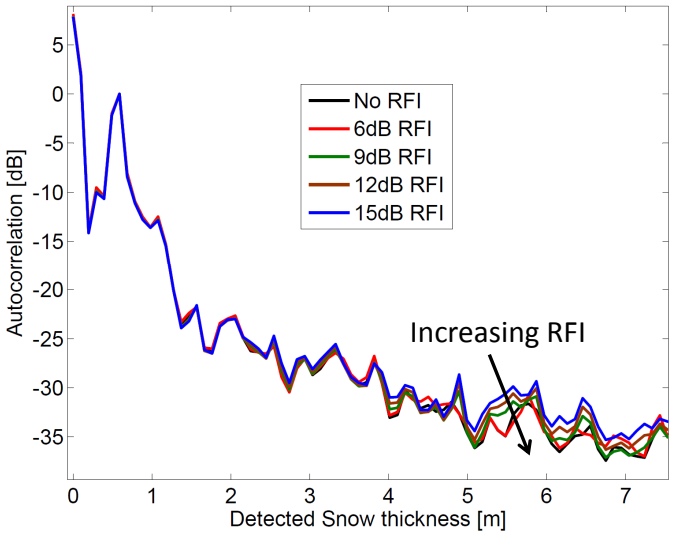

Figure 4.7: The effect of a single tone RFI on the autocorrelation response of WiBAR.

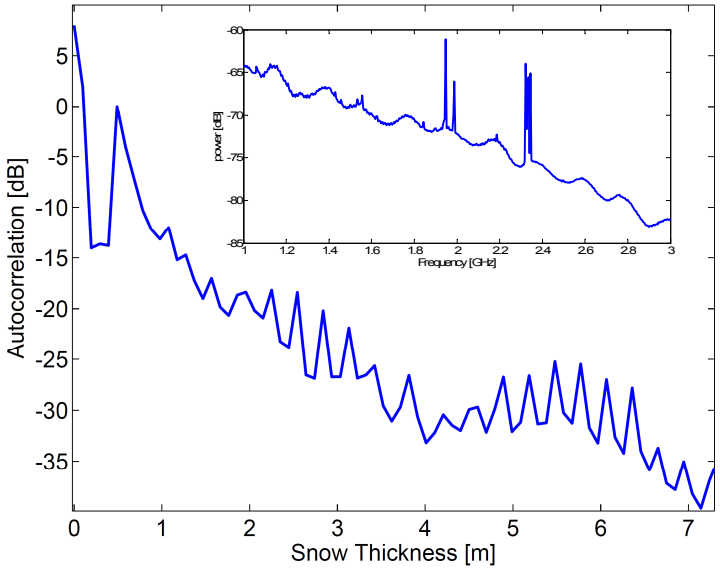

Figure 4.8: The effect of several RFIs on the autocorrelation response of WiBAR. The power spectrum is shown in the inset.

We calculate the coherent reflectivity by defining the following parameters. R_1 and T_1 are the reflection coefficient and transmission coefficients of the top interface in the absence of roughness from air into layer, R_2 is the reflection coefficient of the bottom interface in the absence of roughness from layer into underlying layer, r_1 and r_2 are the reduction in the reflection coefficient predicted by physical optics approximation for the top and bottom layers, respectively, when the wave is within the layer. t_1 is the change in the transmission coefficient due to the roughness predicted by physical optics approximation, when the wave is within the slab. x is the one way distance traveled by the wave inside the layered material. The r_1' and t_1' are the changes in the reflection of transmission coefficients due to the surface roughness, when the wave is outside the slab. The coherent reflectivity by ray tracing is given by equation 4.3.

$$\begin{aligned} \Gamma &= r_1 R_1 + t_1 t_1' T_1 T_1' R_2 r_2 e^{-j\omega\tau} \times \\ \times &\quad [\quad 1 - r_1' R_1 R_2 r_2 e^{-j\omega\tau} + r_1'^2 R_1^2 r_2^2 R_2^2 e^{-2j\omega\tau} + \cdots] \\ &= \frac{r_1 R_1 + r_2 R_2 e^{-j\omega\tau}(T_1 T_1' t_1 t_1' + r_1 r_1' R_1 R_1')}{1 + r_1' R_1 r_2 R_2 e^{-j\omega\tau}} \end{aligned} \tag{4.3}$$

where index 1 refers to air, index 2 refers to the layer sandwiched between the top and bottom interfaces. For verification, if the interface is flat, all the r_1,r_2, and t_1 are equal to 1 and due to the conservation of energy and equation (4.4) $T_1 T_1' - R_1 R_1' = 1$, $[(n_2 cos(\theta_2))/cos(\theta_1)]T = T'$, and $R_1 = -R_1'$. Therefore; the well-known reflection coefficient of a dielectric slab is inferred. The emissivity is given by equation 4.5.

$$
\begin{aligned}
T_1T_1' - R_1R_1' &= T_1T_1\frac{n_2cos(\theta_2)}{cos(\theta_1)} + R_1^2 = \\
&= 4\frac{n_1cos(\theta_1)n_2cos(\theta_2)}{n_1cos(\theta_1)+n_2cos(\theta_2)} + \frac{n_1cos(\theta_1)-n_2cos(\theta_2)}{n_1cos(\theta_1)+n_2cos(\theta_2)} \\
&= \frac{(n_1cos(\theta_1)+n_2cos(\theta_2))^2}{(n_1cos(\theta_1)+n_2cos(\theta_2))^2} = 1, \qquad (4.4)
\end{aligned}
$$

$$
\begin{aligned}
\alpha &= 1 + R_1^2r_1^2R_2^2r_2^2 - R_1^2r_1^2 - r_2^2R_2^2(T_1T_1't_1t_1' - R_1r_1R_1'r_1')^2 \\
e &= \frac{\alpha + 2cos(\omega\tau)R_1r_1R_2r_2[1-(T_1T_1't_1t_1' - R_1r_1R_1'r_1')]}{1 + r_1'^2R_1^2r_2^2R_2^2 + 2r_1'R_1r_2R_2cos(2\beta x)}, \qquad (4.5)
\end{aligned}
$$

The delayed peak will go down by a value of $10log_10(r_1'r_2)$. The value of the r_1, r_1', r_2, t_1, and t_2' can be estimated by physical optics (Kirchhoff) approximation as given by equation 4.6 (79; 75; 76; 77).

$$
\begin{aligned}
r_1^2 &= e^{-2k_0^2\sigma_1^2cos^2(\theta_1)} \\
r_1'^2 &= e^{-2k_1^2\sigma_1^2cos^2(\theta_2)} \\
r_2^2 &= e^{-2k_1^2\sigma_2^2cos^(\theta_2)} \\
t_1^2 &= e^{-(k_1cos(\theta_2)-k_0cos(\theta_1))\sigma_1^2} \\
t_1'^2 &= e^{-(k_0cos(\theta_1)-k_1cos(\theta_2))\sigma_1^2} \\
t_2^2 &= e^{-(k_2cos(\theta_3)-k_1cos(\theta_2))\sigma_2^2}, \qquad (4.6)
\end{aligned}
$$

where σ_1 and σ_2 are the rms height of the surfaces on the top and bottom, respectively. k_i is the wave vector in the region i. The Kirchohoff condition is satisfied if $kl > 6$ and $l^2 > 2.76\sigma\lambda$, where l is the correlation length of the surface and $\lambda = 2\pi/k$ is the wavelength of the propagating wave. The reduction in the peak is shown in Fig. 4.9.

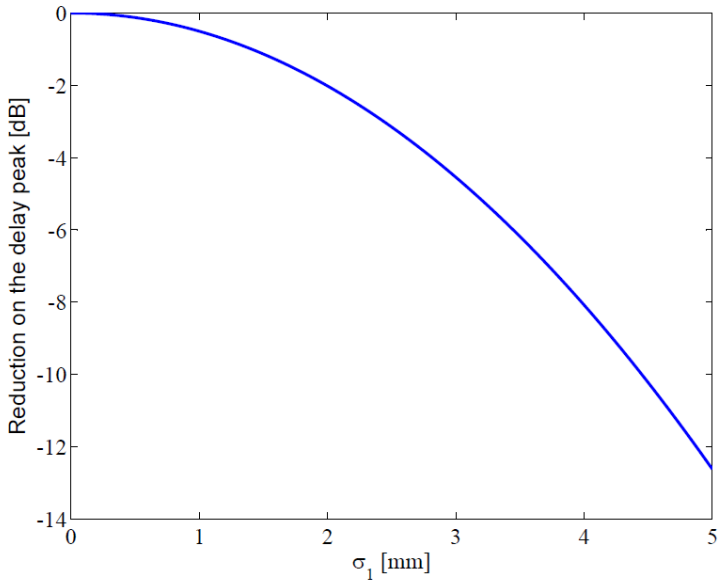

Figure 4.9: The reduction in the delay peak due to surface roughness.

4.5 Second order Effects

The antenna beamwidth affects the autocorrelation response by reducing the delayed peak slightly. The gain of the antenna is illustrated in Fig. 4.10. In order to consider this effect, we should replace the gain (G) with the ($G(f, \theta)$).

In this section the impact of the beamwidth on the autocorrelation response is analyzed. We analyze the effect of beamwidth on the time domain autocorrelation response for radiometers. Two scenarios of far- and near- field are fully investigated in this section. In the far-field case, as shown in Fig. 4.11 (a and b), the beam angle corresponds to $3dB$ bandwidth, is assumed to be θ, the antenna angle corresponds to vertical line is assumed to be α. By a simple graphical and trigonometry analysis, the following formulations are valid, as given by (4.7).

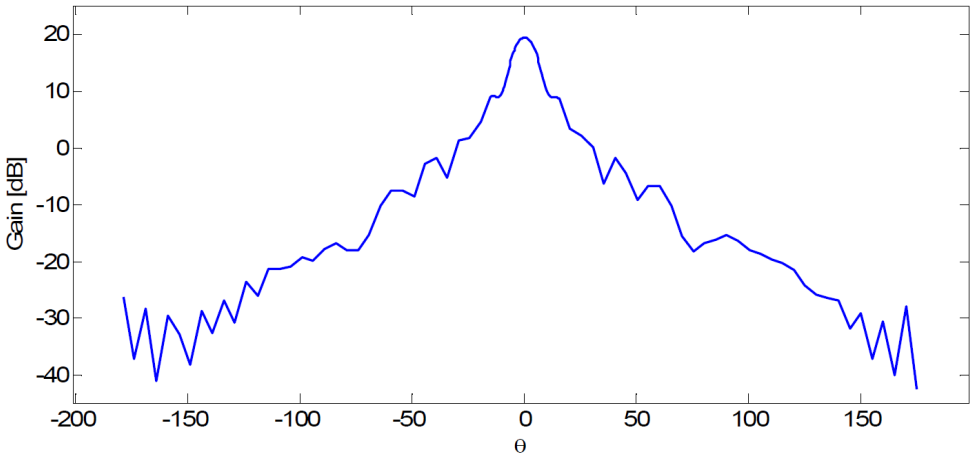

Figure 4.10: The gain pattern of the antenna as a function of angle.

$$
\begin{aligned}
sin(\alpha - \theta/2) &= nsin(\gamma_1) \\
sin(\alpha + \theta/2) &= nsin(\gamma_2) \\
tan(\gamma_1) = \frac{x_1}{d} &= \frac{sin(\alpha - \theta/2)}{\sqrt{n^2 - sin^2(\alpha - \theta/2)}} \\
tan(\gamma_2) = \frac{x_2}{d} &= \frac{sin(\alpha + \theta/2)}{\sqrt{n^2 - sin^2(\alpha + \theta/2)}} \\
x_3 = Htan(\alpha - \theta/2) &\quad , \quad x_4 = Htan(\alpha + \theta/2) \\
b = Htan(\theta/2) &\quad , \quad a = d\frac{sin(\theta/2)}{\sqrt{n^2 - sin^2(\theta/2)}} \\
Direct\ path\ diameter_x &= x_4 - x_3 - x_1 + x_2 \\
Delayed\ path\ diameter_x &= x_4 - x_3 - 3x_1 + 3x_2 \\
Common\ diameter_x &= x_2 + x_4 - x_3 - 3x_1 \\
Direct\ path\ diameter_y &= b + 2a \\
Delayed\ path\ diameter_y &= b + 6a
\end{aligned}
\tag{4.7}
$$

In the near field case, the same approach leads to the same equation as the one

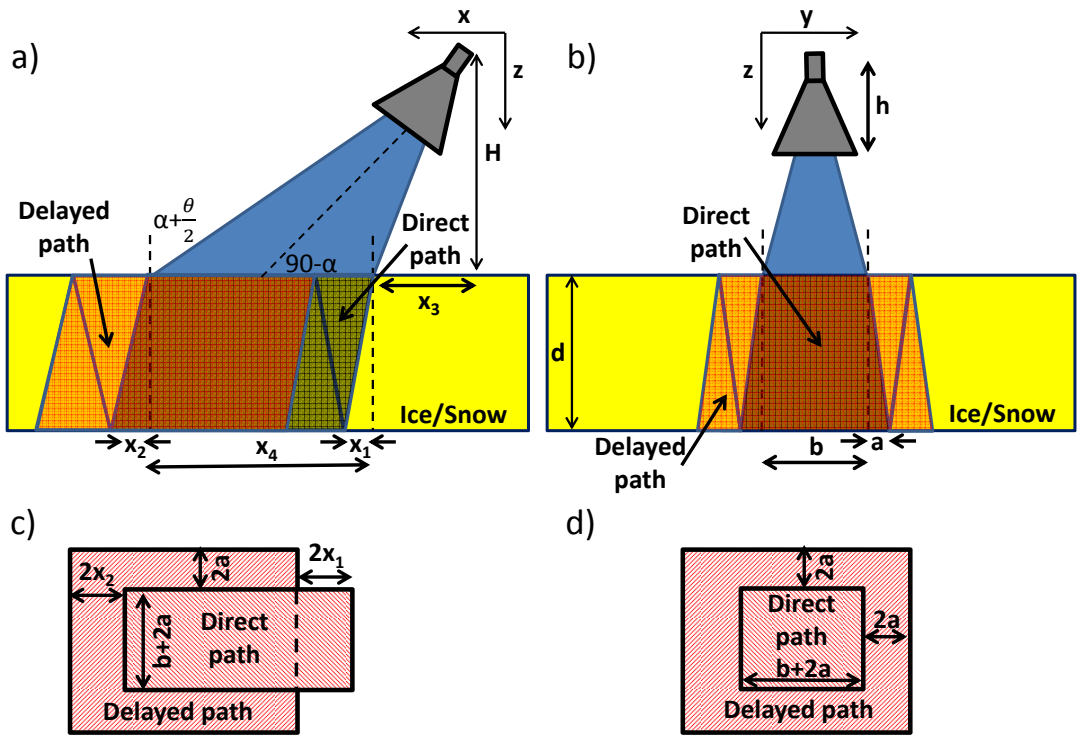

Figure 4.11: The effect of beamwidth on the WiBAR response. (a) Far-field scenario in x-z plane. (b) Far-field scenario in y-z plane. The near field scenario is very similar to figure (b). The direct path and delayed path areas for (c) far-field and (d) near-field measurements are shown.

for far-field in the y-direction, with the only exception of replacing h instead of H. In case of very far-field, where we can assume parallel beams, $x_1 = x_2$ and $\theta = 0$.

The impact of non-parallel interfaces in the layered medium consists of ice/snow on the autocorrelation response is the broadening of the peaks. In order to show this phenomenon, a through analysis is investigated. The geometry of the problem is shown in Fig. 5.1. The Greek letters show the angles. The incident angle of the antenna is α. The deviation from the parallel interface is parametrized by α_1. The θ_1 and θ_2 are the angles of emission for one dipole of the underlying medium. We are interested in the case, in which the waves can propagate in parallel toward the antenna at the far field. Therefore; $\theta_2 = \theta_1 - 2\alpha_1$. The angles should be smaller than the critical angle to make sure that the transmission of the emission wave toward

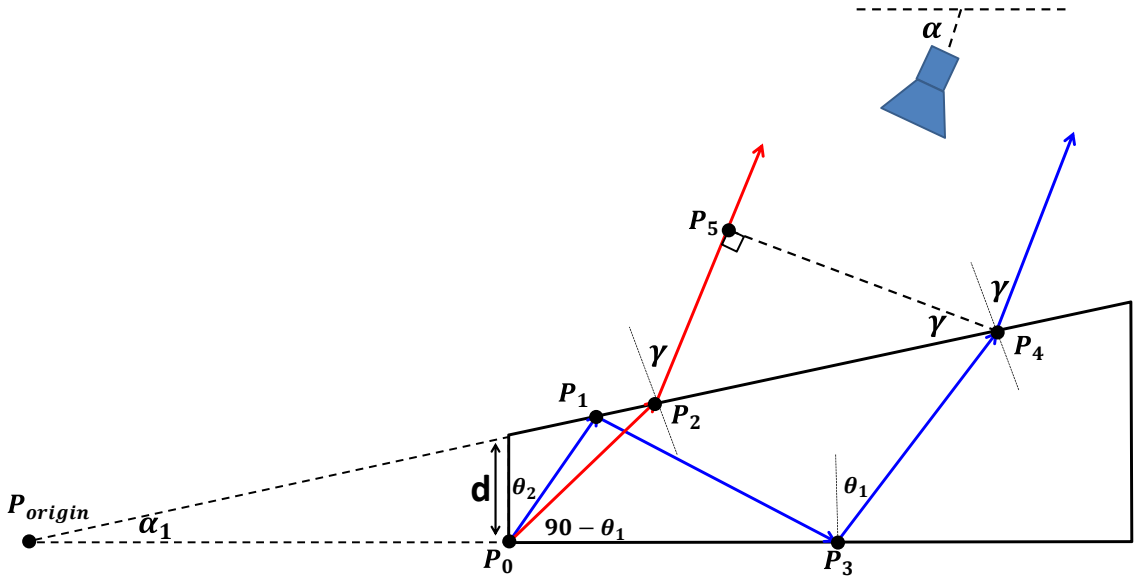

Figure 4.12: The non-parallel interfaces and the geometrical ray tracing of the emission waves.

the antenna is not zero. Therefore; $\theta_1 + \alpha_1 < \theta_c$, where $sin(\theta_c) = 1/n$ and n is the refractive index of the layered medium. Based on the Snell's law there is only one ray at each point that can reach to the antenna. Therefore, $nsin(\theta_1 + \alpha_1) = sin(\gamma)$. The incident angle of the antenna is related to the other angles as $\alpha = 90 - (\gamma - \alpha_1)$.

We analyze the problem by finding the coordinate of the points $(P_0, P_1, P_2, P_3, P_4, P_5)$. P_{origin} is assumed to be $(0, 0)$. the coordination of P_0 can be calculated simply as $(\frac{d}{tan(\alpha_1)}, 0)$. The coordinate of the points P_1 and P_2 can be calculated by finding the intersection of two lines of $y = cotg(\theta_i)(x - dcotg(\alpha_1))$ and $y = tan(\alpha_1)x$, where $i = 1, 2$. The coordinate of the points P_1 and P_2 are given by (4.8).

$$
\begin{aligned}
x_1 &= \frac{dcotg(\theta_2)cotg(\alpha_1)}{cotg(\theta_2) - tan(\alpha_1)} \\
y_1 &= tan(\alpha_1)x_1 \\
x_2 &= \frac{dcotg(\theta_1)cotg(\alpha_1)}{cotg(\theta_1) - tan(\alpha_1)} \\
y_2 &= tan(\alpha_1)x_2
\end{aligned} \tag{4.8}
$$

The coordination of P_3 can be calculated as given by (4.9).

$$
\begin{aligned}
x_3 &= x_2 + y_2 tan(\theta_1) \\
y_3 &= 0.
\end{aligned} \tag{4.9}
$$

the coordination of P_4 is calculated using the same procedure used to calculate the coordination of the P_1 and P_2 points. Therefore, the coordination is given by (4.10).

$$
\begin{aligned}
x_4 &= \frac{x_3 cotg(\theta_1)}{cotg(\theta_1) - tan(\alpha_1)} \\
y_4 &= tan(\alpha_1)x_4.
\end{aligned} \tag{4.10}
$$

The distance between the P_5 and P_1 is calculated using trigonometry as given by (4.11).

$$
||P_5 - P_2|| = sin(\gamma)||P_4 - P_2||, \tag{4.11}
$$

where $||p - q||$ is the norm of the $p - q$ is equal to the distance between the points p

and q.

The delay is formulated as given by (4.12).

$$\tau = \frac{||P_1 - P_0||n}{c} + \frac{||P_1 - P_3||n}{c} + \frac{||P_3 - P_4||n}{c} - \frac{||P_2 - P_0||}{c} + \frac{||P_2 - P_5||}{c}, \quad (4.12)$$

The algorithm to find the broadening of the autocorrelation peak is given as follows. Using the incident angle of the antenna and the slope of the interface of the layered medium, γ, then θ_1 and θ_2 can be calculated. Then, the coordination of the points can be calculated and consequently the delay can be calculated. The procedure is repeated for all the angles within the beam-width of the antenna. The difference between the maximum and minimum delay time show the broadening of the autocorrelation peak.

4.6 Compressive sensing

The ever increasing amount of data transmitted by mobile devices has posed significant challenges to the specifications of mobile transmitters and receivers. One of the most important bottlenecks in such devices has become the analog to digital converter (ADC). This is due to the fact that the performance of ADC has not scaled with the advances in the signal reception and processing units. On the other hand, most of the mobile signals are inherently sparse. Hence, such sparse signal is usually compressed as soon as it is in the digital domain. In other words, many of the acquired samples are redundant and hence will be discarded as soon as the signal is in the digital domain. For example, images are sparse in wavelet domain, speech is sparse in frequency domain, etc. One way to overcome the limitations of the current signal reception technology is to utilize this inherent sparsity of the signals so as to acquire significantly smaller number of samples from a continuous-time signal in the analog-to-digital conversion. Compressive sensing (CS) provides a novel theory of

sampling (as opposed to the traditional Nyquist-rate sampling) that aims to remove the inherent redundancy of the signal while acquiring samples. In other words, it tries to acquire as many samples as required to represent the sparse signal as opposed to sampling at the Nyquist rate and then discarding the redundant part. Compressive sensing has recently attracted a great deal of interest because of the rising of low complexity signal reconstruction algorithms that enable real-time signal acquisition. One important advantage of the compressive sensing technique is that it can directly extract information from the input desired signal and hence it is sometimes referred to as analog-to-information conversion. In most analog and digital systems, we deal with a huge set of redundant data that can be compressed with signal processing methods without removing significant information. Compressive sensing technique has already been used in a lot of applications including: image processing, data processing, and object classifications.

In the analog design world, different implementations of the compressive sensing algorithm has been introduced such as random demodulation (63), random sampling (59), and random filtering, all of which are based on the same CS principle. Among these systems, random demodulation technique has shown a great potential for future communication systems. This configuration can be utilized in the transmitter design such as sensor nodes in a wireless sensor network or it can be used in the receiver architecture to reduce the complexity and power consumption of the receiver. In the receiver design, which is the focus of this report, this configuration can reduce the burden of the analog to digital converters (ADCs) as well as reducing the overall power consumption of the system. Compressive sensing (CS) is a compression technique that can be utilized for sparse signals recovery. A sparse signal can be defined as any signal that can be expressed by a small number of components. As an example a sinusoidal signal is sparse in frequency domain. The CS algorithm relies on the multiplication of the input sparse signal by a random matrix known

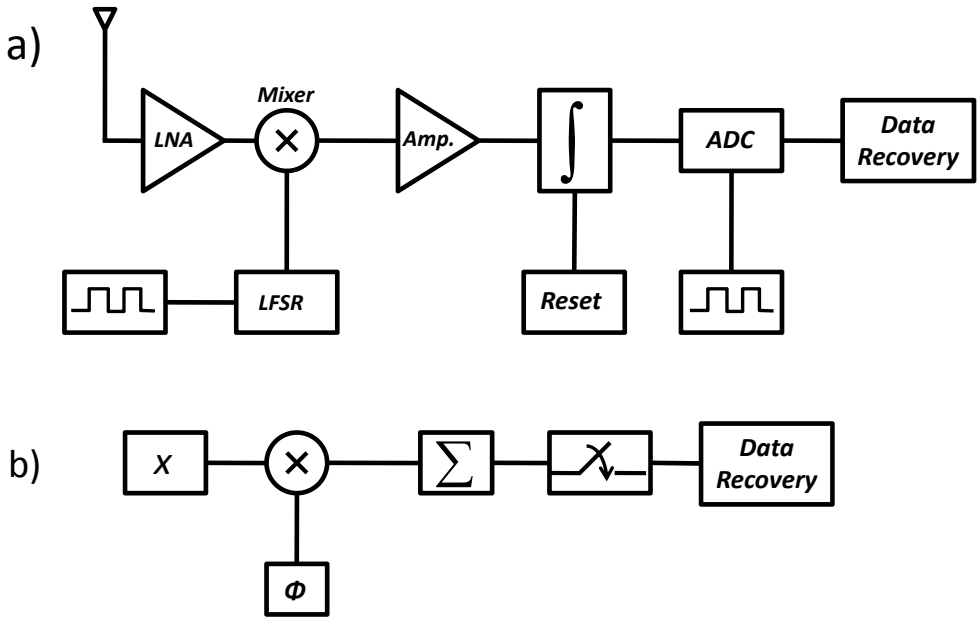

Figure 4.13: System level configuration of (a) superheterodyne compressive sensing receiver and (b) mathematic modeling of the compressive sensing based receiver's topology.

as random measurement matrix. The number of measurements should be less than the whole number of data points (Nyquist rate). Adding the measurement data can generate a single output data for each measurement. By sending the single data for each measurement, CS algorithm can recover the original data.

Our radiometer is mainly a superheterodyne configuration. It composed of a pre amplification stage using a very low noise amplifier followed by a gain stage, down conversion mixer, intermediate frequency (IF) filter, and ADC. A superheterodyne receiver can be interpreted as a random demodulation system by replacing the multiplication by mixing, local oscillator with a random number generator, and the summation operator by integrator/low pass filter. The overall system block diagram for a superheterodyne receiver is shown in Fig. 4.13. The input RF signal incident to the antenna is the input of the system. This signal is amplified using a narrow-

band low noise amplifier (LNA). The amplified signal is then inserted to the mixer and is multiplied with a random number string. The mixed signal passes through a low pass filter/integrator and the output data is digitally sampled with a low rate ADC. The sampled data is processed in the processing unit. In our implementation, we utilized a two different algorithms to recover the input signal. This stage can also be implemented on a DSP board to make a real-time analysis and recovery of the data. In random demodulation system design, the input signal is mixed with a pseudo-random bipolar wave sequence using an analog multiplier to randomize the signal in time domain. This is followed by a Gm-C based differential integrator that adds the random samples and produces the measurements. The reconstruction end consists of a communication module, to receive the compressed signal, as well as a digital signal processor (DSP) that runs the reconstruction algorithm and recovers the original signal from the compressive measurements.

This algorithm/prototype has been implemented previously in [randemod] by the author and was capable of testing the AIC performance for signals with bandwidth up to 1MHz. Single tone signals are successfully reconstructed when sampled at a Nyquist-rate/8 sampling rate while maintaining a 55.7 dB signal-to-noise ratio, which represents a 9.3 bit resolution. Sampling at Nyquist-rate/8 represents about 87.5% savings in bandwidth and memory. Using Nyquist-rate/12 sampling frequency while achieving a 39.6 dB signal-to-noise ratio the savings in bandwidth and memory was 91.7%. The author showed that this implementation is capable of detecting single tone sine waves and AM-modulated sine waves.

In our system, the autocorrelation response as well as the Fourier transform of the received power spectrum are sparse. The sparsity of the Fourier transform of the power spectrum is addressed here using random demodulation technique and in the future work the sparsity in the autocorrelation domain is addressed using random sampling technique.

Mathematically, the reconstruction using compressive sensing is given by the solution to the optimization problem given by equation 4.13.

$$\begin{aligned} \underset{x}{\text{minimize}} \quad & \|x\|_{l1} \\ \text{subject to} \quad & Ax = b, \end{aligned} \tag{4.13}$$

where $\|\cdots\|_{l1}$ denotes the $l1$ norm. The measurement matrix can be written as Ax, where x is sparse. There are several algorithms to solve this equation. The most common ones are orthogonal matching pursuit (OMP) and approximate message passing (AMP). OMP relies on finding the best matching projections of the minimum orthogonal multidimensional basis over a complete dictionary. This basis has the minimum number of dimensions and the projection of data on this coordinate system represent data almost completely. The algorithm relies on finding the basis vectors one by one. The result of OMP applied to a snow thickness scenario is shown in Fig. 4.14. AMP is an iterative technique that can find the solution to the compressive sensing optimization problem, efficiently. The result of AMP applied to a snow thickness scenario is shown in Fig. 4.15.

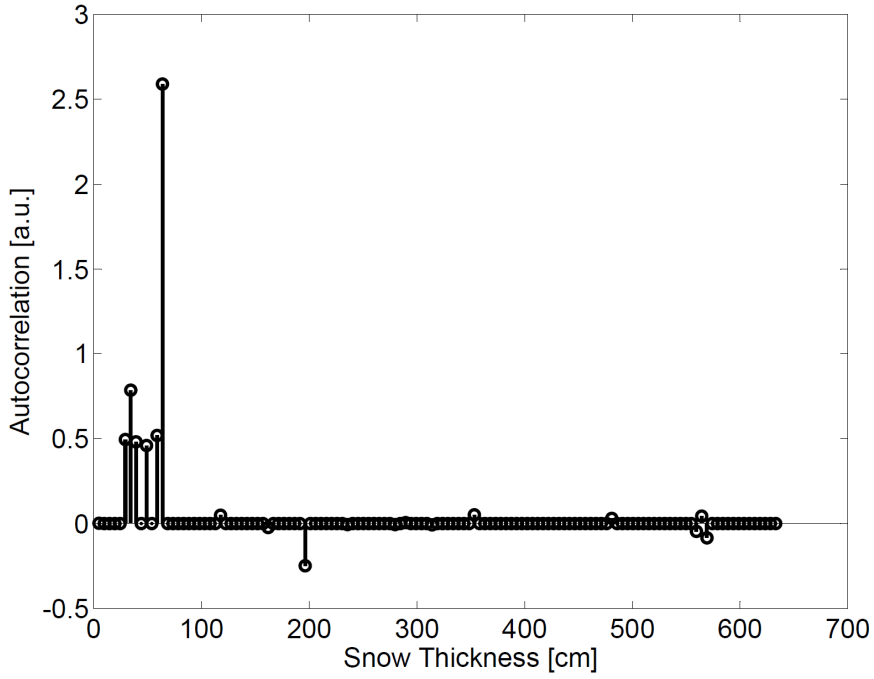

Figure 4.14: Autocorrelation sparse signal recovery using orthogonal matching pursuit, which predicts 64cm of snow correctly.

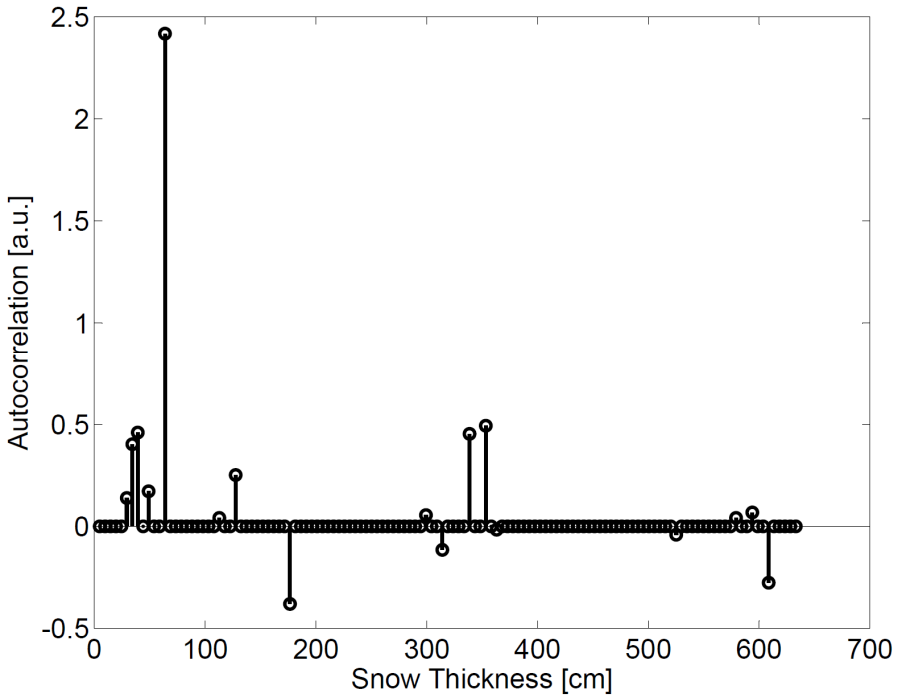

Figure 4.15: Autocorrelation sparse signal recovery using approximate message passing, which predicts 64cm of snow correctly.

CHAPTER V

Autocorrelation-Based Technique to Measure the Noise Figure of Wideband Systems

5.1 Introduction

Empirical techniques to measure the noise figure (NF) of wideband systems are challenging, specially at high frequencies. The common procedure to characterize the noise figure of a two port device is by utilizing a high-gain, tunable, sensitive double-conversion super-heterodyne receiver with tunable attenuators followed by a square law power detector (13; 40). In this procedure a couple of calibrated noise sources (28; 36; 37) can be used as input to the device under test (DUT). The amplified noise enters the tunable receiver and the power can be detected by the power detector. This procedure is capable of characterizing the gain and noise figure of the DUT. The variable attenuators are used to make sure that the output power is within the detection range of square-law detector. The noise sources can be two matched loads at very different physical temperatures. The power of the noise generated by matched load as a function of their temperatures can be formulated as kTB, where k is the Boltzmann constant, B is the bandwidth, and T is the physical temperature of the load. In this procedure the ratio of the detected power for the matched loads ($Y = P_1/P_0$) is used to find the noise figure of the DUT, where P_0 and P_1 are the

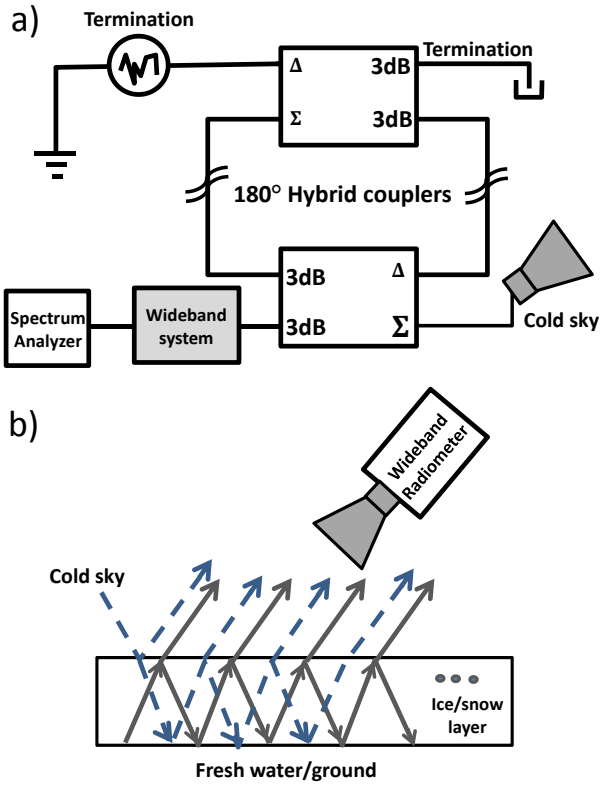

Figure 5.1: (a) Microwave circuit schematic for noise figure measurement. (b) The circuit in (a) is inspired by the detection of emission from a layered media.

output noise power of the cold and hot loads, respectively. Commonly the hot and cold loads are realized using calibrated active noise sources. These noise sources generate noise in both ON and OFF states. They are characterized by a quantity known as excess noise ratio (ENR) defined by $ENR = (T_1 - T_0)/T_0$, where T_0 and T_1 are the noise temperature for the OFF and ON conditions of the active noise source. T_0 is usually the ambient temperature. T_1 is usually one to three orders of magnitudes larger than T_0, therefore, ENR is between 10 to $30dB$.

Noise figure estimation of radiometers is required to find the sensitivity and precision of the radiometers. The common procedure to find the noise figure of the radiometers is by linear extrapolation of cold sky and hot absorber (78). The hot absorber temperature can be sensed accurately, however determining the cold sky temperature can't be estimated precisely. The estimation of the sidelobe contribu-

tions are also challenging. The detected sky temperature is a function of frequency and the incidence angle of the radiometer looking at sky. Hence the estimated noise figure depends on the cold sky temperature. In the microwave frequency range of WiBAR, the cold sky temperature is within $3 - 10K$. The inaccuracy in fiding the cold sky temperature directly influences the estimated noise figure of the radiometers. Estimation of the noise figure is by extrapolating the calibration line of the radiometer and finding the negative temperature, at which the radiometer output appears to detect zero power (69). The receiver temperature, T_{REC}, corresponds to the absolute value of that temperature. The noise figure depends on the receiver temperature as given by $NF = \frac{T_{REC}}{T_0} + 1$, where T_0 is the ambient temperature and NF is the noise figure, respectively.

In this paper, a novel procedure to estimate the noise figure (NF) information of wideband systems, such as amplifiers, receivers, and radiometers is presented. This procedure relies on the calculation of the autocorrelation response of the setup illustrated in Fig. 5.1(a). This setup is inspired by the multiple reflections inside a layered medium (ice layer) as shown in Fig. 5.1(b)[2,3]. Analysis of the autocorrelation response reveals information about the microwave transit time within the ice layer and consequently the thickness of the ice layer. Fig. 5.1(a) is the microwave circuit model for the scenario shown in Fig. 5.1(b). The actual experimental setup is shown in Fig. 5.2.

This chapter is organized as follows. In Section 5.2, the motivation and the procedure to find the noise figure is explained. In Section 5.3, a thorough theoretical analysis of the setup is explained in details. The experimental results are demonstrated in Section **??**. Section 5.5 concludes the chapter.

5.2 Analysis of the system response

This idea is based on our observation in the measurement of the brightness temperature of the emitting background beneath a layered medium using passive remote sensing. The multiple reflections inside the layered medium causes the same emitting wave to travel to the radiometer with different transit time delays, which are a function of the thickness of the layered medium (23; 22). The detected power spectral density shows periodic behavior called ripples. The periodicity of the ripples is directly proportional to the thickness of the layer. Based on Wiener-Khinchin theorem, the autocorrelation response can be extracted by calculating the inverse Fourier transform of power spectral density. The autocorrelation response of the brightness temperature demonstrates peaks. The zero-lag peak, first, and second peaks are stronger than the other peaks. The first and second delay waves transit the same path with similar reflection coefficient and absorption, which accounts for an equal value of attenuation for both paths. Hence, if we measure the amplitude of the zero-lag peak (A_0), first peak (A_1), and second peak (A_2) in dB and check the difference between $A_0 - A_1$ and $A_1 - A_2$ with an ideal noiseless radiometer, we expect to see the same number. However, these values are different. The difference is due to the noise figure of the radiometer, which is only present in the zero-lag peak.

The detected voltage in the input of the radiometer can be formulated as given by (5.1).

$$v(t) = v_{dir}(t) + v_{delay1}(t) + v_{delay2}(t) + v_{nf}(t), \tag{5.1}$$

where $v_{dir}(t)$, $v_{delayi}(t)$ with $i = 1, 2$ are the thermal emission of the underlying medium or downwelling brightness temperature reaching to the wideband radiometer directly and with delays, respectively. $v_{delay1}(t)$, and $v_{delay2}(t)$ corresponds to the first and second peaks, respectively. In these formulations only the first and second delayed waves are considered for simplicity. We also assume that the layered medium

Figure 5.2: The actual implementation of the loop structure to measure the noise figure of the WiBAR.

is lossless for simplicity. The delayed waves are related to the direct path wave by $v_{delay1}(t) = \rho_1\rho_2 v_{dir}(t-\tau_d)$ and $v_{delay2}(t) = \rho_1^2\rho_2^2 v_{dir}(t-2\tau_d)$, where ρ_i is the reflection coefficients on the top ($i=1$) and bottom ($i=2$) interfaces of the layer, respectively. τ_d is the microwave transit time delay between the direct path and doubly reflected path waves. $v_{nf}(t)$ is the noise contribution of the receiver referred to the input of the radiometer. The WiBAR detects the autocorrelation response of the power spectral density, which corresponds to finding the autocorrelation as given by 5.2. In this formulation, the input referred noise of the receiver is independent (uncorrelated) of the brightness temperature of the background. Therefore, the average of the cross terms are zero. The correlation length of each of the noise terms also is assumed to approach to zero (66), which is much smaller value than τ_d.

$$\begin{aligned} &< v(t)v^*(t+\tau) >= \\ &< v_{nf}(t)v_{nf}(t+\tau) > + f(v_{dir}^{sky}(t')) + g(v_{dir}^{under}(t'')), \end{aligned} \tag{5.2}$$

where$f(v_{dir}^{sky}(t'))$ and $g(v_{dir}^{under}(t''))$ are only a function of the brightness temperature of sky and the underlying medium, respectively. These terms are independent of the input referred noise of the receiver. The term $< (v_{nf}(t)v_{nf}(t+\tau)) >$ has its maximum at $\tau = 0$ and it decays very fast, which indicates that the receiver noise is only presented at zero lag peak and it is absent in the first and second peaks. The other two terms are presented in the zero lag, first and second peaks.

We have designed and implemented a microwave circuit, shown in Fig. 5.1(a), that mimics the physics behind the scenario shown in Fig. 5.1 (b). This circuit consists of two 180 degree hybrid couplers that divide the input signal into two output signals with a phase difference of 180 degree. Any of these couplers model one of the interfaces and the 180 degree out of phase signals are similar to the transmitted and reflected signals from the interface. The spectrum analyzer is used as a spectral power density sensor. The actual measurement setup is shown in Fig. 5.2. In order to calibrate the measured data, the left branch of the loop in Fig. 5.1(a) is broken and terminated by matched load terminations. The measured data is used for calibration of the main data. Both the calibration and measured data are shown in Fig. 5.4(a). The inverse Fourier transform of the calibrated data is shown in Fig. 5.4(b). The zero-lag peak as well as first, second, third, fourth and fifth peaks are vivid in Fig. 5.4 (b).

As shown before, the noise figure of the radiometer is only presented in the zero-lag peak. Therefore, analyzing the autocorrelation response of the received brightness temperature provides enough information to estimate the noise figure of the wideband system of interest for better performance and higher sensitivity.

5.3 Theoretical model for noise figure estimation

We have derived a closed-form formulation for the noise figure of a wideband system using the setup shown in Fig.5.1 (a). The downwelling brightness temperature of sky is assumed to be independent and uncorrelated from the brightness temperature

of the background medium. Both of these signals are also independent of the system noise.

The overall input voltage of the wideband system is equal to $V_i = V_{rw} + V_{rs} + V_n$, where V_n is the wideband system noise referred to the input. The V_{rs} and V_{rw} are the received voltage in the input of the wideband system corresponding to the sky and matched load, respectively. The noise at the input of the wideband system can be derived as given by (5.3).

$$\begin{aligned} V_{rw} &= (V_w\alpha^2 e^{-i\beta l} - V_w\alpha^4 e^{-3i\beta l} + ...) \\ &= \frac{V_w\alpha^2 e^{-i\beta l}}{1+\alpha^2 e^{-2i\beta l}}, \\ V_{rs} &= (V_s\alpha + V_s\alpha^3 e^{-2i\beta l} - V_s\alpha^5 e^{-4i\beta l} + ...) \\ &= \frac{V_s\alpha(1+2\alpha^2 e^{-2i\beta l})}{1+\alpha^2 e^{-2i\beta l}}, \end{aligned} \tag{5.3}$$

where α is the overall attenuation of the input signal while passing through hybrid coupler as well as the cable loss. It is assumed the same for both terminals of the coupler due to the symmetry of the structure. V_s and V_w are the noise waves of the sky and matching load used for termination, respectively. The envelope of the power spectral density is given by equation (5.4).

$$P_i =< |V_i|^2 >=< |V_{rw}|^2 > + < |V_{rs}|^2 > + < |V_n|^2 >= P_w + P_s + P_n, \tag{5.4}$$

where $P_k =< |V_k|^2 >$ for $k = i, w, s, n$. By inserting (5.3) into equation 5.4, the envelope of the power spectral density can be given by (5.5).

$$P_i = P_n + \frac{\alpha^4 P_w + \alpha^2 P_s[1 + 4\alpha^4 + 4\alpha^2 cos(4\pi f\tau)]}{1 + \alpha^4 + 2\alpha^2 cos(4\pi f\tau)}, \tag{5.5}$$

where τ is the time delay corresponds to the length of the cable and can be calculated using $\beta l = 2\pi f\tau$. The power spectral density at the output of the wideband system is given by $P_o = |H(s)|^2 P_i$, where P_i and P_o are the power at the output and the input of the wideband system. $H(s)$ is the impulse response of the wideband system in the Laplace domain. For simplicity, we assume that the gain of the system is flat top normalized to one and is within the bandwidth of the system. The autocorrelation response can be calculated by applying an inverse Fourier transform on the power spectral density and is given by (5.6).

$$\begin{aligned} R \quad (t) &= \int_0^\infty P_o e^{-i2\pi ft} df = R_n(t) + R_w(t) + R_s(t) \\ &= \int_{f_l}^{f_h} P_n e^{-i2\pi ft} df \\ &+ \int_{f_l}^{f_h} \frac{P_w \alpha^4 e^{-i2\pi ft}}{1 + \alpha^4 + 2\alpha^2 cos(4\pi f\tau)} df \\ &+ \int_{f_l}^{f_h} \frac{P_s \alpha^2 [1 + 4\alpha^4 + 4\alpha^2 cos(4\pi f\tau)] e^{-i2\pi ft}}{1 + \alpha^4 + 2\alpha^2 cos(4\pi f\tau)} df. \end{aligned} \tag{5.6}$$

We assume white noise for all three components of the input voltage. The integral should be evaluated at time stamps of 0, τ, and 2τ. The contribution of the wideband system noise is given in (5.7).

$$R_n(t) = P_n B e^{-i\omega_c t} Sinc(\pi Bt), \tag{5.7}$$

where $B = f_h - f_l$ and ω_c are the bandwidth and angular center frequency of the wideband system. The sinc function is defined as $Sinc(x) = sin(x)/x$. $P_n = kT_{rec}$, where k is the Boltzmann constant and T_{rec} is the temperature of the receiver. The contribution of the noise generated by the matching load is given by (5.8).

$$R_w(t) = \frac{P_w \alpha^4}{i4\pi\tau} \int_{u_l}^{u_h} \frac{u^{\frac{-t}{2\tau}} du}{\alpha^2 u^2 + (1+\alpha^4)u + \alpha^2}, \tag{5.8}$$

where $u = e^{i4\pi f\tau}$ is a dummy variable. The denominator of the integrand can be written as $(u - \gamma_1)(u - \gamma_2)$, where γ_1 and γ_2 are given by (5.9).

$$\begin{aligned} \gamma_1 &= \frac{-(1+\alpha^2)^2}{2\alpha^2} \\ \gamma_2 &= \frac{-(1-\alpha^2)^2}{2\alpha^2} \end{aligned} \tag{5.9}$$

Based on the values of α, which is confined between 0 and 1, $\gamma_1 < -2$ and $-1/2 < \gamma_2 < 0$. Therefore, both of them are negative, the γ_1 pole is outside the unit circle and γ_2 pole is inside the unit circle. The integral is in the complex domain and using the Cauchy integral theorem for analytical functions the integral can be calculated at $t = 0$ using a unit circle contour as given by (5.10).

$$R_w(0) = \frac{P_w \alpha^4 B}{|\gamma_1| - |\gamma_2|}, \tag{5.10}$$

where $P_w = kT_w$ and T_w is the ambient temperature. The system bandwidth appears in (5.10) due to the number of the rotation on the contour. At $t = \tau$, the contour is shown in Fig. 5.3. The contribution of the matching load in the autocorrelation integral is given by (5.11)

$$R_w(\tau) = \frac{P_w \alpha^4}{i4\pi\tau(|\gamma_1| - |\gamma_2|)} \left[\int_R \frac{u^{-1/2} du}{u + |\gamma_2|} - \int_R \frac{u^{-1/2} du}{u + |\gamma_1|} \right]. \tag{5.11}$$

Each of the contour integrals can be broken into four integrals as given by (5.12).

$$\oint \frac{u^{-1/2}du}{u+|\gamma|} = \int\limits_{r+R+r_1+r_2} \frac{u^{-1/2}du}{u+|\gamma|}, \tag{5.12}$$

where γ can be the first or the second pole. Using Cauchy theorem, the contour integral can be calculated as given by (5.13).

$$\oint \frac{u^{-1/2}du}{u+|\gamma|} = \begin{cases} 0 & \text{if } \gamma = |\gamma_1| \\ 4\pi i B\tau |\gamma_2|^{-1/2} e^{-i\pi/2} & \text{if } \gamma = |\gamma_2| \end{cases} \tag{5.13}$$

In order to find the integral on the outer contour R, we should calculate the integrals over all three contours r, r_1, r_2. The integral over the inner contour is zero as the radius of the contour approaches zero as given by (5.14).

$$\begin{aligned} \int\limits_{r} \frac{u^{-1/2}du}{u+|\gamma|} &= ir \int\limits_{2\pi}^{0} \frac{r^{-1/2}e^{i\theta/2}d\theta}{\gamma + re^{i\theta}} \\ \Rightarrow |\int\limits_{r} \frac{u^{-1/2}du}{u+|\gamma|}| &\leq \frac{2\pi r^{1/2}}{|\gamma|-r} \rightarrow\ 0 \ as\ r \rightarrow 0, \end{aligned} \tag{5.14}$$

where $u = re^{i\theta}$. The other two integrals can be calculated as given by (5.15).

$$\begin{aligned} \int\limits_{r_1+r_2} \frac{u^{-1/2}du}{u+|\gamma|} &= 2ie^{-i\pi/2} sin(\pi/2) \int\limits_{0}^{1} \frac{x^{-1/2}dx}{x+|\gamma|} \\ &= \frac{2iLn[\frac{\sqrt{|\gamma|}-i}{\sqrt{|\gamma|}+i}]}{\sqrt{|\gamma|}}, \end{aligned} \tag{5.15}$$

where Ln is the natural logarithmic function. The integral over the outer contour can be calculated as given by (5.16).

$$\int_R \frac{u^{-1/2}du}{u+|\gamma_2|} - \int_R \frac{u^{-1/2}du}{u+|\gamma_1|} = \frac{4\pi B\tau|\gamma_2|^{-1/2}}{|\gamma_1|-|\gamma_2|} + \frac{-2i}{|\gamma_1|-|\gamma_2|}\left[\frac{Ln[\frac{\sqrt{|\gamma_2|}-i}{\sqrt{|\gamma_2|}+i}]}{\sqrt{|\gamma_2|}} - \frac{Ln[\frac{\sqrt{|\gamma_1|}-i}{\sqrt{|\gamma_1|}+i}]}{\sqrt{|\gamma_1|}}\right], \tag{5.16}$$

At $t = 2\tau$, the integral is simplified and can easily be calculated as given by (5.17).

$$R_w(2\tau) = \frac{P_w B\alpha^4}{|\gamma_1|(|\gamma_1|-|\gamma_2|)} \tag{5.17}$$

The same procedure can be applied to the sky contribution in the autocorrelation calculation as derived in (5.18).

$$R_s(t) = \frac{\alpha^2 P_s}{i4\pi\tau}\int u^{-t/(2\tau)}\left[\frac{A_1}{u} + \frac{B_1}{u-\gamma_1} + \frac{C_1}{u-\gamma_2}\right]du, \tag{5.18}$$

where $P_s = kT_s$, $A_1 = 2\alpha^2/(\gamma_1\gamma_2)$, $B_1 = D_1/(\gamma_1-\gamma_2)$, $C_1 = 2\alpha^2 - A_1 - B_1$, and $D_1 = 2\alpha^2\gamma_1(1-1/(\gamma_1\gamma_2)) + 1 + 4\alpha^4 + A_1(\gamma_1+\gamma_2)$. Using the same procedure and the same contours, the integrals can be calculated and the solutions are given by (5.19).

$$\begin{aligned} R_s(0) &= P_s\alpha^2 B(A_1+C_1) \\ R_s(\tau) &= \frac{P_s\alpha^2}{2\pi\tau}\left[\frac{-B_1 Ln[\frac{\sqrt{|\gamma_1|}-i}{\sqrt{|\gamma_1|}+i}]}{\sqrt{|\gamma_1|}} - \frac{C_1 Ln[\frac{\sqrt{|\gamma_2|}-i}{\sqrt{|\gamma_2|}+i}]}{\sqrt{|\gamma_2|}}\right] \\ &- C_1 P_s\alpha^2 iB|\gamma_2|^{-1/2} \\ R_s(2\tau) &= P_s\alpha^2 B(-B_1/\gamma_1), \end{aligned} \tag{5.19}$$

5.4 Noise figure estimation and verification

We have built a wideband radiometer at the frequency range of $7-10GHz$ and is composed of two gain stages, low noise amplifiers (LNAs), a band pass filter (BPF). The isolators and the attenuators are used for providing wideband matching among adjacent stages. The wideband impedance matching is required to remove the internal oscillation in the structure due to the instability of the LNAs and increase the dynamic range of the radiometer. In order to stabilize the chain of high gain amplifiers and make sure that they both operate on their linear gain regime, we add an attenuator in between the amplifiers.

The noise figure of the radiometer can be calculated theoretically using the Friis' formula (24). Only the dominant terms should be considered in noise figure calculation. The dominant contribution to the noise figure is due to the first LNA in the chain. The noise contribution of other components is negligible. The overall noise figure of our wideband radiometer is found to be $2.46dB$ in the frequency band of interest $(7-10GHz)$. As given by (5.20), only the dominant terms have been considered in noise figure calculation.

$$\begin{aligned} F &= F_{SemiRigid} + \frac{F_{Isolator}-1}{G_{SemiRigid}} + \\ &+ \frac{F_{LNA1}-1}{G_{SemiRigid}\times G_{Isolator}} + \\ &+ \frac{F_{Attenuator}-1}{G_{SemiRigid}\times G_{Isolator}\times G_{LNA1}\times G_{BPF}}, \end{aligned} \tag{5.20}$$

where F is the noise figure of the overall radiometer. $F_{SemiRigid}$ is the noise figure associated with the semi rigid cable connected right after the antenna. We have fully characterized this semi-rigid cable using a network analyzer and its loss is equal to $0.05dB$ in the frequency range of interest $(7-10GHz)$. Using $T_0 = T_p$, where T_p is

the physical temperature of the component and T_0 is the ambient temperature, the noise figure of this part is equal to its loss. The loss of the isolator and band-pass filter are $0.4dB$ and $0.24dB$, respectively. The noise figure of the LNAs are equal to $2dB$. The gain of both the semi-rigid cable and isolator are equal to the inverse of their loss. The gain of the LNA is $35dB$.

The actual implementation of the loop structure to measure the noise figure is shown in Fig. 5.2. In this setup, the loop formed by the hybrid coupler is attached to an antenna looking at sky and also a matched load. The output is fed to a spectrum analyzer. The detected power post processed by applying inverse Fourier transform to estimate the autocorrelation response. The detected power of the matched load and the calibration signal are shown in Fig. 5.4(a). The autocorrelation response is illustrated in Fig. 5.4(b). The ripples in the power spectral domain are due to the rotation of the generated noise by the matched load inside the loop structure. In each rotation, part of the signal is amplified and detected by spectrum analyzer. Therefore, the detected signal is highly correlated in time domain. The calibration signal is detected when the left side of the loop is disconnected and terminated by the matched loads. In the calibration procedure, only the direct path of the signal is detected and the output power is uncorrelated in the time domain. The gain of the DUT can be extracted using the calibration procedure. The width of the peaks in the autocorrelation response in the time domain is inversely proportional to the bandwidth of the radiometer. Hence, wideband radiometers generates narrow peaks and vice versa. The estimated noise figure of the radiometer is shown in Fig. 5.5.

The estimation for the noise figure of the radiometer is $2.24dB$ using this technique, which is within $0.3dB$ of the calculated noise figure (NF) using Frii's formula. The sensitivity of this method to the sky temperature is also negligible. The changes in the noise figure of the radiometer for different sky temperatures of $3 - 10[K]$ is within $0.1dB$.

5.5 Conclusion

In this paper, a novel technique to estimate the noise figure (NF) of the wideband systems, such as amplifiers, receivers, and radiometers is presented. This technique relies on the calculation of the autocorrelation response of a loop setup. This setup is inspired by the multiple reflection back and forth inside a layered media. Based on Wiener-Khinchin theorem, the autocorrelation response can be extracted by calculating the inverse Fourier transform of the power spectral density. Analyzing the autocorrelation response of the received brightness temperature provides adequate information to estimate the noise figure of the wideband system of interest. The error in estimating the NF is less than $0.3dB$. The sensitivity of this method to the sky temperature is also negligible. This technique is capable of detecting the noise figure within the system wide bandwidth with only one measurement.

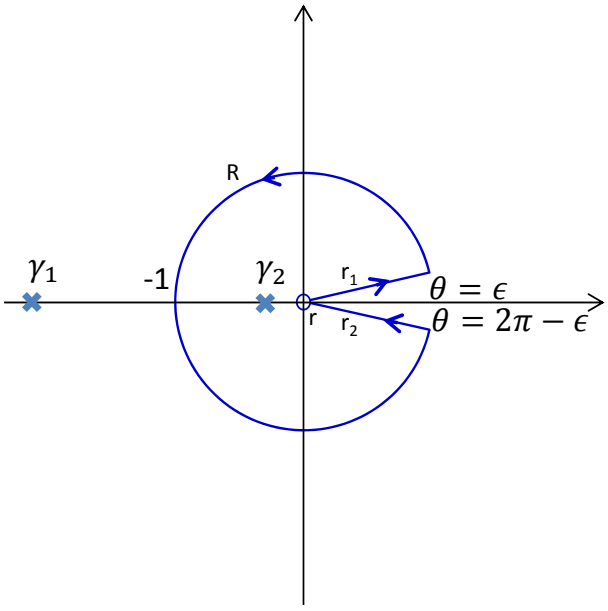

Figure 5.3: The contour that is used for the integration at $t = \tau$

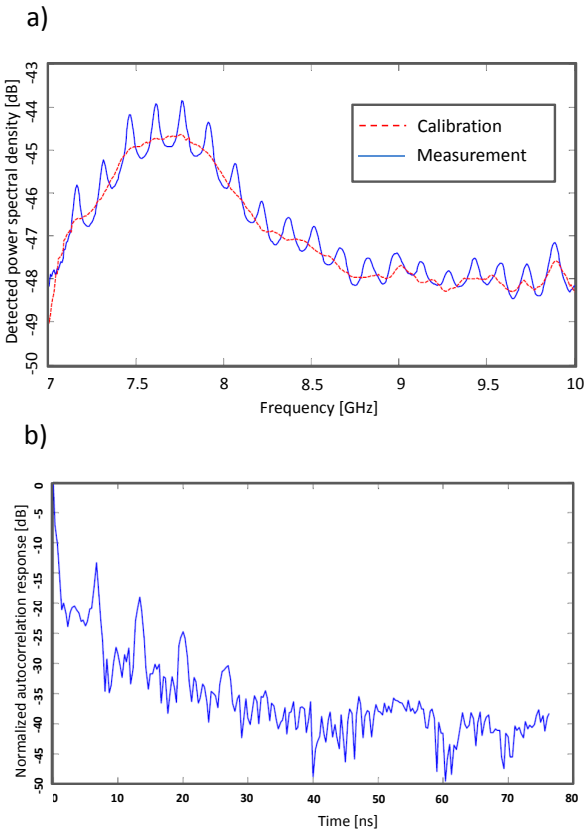

Figure 5.4: (a) The power spectral response of the loop structure to a WiBAR. The calibration signal (red dashed line) and the WiBAR response (solid blue line) are shown. The ripples are due to the signal circulating in the loop. (b) The autocorrelation response of the calibrated signal. The peaks are due to the signal delay inside the loop.

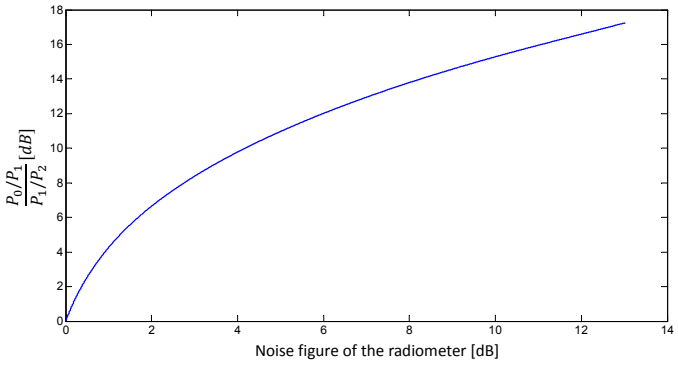

Figure 5.5: The difference between the zero lag peak and the first peak compared to the first peak to the second peak as a function of the noise figure of the wideband system.

CHAPTER VI

Conclusions and Future Work

6.1 A brief overview

In this thesis, the remote sensing estimation of low-loss dielectric layer thickness over a semi-infinite lossy medium is considered. Our technique is capable of estimating the thickness of snowpacks or fresh water ice layer over ground or lake. This problem is thoroughly modeled, simulated, verified using the measured results obtained from a novel wideband auto-correlation radiometer (WiBAR). By transforming the power spectral data to the time domain, the thickness of the ice/snow layer is estimated. The optimal design for the radiometer is presented. The radiometer has been tested for several controlled experiments as well as natural scenarios including snow and ice layers where the accuracy is found to be within $1.5cm$ for horizontally polarized far-field measurements compared to in-situ measurements. Three generations of the radiometer have been designed, developed, and implemented for optimal operations in detecting lake ice, snow, and autonomous lake ice measurements. Several post processing techniques have been developed to accurately estimate the thickness of the ice/snow layer. A novel technique based on compressive sensing has been developed to decrease the detection time.

A novel technique to estimate the noise figure (NF) of the wideband systems, such as amplifiers, receivers, and radiometers is also presented in this thesis. This

technique relies on the calculation of the autocorrelation response of a loop setup. This setup is inspired by the multiple reflection back and forth inside a layered media. Based on Wiener-Khinchin theorem, the autocorrelation response can be extracted by calculating the inverse Fourier transform of the power spectral density. Analyzing the autocorrelation response of the received brightness temperature provides adequate information to estimate the noise figure of the wideband system of interest. The error in estimating the NF is less than $0.3dB$. The sensitivity of this method to the sky temperature is also negligible.

6.2 Contribution

Our contributions in this thesis are listed below:

- We demonstrate that the power spectral measurement is necessary and sufficient for autocorrelation calculation using Wiener-Khinchin theorem.

- We model and design three generations of wideband radiometers using hand-held spectrum analyzers for maximum performance efficiency. The microwave circuit models for signal path are also developed using commercial off-the-shelf components (COTS). The first generation operates at $7 - 10GHz$ and is designed for lake ice thickness detection. The second generation works at lower frequency range of $1 - 3GHz$ and is designed for snow thickness detection. The third generation is an autonomous radiometer that can operate on harsh remote environment for lake ice detection.

- We analyze the sensitivity of WiBAR using the actual microwave circuit components and spectrum analyzer characteristics.

- We perform on-site measurements of air gap, ice, and snow layer thicknesses and verify our results against *in-situ* measurements.

- We thoroughly modeled and analyzed the physics of operation theoretically and statistically.
- The impact of radio frequency interference (RFI) on the autocorrelation response of the WiBAR has been explored. The effect of surface roughness on the emissivity and delay peak has bee investigated. A post processing technique to detect weak signals has been presented.
- A noise figure measurement system has been presented that can accurately estimate the noise figure of wideband radiometers and receivers.
- A compressive sensing based implementation of the WiBAR is introduced.
- An entropy based RFI detection technique is used to find RFIs.

6.2.1 Future work

We have designed and investigated the WiBAR in this work. There are several directions in this work that can be continued as the continuation of this work as listed below.

6.2.1.1 Optimum system design

The WiBAR can be designed without the utilization of the spectrum analyzer. The main use of the spectrum analyzer in our system is to monitor the power spectrum in the frequency band of interest. One of the fault point of our autonomous system design and the most expensive part of our system is the spectrum analyzer. By down converting the frequency using mixer and designing a super-heterodyne receiver with tunable bandwidth filter swept through the bandwidth, we can replace the spectrum analyzer. This microwave circuit can be designed for optimum operation and higher resolution than a COTS spectrum analyzer and is capable of operating efficiently at lower ambient temperatures compared to the COTS spectrum analyzer.

6.2.1.2 Real-time WiBAR design

For airborne and spaceborne applications, a fast real-time implementation of the system is of interest. One possible candidate for the high speed WiBAR is by implementing it in the time-domain using a fast sampling system.

6.2.1.3 Compressive sensing implementation in the time domain

Compressive sensing is a recent development in mathematics and signal processing with a possible solution to the ADC/DSP speed and accuracy bottlenecks for a broad class of applications. The Shannon/Nyquist sampling represents a worst-case scenario since it applies to arbitrary band-limited signals. In many applications signals have a sparse representation in some canonical system (Fourier, wavelets, etc.). For instance, the FM and MSK/OOK modulation schemes make high power cordless telephone (HPCT) signals sparse in the local-Fourier domain. Hence, sub-Nyquist sampling is possible using a random sampling scheme. The second key observation is that, to distill the small amount of information contained in a sparse signal, it is not necessary to perform expensive, adaptive post-processing on nonsparse data such as discrete-time samples or Fourier or wavelet coefficients. Rather, the information can be extracted directly from the analog RF signal if we alter our notion of sampling to replace time samples by more general random linear functionals. CS algorithms seek the sparsest signal that explains the measured information. These results have created a new paradigm, analog-to-information conversion (AIC or A2I), as a replacement for conventional ADC in certain applications. We can use the concept of compressive sensing, which can be applied to sparse signals to extract the information of the signal. Most of digital devices such as digital cameras or digital transceivers save/send a highly redundant data in digital domain; however the same signal has very small information content. Therefore, by converting the analog input signal to its information content, we are able to reduce the system complexity tremendously.

These design techniques can be used instead of ADCs or as demodulators to extract the information content of the received wireless signal.

The theory of random sampling suggests that we can build a random sampling based analog to information converter (RS-AIC) that recovers significant information about the input wideband signals from just a few measurements (samples) and with low computational complexity. Recovering signals with few samples achieves sub-Nyquist average sampling frequency, however, the minimum time separation between successive samples still governed by Nyquist-rate. Therefore, redistributing the samples in time enables us sub-Nyquist sampling clocks and to relax the design constraints of the low-rate ADC in the AIC design. The input analog signal is fed to the input multiplexer that selects the signal values with non-uniform timing and pushes them forward onto the analog queue, which stores the values via sample and hold (S/H). Finally, these values are read with uniform timing from the selection DEMUX and sampled with a sub-Nyquist rate ADC.

Another way to implement a fast, real time system for remote airborne and spaceborne WiBAR is to use very little samples far lower than the Nyquist rate (about tenth of Nyquist rate) in the time domain. Compressive sensing implementation using random sampling technique is a great candidate for this purpose. This idea can be implemented by wisely reconstructing an autocorrelation matrix consist of zeros and ones multiplied by pair combination of sample points called A_C. By multiplying a random matrix to the inverse of A_C we can reconstruct the sparse autocorrelation matrix.

6.2.1.4 Analysing lossy layer emission

In the case of lossy layer, which occurs if we are analyzing wet snow, ice layer with air bubbles, or the sea ice. In this case one possible approach is to use radiative transfer method. The analysis will be similar to analysis of atmosphere, in which several

horizontal layers with different refractive index and loss in each layer. This technique can be used to include the interlayer emission in the autocorrelation response of the system.

6.2.1.5 Vertical polarized implementation

Utilizing the vertical polarization together with high sensitivity ultrawide band WiBAR enables us to detect the relatively wider delay peak. Using this system, the Brewster angle can be detected, which can be used to find the refractive index at the top and bottom of the slab. The refractive index of the bottom of the snowpack is highly of interest to study the avalanches. The depth hoar is the snow located at the bottom of the snowpack formed due to large thermal gradients. Depth hoar is highly unstable mechanically and is a reason for avalanches.

BIBLIOGRAPHY

BIBLIOGRAPHY

[1] (1991), *Opportunities in the hydrologic sciences*, Comm. Opportunities Hydrol. Sci., Nat. Res. Council, Nat. Acad. Press, Washington, D.C.

[2] (1992), Report of Chapman conference on hydrological aspects of global climate change, *J. Geophys. Res.*, *97*, 2675–2833.

[3] (1998), *Global Energy and Water Cycle Experiment (GEWEX) Continental-Scale International Project (GCIP): A review of progress and opportunities*, Nat. Res. Council, Nat. Acad. Press, Washington, D.C.

[4] Andrei V. Shchegrov, R. C., Karl Joulain, and J.-J. Greffet (2000), Near-field spectral effects due to electromagnetic surface excitations, *Phys. Rev. Lett.*, *85*, 1548.

[5] Ashton, G. D. (1986), *River and lake ice engineering*, Water resources publications.

[6] Beirami, A., and H. Nejati (2012), Chaotic-map truly random number generators: evaluation of bit-generation and post-processing, *submitted to IEEE Trans. Circuits Syst. II.*

[7] Beirami, A., and H. Nejati (2013), A framework for investigating the performance of chaotic-map truly random number generators, *Circuits and Systems II: Express Briefs, IEEE Transactions on*, *60*(7), 446–450.

[8] Beirami, A., H. Nejati, and W. Ali (2012), Zigzag map: a variability-aware discrete-time chaotic-map truly random number generator, *Electronics Letters*, *48*(24), 1537–1538.

[9] Beirami, A., H. Nejati, and Y. Massoud (2012), A performance metric for discrete-time chaos-based truly random number generators, *arXiv preprint arXiv:1201.2201.*

[10] Bertocco, M., and A. Sona (2006), On the measurement of power via a superheterodyne spectrum analyzer, *IEEE Transactions on Iinstrumentation and Measurement*, *55*(5), 1494–1501.

[11] Bosma, H. (1967), *On the theory of linear noisy systems*, Technische Hogeschool.

[12] Brogioni, M., G. Macelloni, E. Palchetti, S. Paloscia, P. Pampaloni, S. Pettinato, E. Santi, A. Cagnati, and A. Crepaz (2009), Monitoring snow characteristics with ground-based multifrequency microwave radiometry, *IEEE Trans. Geosci. Remote Sens.*, *47*(11), 3643–3655.

[13] Bryant, G. H. (1988), *Principles of Microwave Measurements*, (IEE Electrical Measurement), London: The Institution of Engineering and Technology, pp. 107-110.

[14] Chang, A. T. C., J. L. Foster, D. K. Hall, A. Rango, and B. K. Hartline (1982), Snow water equivalent estimation by microwave radiometry, *Cold Regions Sci. Technol.*, *5*(3), 259–267.

[15] Chang, A. T. C., J. L. Foster, D. K. Hall, D. A. Robinson, L. Peiji, and C. Meisheng (1992), The use of microwave radiometer data for characterizing snow storage in western China, *Ann. Glaciol.*, *16*, 26–30.

[16] Derksen, C., B. Goddison, E. Ledrew, and A.Walker (2003), Combining SMMR and SSM/I data for time series analysis of central North American snow water equivalent, *J. Hydromet.*, *4*(2), 304–316.

[17] DeRoo, R. D., S. Misra, and C. S. Ruf (2007), Sensitivity of the kurtosis statistic as a detector of pulsed sinusoidal RFI, *IEEE Transactions on Geoscience and Remote Sensing*, *45*(7), 1938–1946.

[18] Durand, M., E. J. Kim, and S. A. Margulis (2008), Quantifying uncertainty in modeling snow microwave radiance for a mountain snowpack at the pointscale, including stratigraphic effects, *IEEE Trans. Geosci. Remote Sens.*, *46*(6), 1753–1767.

[19] Dyball, H. (2012), The next generation, *Electronics letters*, *48*(24), 1515–1515.

[20] England, A. W. (1974), Thermal microwave emission from a halfspace containing scatterers, *Radio Sci.*, *9*(4), 447–454.

[21] England, A. W. (1975), Thermal microwave emission from a scattering layer, *J. Geophys. Res.*, *80*(32), 4484–4496.

[22] England, A. W. (2013), Wideband autocorrelation radiometric sensing of microwave travel time in snowpacks and planetary ice layers, *IEEE Trans. Geosci. Remote Sens.*, *51*(4), 2316–2326, part 2.

[23] England, A. W., H. Nejati, and A. Mims (2011), Snowpack and freshwater ice sensing using autocorrelation radiometry, in *IEEE IGARSS*, pp. 3764–3767, Vancouver, BC, Canada.

[24] Friis, H. (1944), Noise figures of radio receivers, *Proceedings of the IRE*, *32*(7), 419–422.

[25] Galantowicz, J. F., and A. W. England (1997), Seasonal snowpack radiobrightness interpretation using a SVAT-linked emission model, *J. Geophys. Res.*, *102*(D18), 21,933–21,946.

[26] Goodison, B., E. Barry, and A. E.Walker (1993), Use of snow cover derived from satellite passive microwave data as an indicator of climate change, *Ann. Glaciol.*, *17*, 137–142.

[27] Guo, J.-J., L. Tsang, E. G. Josberger, A. W. Wood, J.-N. Hwang, and D. P. Lettenmaier (2003), Mapping the spatial distribution and time evolution of snow water equivalent with passive microwave measurements, *IEEE Trans. Geosci. Remote Sens.*, *41*(3), 612–621.

[28] Haitz, R., and F. Voltmer (1968), Noise in self-sustaining avalanche discharge in silicon: Studies at microwave frequencies, *J. Appl. Phys.*, *39*, 3379–3384.

[29] Hallikainen, M. T. (1992), Comparison of algorithms for retrieval of snow water equivalent from Nimbus-7 SMMR data in Finland, *IEEE Trans. Geosci. Remote Sens.*, *30*(1), 124–131.

[30] Hallikainen, M. T., and P. A. Jolma (1986), Retrieval of the water equivalent of snow cover in Finland by satellite microwave radiometry, *IEEE Trans. Geosci. Remote Sens.*, *GE-24*(6), 855–862.

[31] Han, H., and H. Lee (2013), Radar backscattering of lake ice during freezing and thawing stages estimated by ground-based scatterometer experiment and inversion from genetic algorithm, *IEEE Transactions on Geoscience and Remote Sensing*, *51*(5), 3089–3096.

[32] Harries, J. E. (1996), The greenhouse earth: A view from space, *Quarterly journal of the Royal Meteorological Society*, *122*, 799–799.

[*https://science.nrao.edu/facilities/vla/observing/RFI*] https://science.nrao.edu/facilities/vla/observing/RFI ().

[33] Kelly, R. E., A. T. C. Chang, L. Tsang, and J. L. Foster (2003), A prototype AMSR-E global snow area and snow depth algorithm, *IEEE Trans. Geosci. Remote Sens.*, *41*(2), 230–242.

[34] Koike, T., and T. Suhama (1993), Passive-microwave remote sensing of snow, *Ann. Glaciol.*, *18*, 305–308.

[35] Kraus, J. D., M. E. Tiuri, and A. V. Raisanen (1986), *Radio Astronomy*, Powell, Ohio: Cygnus-Quasar Books.

[36] Lane, R. (1969), The determination of device noise parameters, *Proceedings of the IEEE*, *57*, 1461–1462.

[37] Laveghetta, T. (1981), *Handbook of microwave testing*, Artech House, pp. 142 and 148.

[38] Lazo, A., and P. Rathie (1978), On the entropy of continuous probability distributions (corresp.), *Information Theory, IEEE Transactions on*, *24*(1), 120–122, doi:10.1109/TIT.1978.1055832.

[39] Leconte, R., and P. D. Klassen (1991), Lake and river ice investigations in Northern Manitoba using airborne SAR imagery, *The Arctic Institute North America*, *44*(5), 153–163.

[40] Lee, A. C., and G. Dalman (1994), *Microwave Devices, Circuits and Their Interaction*, Wiley Series in Microwave and Optical Engineering, New York: Wiley and Sons, pp. 140-157.

[41] Lemmetyinen, J., et al. (2009), A comparison of airborne microwave brightness temperatures and snowpack properties across the boreal forests of Finland and Western Canada, *IEEE Trans. Geosci. Remote Sens.*, *47*(3), 965–978.

[42] Lemmetyinen, J., et al. (2009), A comparison of airborne microwave brightness temperatures and snowpack properties across the boreal forests of Finland and Western Canada, *Geoscience and Remote Sensing, IEEE Transactions on*, *47*(3), 965–978.

[43] Liou, K. N. (1980), *An Introduction to Atmospheric Radiation*, vol. 84, second ed., International Geophysics series.

[44] Liu, D., H. Ren, L. Song, and H. Li (2005), Weak signal detection based on chaotic oscillator, in *Industry Applications Conference, 2005. Fourtieth IAS Annual Meeting. Conference Record of the 2005*, vol. 3, pp. 2054–2058, IEEE.

[45] Lopez-Moreno, J., S. Goyette, and M. Beniston (2009), Impact of climate change on snowpack in the Pyrenees: Horizontal spatial variability and vertical gradients, *Journal of Hydrology*, *374*(3-4), 384396.

[46] Macelloni, G., S. Paloscia, P. Pampaloni, and M. Tedesco (2001), Microwave emission from dry snow: A comparison of experimental and model results, *IEEE Trans. Geosci. Remote Sens.*, *39*(12), 2649–2656.

[47] Manwell, J., C. Elkinton, A. Rogers, and J. McGowan (2007), Review of design conditions applicable to offshore wind energy systems in the United States, *Renewable and Sustainable Energy Reviews*, *11*(2), 210–234.

[48] Marshall, E., and T. Randhir (2008), Effect of climate change on watershed system: a regional analysis, *Climatic Change*, *89*, 263280.

[49] McFarland, M. J., G. D. Wilke, and P. H. Harder (1987), Nimbus 7 SMMR investigation of snowpack properties in the northern Great Plains for the winter of 1978-1979, *IEEE Trans. Geosci. Remote Sens.*, *GE-25*(1), 3–46.

[50] Milly, P. C. D., J. Beancourt, M. Falkenmark, R. M. Hirsch, Z. W. Kundzewicz, D. P. Lettenmaier, and R. J. Stouffer (2008), Stationarity is dead: Whither water management?, *Science*, *319*(5863), 573–574.

[51] Misra, S. (2011), Development of radio frequency interference detection algorithms for passive microwave remote sensing, Ph.D. thesis, University of Michigan.

[52] Nejati, H., T. Ragheb, A. Hosseini, and Y. Massoud (2007), A programmable input-pulse dependent chaotic oscillator, in *Circuits and Systems, 2007. MWSCAS 2007. 50th Midwest Symposium on*, pp. 173–176, IEEE.

[53] Nejati, H., A. Beirami, and Y. Massoud (2008), A realizable modified tent map for true random number generation, in *Circuits and Systems, 2008. MWSCAS 2008. 51st Midwest Symposium on*, pp. 621–624, IEEE.

[54] Nejati, H., T. Ragheb, and Y. Massoud (2008), On the feasibility of bandwidth tuning in cascaded non-autonomous chaotic oscillators, in *Circuits and Systems, 2008. MWSCAS 2008. 51st Midwest Symposium on*, pp. 902–905, IEEE.

[55] Nejati, H., A. Beirami, and W. H. Ali (2012), Discrete-time chaotic-map truly random number generators: design, implementation, and variability analysis of the zigzag map, *Analog Integrated Circuits and Signal Processing*, *73*(1), 363–374.

[56] Olmstead, S. M. (2013), Climate change adaptation and water resource management: A review of the literature, *Energy Economics*, pp. 1–10.

[57] Orfanidis, S. J. (2014), Electromagnetic waves and antennas, http://www.ece.rutgers.edu/ orfanidi/ewa/.

[58] Papoulis, A. (1965), *Probability, random variables, and stochastic processes*, Mcgraw hill book company.

[59] Pfetsch, S., T. Ragheb, J. Laska, H. Nejati, A. Gilbert, M. Strauss, R. Baraniuk, and Y. Massoud (2008), On the feasibility of hardware implementation of sub-nyquist random-sampling based analog-to-information conversion, in *Circuits and Systems, 2008. ISCAS 2008. IEEE International Symposium on*, pp. 1480–1483, IEEE.

[60] Planck, M., and M. Masius (1914), *The theory of heat radiation*, Philadelphia: P. Blakiston's Son and Co.

[61] Pulliainen, J. T., and M. T. Hallikainen (2001), Retrieval of regional snow water equivalent from space-borne passive microwave observations, *Remote Sens. Environ*, *75*(1), 76–85.

[62] Pulliainen, J. T., J. Grandell, and M. T. Hallikainen (1999), Hut snow emission model and its applicability to snow water equivalent retrieval, *IEEE Trans. Geosci. Remote Sens.*, *37*(3), 1378–1390.

[63] Ragheb, T., J. N. Laska, H. Nejati, S. Kirolos, R. G. Baraniuk, and Y. Massoud (2008), A prototype hardware for random demodulation based compressive analog-to-digital conversion, in *Circuits and Systems, 2008. MWSCAS 2008. 51st Midwest Symposium on*, pp. 37–40, IEEE.

[64] Rice, J. (1995), *Mathematical Statistics and Data Analysis*, second ed., Duxbury Press.

[65] Rytov, S. M., Y. A. Kravtsov, V. I. Tatarskii, and A. P. Repyev (1988), *Principles of Statistical Radiophysics 2: Correlation Theory of Random Processes*, springer-verlag.

[66] Rytov, S. M., Y. A. Kravtsov, V. I. Tatarskii, and A. P. Repyev (1988), *Principles of Statistical Radiophysics 3: Elements of Random Fields*, springer-verlag.

[67] Schweizer, J., K. Kronholm, J. B. Jamieson, and K. W. Birkeland (2008), Review of spatial variability of snowpack properties and its importance for avalanche formation, *Cold Regions Science and Technology*, *51*, 253272.

[68] Serreze, M. C., et al. (2000), Observational evidence of recent change in the northern high-latitude environment, *Clim. Chang.*, *46*(1/2), 159–207.

[69] Skou, N., and D. M. L. Vine (2006), *Microwave Radiometer Systems: Design and Analysis*, Artech House, Incorporated.

[70] Smith, J. O. (2007), *Mathematics of the Discrete Fourier Transform (DFT), with Audio Applications*, W3K Publishing.

[71] Stankov, B. B., D. Cline, B. L.Weber, A. J. Gasiewski, and G. A.Wick (2008), High-resolution airborne polarimetric microwave imaging of snow cover during the NASA cold land processes experiment, *IEEE Trans. Geosci. Remote Sens.*, *46*(11), 3672–3693.

[72] Stoica, P., and R. L. Moses (1997), *Introduction to spectral analysis*, vol. 1, Prentice hall Upper Saddle River, NJ.

[73] Stoica, P., and T. Soderstrom (1990), High-order Yule-Walker equations for estimating sinusoidal frequencies: The complete set of solutions, *Signal processing*, *20*(3), 257–263.

[74] Sutton, R. T., B. Dong, and J. M. Gregory (2007), Land/sea warming ratio in response to climate change: IPCC AR4 model results and comparison with observations, *Geophys. Res. Lett.*, *34*, L02,701.

[75] Tsang, L., J. A. Kong, K.-H. Ding, and C. O. Ao (2004), *Scattering of Electromagnetic Waves, Theories and Applications*, Wiley.

[76] Tsang, L., J. A. Kong, K.-H. Ding, and C. O. Ao (2004), *Scattering of Electromagnetic Waves, Numerical Simulations*, Wiley.

[77] Tsang, L., J. A. Kong, K.-H. Ding, and C. O. Ao (2004), *Scattering of Electromagnetic Waves, Advanced Topics*, Wiley.

[78] Ulaby, F. T., R. K. Moore, and A. K. Fung (1981), *Microwave Remote Sensing: Active and Passive*, vol. I, Artech House.

[79] Ulaby, F. T., R. K. Moore, and A. K. Fung (1981), *Microwave Remote Sensing: Active and Passive*, vol. II, Artech House.

[80] Ulaby, F. T., R. K. Moore, and A. K. Fung (1981), *Microwave Remote Sensing: Active and Passive*, vol. III, Artech House, pp. 1065-2162.

[*Vickers*] Vickers, R. S. (), *Tech. rep.*

[81] Vrsmarty, C. J., L. D. Hinzman, B. J. Peterson, D. H. Bromwich, L. C. Hamilton, J. Morison, V. E. Romanovsky, M. Sturm, and R. S.Webb (2000), The hydrologic cycle and its role in arctic and global environmental change: A rationale and strategy for synthesis study, *Tech. rep.*, Arctic Res. Consort. U.S., Fairbanks, AK.

[82] Waitt, J. R. B., T. C. Pierson, N. S. Macleod, R. J. Janda, B. Voight, and R. T. Holcomb (1983), Eruption-triggered avalanche, flood, and lahar at Mount St. Helens effects of winter snowpack, *Science*, *221*(4618), 1394–1397.

[83] Wang, G., and S. He (2003), A quantitative study on detection and estimation of weak signals by using chaotic duffing oscillators, *Circuits and Systems I: Fundamental Theory and Applications, IEEE Transactions on*, *50*(7), 945–953.

[84] Wang, G., D. Chen, J. Lin, and X. Chen (1999), The application of chaotic oscillators to weak signal detection, *Industrial Electronics, IEEE Transactions on*, *46*(2), 440–444.

[85] Wang, G., W. Zheng, and S. He (2002), Estimation of amplitude and phase of a weak signal by using the property of sensitive dependence on initial conditions of a nonlinear oscillator, *Signal processing*, *82*(1), 103–115.

[86] Wilson, L. L., L. Tsang, J. N. Hwang, and C. T. Chen (1999), Mapping snow water equivalent by combining a spatially distributed snow hydrology model with passive microwave remote-sensing data, *IEEE Trans. Geosci. Remote Sens.*, *37*(2), 690–704.